Monte Carlo Simulation of the DUNE Stopped Muon Monitor Prototype Exposed to Cosmic Ray Muons

by

Sergey Gitalov

Undergraduate Honors Thesis

University of Colorado Boulder

College of Arts and Sciences

2020

This thesis entitled:
Monte Carlo Simulation of the DUNE Stopped Muon Monitor Prototype Exposed to Cosmic Ray Muons
written by Sergey Gitalov
has been approved for the Department of Physics

Prof. Eric D. Zimmerman
Department of Physics

Prof. John P. Cumalat
Department of Physics

Dr. Joseph Timmer
Department of Mathematics

Date : April 3, 2020

The final copy of this thesis has been examined by the signatories, and we find that both the content and the form meet acceptable presentation standards of scholarly work in the above mentioned discipline.

Sergey Gitalov, (B.A., Physics)

Monte Carlo Simulation of the DUNE Stopped Muon Monitor Prototype Exposed to Cosmic Ray Muons

Thesis directed by Prof. Eric D. Zimmerman

Department of Physics

The Stopped Muon Monitor (SMM) is a muon monitor planned to be deployed at the DUNE experiment. A prototype of the SMM is being tested at the University of Colorado in Boulder using cosmic ray muons. In this thesis, I discuss the Geant4 Monte Carlo simulation of the SMM prototype exposed to cosmic ray muons. I create a model of cosmic ray muons that is used to simulate $5 \cdot 10^7$ muons generated above the SMM. I categorize data into geometry-based selection cuts that are based on muon and Michel electron trajectory through the detector. I find that scintillation and Cherenkov light detected by the SMM from incoming muons and their daughter electrons can be used to evalue the Monte Carlo SMM geometry for future corrections.

Contents

Chapter

1 Introduction **1**

1.1 Neutrino Oscillations . . . 1

1.2 Deep Underground Neutrino Experiment (DUNE) . . . 2

1.3 Stopped Muon Monitor . . . 3

1.4 Thesis Overview . . . 3

2 Neutrino Oscillations **5**

2.1 Oscillation Mechanism . . . 5

2.1.1 Neutrinos in Vacuum . . . 5

2.1.2 Neutrinos in Matter . . . 8

2.2 Open Questions . . . 12

2.2.1 Value of δ_{CP} . . . 12

2.2.2 Neutrino Mass Hierarchy . . . 12

2.2.3 Sterile Neutrinos and Dark Matter Candidates . . . 12

3 Deep Underground Neutrino Experiment (DUNE) **14**

3.1 Outline and Goals of DUNE . . . 14

3.2 Neutrino Beam Generation . . . 15

3.3 DUNE Detectors . . . 18

3.3.1 Muon Alcove . . . 18

3.3.2 Near Detector 18

3.3.3 Far Detector 20

4 Stopped Muon Monitor Description and Physics Background **23**

4.1 Monitor Description 23

4.2 Physics Background 25

4.2.1 Photomultiplier Tubes 25

4.2.2 Cosmic Ray Muons 26

4.2.3 Passage of Muons Through Material 26

4.2.4 Scintillation 29

4.2.5 Muon Decays 31

4.2.6 Cherenkov Radiation 31

4.2.7 Muon Capture 32

5 Monte Carlo Setup and Results **34**

5.1 Monte Carlo Setup 34

5.2 Preliminary Tests 36

5.2.1 Zenith Angle Dependence Test 36

5.2.2 Initial Muon Distribution Radius Test 37

5.3 Main Test 41

5.3.1 Dataset Partitions 41

5.3.2 Muon Signal 43

5.3.3 Electron Signal 47

5.3.4 Quantum Efficiency Weights 52

6 Conclusion and Future Work **55**

Bibliography **57**

Appendix

A **59**

Tables

Table

2.1 T2K estimates of $\sin^2\theta_{23}, |\Delta m^2_{23}|, \sin^2\theta_{13}$, and δ_{CP} as of 2020 according to Scott [5]. 7

2.2 Values of mixing angles, δ_{CP}, and mass squared differences as of fall 2018 according to Esteban et al [10]. Note that $\Delta m^2_{l3} = \Delta m^2_{13}$ for normal hierarchy and $\Delta m^2_{l3} = \Delta m^2_{23}$. 7

2.3 Possible neutrino interactions and estimated interaction rates in the Near Detector on argon (carbon) at the DUNE experiment assuming 120 GeV proton beam energy and $1 \cdot 10^{20}$ protons on target 574 m away using cross-section predictions from GENIE software.[6, 11] 10

3.1 Main K^+ decay modes [3]. Decay modes with $< 1\%$ occurrence are omitted. 17

5.1 Geometry-based cuts, ratio of number of events in the cut to number of events, where a muon entered SMM (overall ratio); and ratio of number of events in the cut to number of events for cuts with the same Greek letter (relative ratio). 44

A.1 Figure 4.2 fit parameters 59

Figures

Figure

2.1 Fundamental particles of the Standard Model. 6

2.2 Oscillation probabilities at a baseline of 1300 km as a function of neutrino energy for neutrinos (left) and antineutrinos (right) for $\delta_{CP} = -\pi/2$ (blue), 0 (red), and $\pi/2$ (green) and normal mass hierarchy [6]. Matter effects are accounted for, which results in an additional asymmetry even at $\delta_{CP} = 0$. 11

2.3 Value of $\mathcal{A}_{CP}^{\mu\rightarrow e}$ at the first and second oscillation maxima for $\delta_{CP} = 0$ with matter effects (solid line) and $\delta_{CP} = \pm\pi/2$ without matter effects (dashed line) for normal (left) and inverted (right) hierarchies as functions of baseline length [9]. 11

3.1 A simplified schematic of the DUNE experiment [7]. 14

3.2 DUNE Near Site schematic [16]. 15

3.3 Cross-section of the magnetic horns used in the NuMI experiment [17]. DUNE will use horn design based on the NuMI designs[7]. 16

3.4 Proposed Hadron Absorber at DUNE [16]. 18

3.5 Proposed Hadron Absorber (left) and Muon Alcove (right) at DUNE with the beam profile (blue line) [8]. The Stopped Muon Monitors will be installed between blocks of steel (grey). 19

3.6 DUNE Near Detector reference design [18]. The neutrino beam is indicated by the dashed blue line. 21

3.7 Cross section of the DUNE Far Detector 10 kt LArTPC [19]. APA stands for Anode Plane Assembly, CPA stands for Cathode Plane Assembly. 22

4.1 Stopped Muon Monitor. View from the side (a) and from the top (b). Both the Inner and Outer Detectors are encased in metal shells (blue), and have 4 PMTs (yellow) each at the top. 24

4.2 PMT quantum efficiency (dashed line) versus photon wavelength for a bialkali photocathode [20] used in the SMM PMT. At wavelengths less than 300 nm, glass on the photocathode becomes opaque. 27

4.3 Cosmic ray muon flux distribution versus muon zenith angle [21]. Solid lines represent data at various muon momenta. Dashed lines are reference distributions for differential flux being proportional to $\cos^2\theta$ (orange) and $\cos^{-1}\theta$ (blue) respectively. 28

4.4 Muon stopping power when passing through copper [3]. 30

4.5 Energy spectrum of Michel electrons. Data obtained from Geant4 simulation. 30

4.6 Wavelength spectrum of Cherenkov light emitted by a Michel electron in mineral oil. Data obtained from Geant4 simulation. 33

5.1 Cosine of zenith angle distribution for muons that hit the SMM for the polynomial (c) and $\cos^2\theta$ (d) fits. 38

5.2 Projections of muon momentum on entry to the SMM in the xy (a,b), xz (c,d), and yz (e,f) planes for the polynomial (a,c,e) and $\cos^2\theta$ (b,d,f) models. Enlarged plots in Appendix. 39

5.3 Signal vesus particle total energy of muons in OD (a,b), muons in ID (c,d), and electrons in ID (e,f) for the polynomial (a,c,e) and $\cos^2\theta$ (b,d,f) models. Enlarged plots in Appendix. 40

5.4 Initial xy-position of muons that hit the SMM in the Monte Carlo with $\cos^2\theta$ zenith angle distribution 42

5.5 Pie charts of ratios in Table 5.1 for muon fate (a), and relative ratios: muon escape (b), muon capture (c), muon decay (d). The relative ratio of $OIO\delta OIO$ (pink) in (d) is too small to label. 45

5.6 Muon signal in the OD versus total energy on entry for all muons that entered the SMM (a), $OI\delta$ cut (b), $O\delta$ cut (c), $OIO\delta$ cut (d), $O\epsilon$ cut (e), and $OIO\epsilon$ cut (f). Enlarged plots in Appendix. 48

5.7 Muon signal in the ID versus total energy for muons entering OD (a) and only contained events (b). 49

5.8 Electron signal in the ID versus electron total energy for any electron in ID (a) and only contained events (b). 50

5.9 Signal in the ID versus distance traveled in the ID by electrons for contained (a) and uncontained (b) events. 51

5.10 Projections of initial Michel electron position in the ID in the xy (a,b), xz (c,d), yz (e,f) planes for contained (a,c,e) and uncontained (b,d,f) electrons. Enlarged plots in Appendix. 53

5.11 Signal distribution for muons in OD (a,b) and electrons in ID (c,d) without quantum efficiency weights (a,c) and with weights (b,d). Enlarged plots in Appendix. 54

Chapter 1

Introduction

1.1 Neutrino Oscillations

The Standard Model is a well-established modern particle physics theory that succeeded in explaining the three fundamental forces of nature that are at heart of particle interactions [1]. Despite the Standard Model's tremendous success, physicists are actively searching for any extensions that could open opportunities for "new physics". One of these phenomena that was not explained by the Standard Model is known as neutrino oscillations.

The Standard Model assumes that the fundamental particles called neutrinos have zero mass, and for a long time this was thought to be the case. However, during experiments attempting to measure the neutrino flux from the Sun, an astonishing discrepancy was found. The Sun fuses hydrogen in a reaction known as a proton-proton chain reaction, where electron neutrinos are the only neutrino flavor produced. However, experiments measuring solar neutrino flux found considerably fewer electron neutrinos than predicted [2]. A theoretical solution to this problem was found in the theory of neutrino oscillations. It was proposed that neutrinos can oscillate: change flavors as they propagate. The theory requires neutrinos to have mass, which is not predicted by the Standard Model [3]. Hence, neutrino oscillations are an exciting avenue for "new physics" beyond the Standard Model that can enhance our understanding about fundamental particles in nature.

Today, neutrino oscillations are an accepted scientific model that successfully resolved the solar neutrino problem [2]. Nevertheless, many parameters of the model remain either measured with insufficient precision or remain undetermined. For instance, the mass squared difference between two neutrino eigenstates is known, but the relative mass of the third neutrino eigenstate is not. This is known as neutrino mass hierarchy problem [4]. Not only mass hierarchy affects oscillation rates, it also presents opportunities for new theoretical research, as an inverted mass hierarchy would be very unusual and different from mass hierarchies in the Standard Model.

But perhaps the most intriguing open question is whether or not neutrinos violate charge-parity (CP) symmetry, that is whether there is a difference between matter and antimatter in oscillations. If present, neutrino charge-parity violation would be one of the few known examples of CP-violation, and the first such example unrelated to quark flavor. Currently it is not precisely known if neutrino oscillations violate CP [5].

1.2 Deep Underground Neutrino Experiment (DUNE)

In order to solve these problems, a number of neutrino experiments is either currently active or planned. Among the planned ones is the Deep Underground Neutrino Experiment (DUNE), which is planned to be completed by late 2020s. DUNE will be the most advanced neutrino beamline experiment upon completion. It will collect enough precise data to measure neutrino oscillation parameters and answer the mass hierarchy and CP-violation problems [6].

Neutrino oscillations at DUNE will be studied by producing a beam of neutrinos that is probed by two neutrino detectors: the Near and Far Detectors (ND and FD). First, the neutrino beam will be produced at the Long Baseline Neutrino Facility (LBNF) at Fermi National Accelerator Laboratory (FNAL or Fermilab), Illinois [7]. The Near Detector is to be installed at LBNF, close to where the beam is produced, in order to measure the initial neutrino flux. After passing the Near Detector, neutrinos will propagate 1300 km through earth and encounter the Far Detector at the Sanford Underground Research Facility (SURF) at Homestake Mine, South Dakota. As neutrinos continue to propagate, they have a chance to oscillate before they reach the Far Detector. They are then probed in the FD, and neutrino counts for each flavor are compared between the ND and the FD. Any differences in the number of observed neutrinos by flavor indicate that an oscillation took place during propagation [7]. Additionally, DUNE will produce beams of antineutrinos to look for signs of CP-violation [7]. These precise measurements of neutrino counts allows to infer the values of parameters that govern the neutrino oscillation mechanism.

1.3 Stopped Muon Monitor

In order to constrain the neutrino beam flux with required precision, DUNE will deploy particle detectors that monitor muons, which are the byproducts of the neutrino beam production [8]. This thesis focuses on one of the muon detectors planned to be installed at DUNE, the Stopped Muon Monitor (SMM). This particle detector is unusual in that it tracks muons that stopped inside the detector, rather than probe muons in flight. By installing steel shielding for muons to slow down, muons in a selected energy ranges can lose enough energy, stop in the SMM, and be detected, allowing to separately measure portions of the muon beam flux. This energy range selection is an advantage of the SMM that other muon monitors at DUNE do not have.

The SMM prototype is currently being tested at the University of Colorado in Boulder using comsic ray muons. Cosmic ray muons provide a natural source of muons for experiments, and Boulder is particularly good for such experiments due to increased muon flux at higher altitudes. In order to evaluate results from the prototype data, I created a Monte Carlo to simulate the SMM exposed to cosmic ray muons using Geant4 software. Future data from the prototype can be compared to the SMM test results and corrections can be applied. The corrected Monte Carlo can eventually be used to simulate the SMM in the DUNE beamline.

1.4 Thesis Overview

This thesis will provide a description of the DUNE experiment and specifically description and results of a Monte Carlo simulation of the Stopped Muon Monitor prototype. In Chapter 2, I will describe neutrinos in the Standard Model, explain the mechanism of neutrino oscillations, and state current unresolved problems in neutrino physics. In Chapter 3, I will give a description of the DUNE experiment goals and planned facilities. In Chapter 4, I will first give a description of the Stopped Muon Monitor and the principles behind its operation. I will then give a brief physics background to the processes that govern the SMM's operation. In Chapter 5, I will give the description of the Monte Carlo simulation, and then state and discuss the results of the Monte Carlo. In Chapter 6, I will provide a conclusion as well as state the future work on the Stopped Muon Monitor.

Chapter 2

Neutrino Oscillations

2.1 Oscillation Mechanism

2.1.1 Neutrinos in Vacuum

Neutrinos are fundamental particles of the Standard Model. These particles are chargeless and colorless, interacting only through the weak force. They come in three flavors ν_e, ν_μ, ν_τ, corresponding to the charged lepton flavors: electrons (e), muons (μ), and tau (τ) respectively [1]. Each lepton flavor in the Standard Model is given its own quantum number called "lepton flavor number". Since lepton flavor number is conserved in weak interactions, the Standard Model predicts that neutrinos never change flavor [1]. However, this was observed not to be the case [2]. To explain the oscillation process, the Pontecorvo-Maki-Nakagawa-Sakata (PMNS) matrix is used [4]. Interestingly, the PMNS matrix requires neutrinos to have mass, while the Standard Model assumes neutrinos are massless.

The three neutrino flavor states form the flavor basis $\{|\nu_e\rangle, |\nu_\mu\rangle, |\nu_\tau\rangle\}$, while the three neutrino mass states form the mass basis $\{|\nu_1\rangle, |\nu_2\rangle, |\nu_3\rangle\}$. Whereas there is a direct correspondence between these bases for charged leptons (i.e. each flavor has a unique corresponding mass), this is not the case for neutrinos. One transforms from the mass basis to the flavor basis via the PMNS

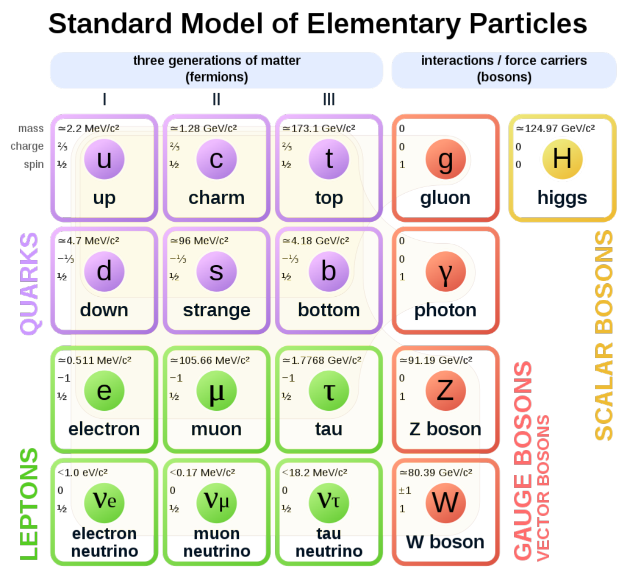

Figure 2.1: Fundamental particles of the Standard Model.

unitary matrix [4]:

$$\begin{pmatrix} |\nu_e\rangle \\ |\nu_\mu\rangle \\ |\nu_\tau\rangle \end{pmatrix} = U_{PMNS} \begin{pmatrix} |\nu_1\rangle \\ |\nu_2\rangle \\ |\nu_3\rangle \end{pmatrix} = \begin{pmatrix} U_{e1} & U_{e2} & U_{e3} \\ U_{\mu 1} & U_{\mu 2} & U_{\mu 3} \\ U_{\tau 1} & U_{\tau 2} & U_{\tau 3} \end{pmatrix} \begin{pmatrix} |\nu_1\rangle \\ |\nu_2\rangle \\ |\nu_3\rangle \end{pmatrix} \tag{2.1}$$

where

$$U_{PMNS} = \begin{pmatrix} 1 & 0 & 0 \\ 0 & c_{23} & s_{23} \\ 0 & -s_{23} & c_{23} \end{pmatrix} \begin{pmatrix} c_{13} & 0 & e^{-i\delta_{CP}} s_{13} \\ 0 & 1 & 0 \\ -e^{i\delta_{CP}} s_{13} & 0 & c_{13} \end{pmatrix} \begin{pmatrix} c_{12} & s_{12} & 0 \\ -s_{12} & c_{12} & 0 \\ 0 & 0 & 1 \end{pmatrix} \tag{2.2}$$

where $c_{jk} = \cos\theta_{jk}$ and $s_{jk} = \sin\theta_{jk}$. The mixing angles $\theta_{12}, \theta_{13}, \theta_{23}$ govern oscillation rates and are analogous to Euler angles for rotations in three dimensions [4]. The charge-parity phase δ_{CP} is a parameter that, when non-zero, causes neutrinos and antineutrinos to oscillate at different rates [4, 9]. Some of the estimates for the oscillation parameters above are presented in Tables 2.1 and 2.2.

Due to Einstein's energy-mass equivalence, the mass basis is an eigenbasis of the Hamiltonian. Since the flavor basis is distinct from the mass basis, it is not an eigenbasis of the Hamiltonian.

Parameter	Value (Normal Hierarchy)	Value (Inverted Hierarchy)
$\sin^2\theta_{23}$	$0.55^{+0.05}_{-0.09}$	$0.55^{+0.05}_{-0.08}$
$\lvert\Delta m^2_{23}\rvert$	$(2.54 \pm 0.08) \cdot 10^{-3}\ eV^2$	$(2.51 \pm 0.08) \cdot 10^{-3}\ eV^2$
$\sin^2\theta_{13}$	$0.027^{+0.007}_{-0.006}$	$0.030^{+0.008}_{-0.007}$
δ_{CP}	$-1.73^{+0.85}_{-0.81}$	$-1.45^{+0.67}_{-0.72}$

Table 2.1: T2K estimates of $\sin^2\theta_{23}, |\Delta m^2_{23}|, \sin^2\theta_{13}$, and δ_{CP} as of 2020 according to Scott [5].

Parameter	Value (Normal Hierarchy)	Value (Inverted Hierarchy)
$\sin^2\theta_{12}$	$0.310^{+0.013}_{-0.012}$	$0.310^{+0.013}_{-0.012}$
$\sin^2\theta_{23}$	$0.580^{+0.017}_{-0.021}$	$0.584^{+0.016}_{-0.020}$
$\sin^2\theta_{13}$	0.02241 ± 0.00065	0.02264 ± 0.00066
δ_{CP}	$-2.53^{+0.51}_{-0.70}$	$-1.33^{+0.51}_{-0.47}$
Δm^2_{12}	$(7.39^{+0.21}_{-0.20}) \cdot 10^{-5}\ eV^2$	$(7.39^{+0.21}_{-0.20}) \cdot 10^{-5}\ eV^2$
$\lvert\Delta m^2_{l3}\rvert$	$(2.525^{+0.033}_{-0.031}) \cdot 10^{-3}\ eV^2$	$(2.512^{+0.034}_{-0.031}) \cdot 10^{-3}\ eV^2$

Table 2.2: Values of mixing angles, δ_{CP}, and mass squared differences as of fall 2018 according to Esteban et al [10]. Note that $\Delta m^2_{l3} = \Delta m^2_{13}$ for normal hierarchy and $\Delta m^2_{l3} = \Delta m^2_{23}$.

This causes the components of the flavor basis to oscillate according to Schrödinger equation:

$$|\nu_\alpha(t)\rangle = \sum_{j=1}^{3} U_{\alpha j} \, |\nu_j\rangle \, e^{-iE_j t/\hbar} \tag{2.3}$$

where ν_α is some neutrino flavor, $E_j = \sqrt{m_j^2 c^4 + p^2 c^2}$ is relativistic total energy. Thus, we can calculate oscillation probability between two flavors ν_α and ν_β as follows:

$$\mathcal{P}_{\nu_\alpha \to \nu_\beta}(t) = |\,\langle \nu_\beta | \nu_\alpha(t) \rangle\,|^2 = \left| \sum_{j=1}^{3} U_{\beta j}^* U_{\alpha j} e^{-iE_j t/\hbar} \right|^2 \tag{2.4}$$

Since neutrinos are extremely light, they move at the speed close to the speed of light, so we let $t = L/c$, where L is travel length. Additionally, we can also assume that $pc >> mc^2$. With these assumptions, the oscillation probability becomes a function of the mixing angles θ_{ij}, the charge-parity phase δ_{CP}, difference in masses squared $\Delta m_{jk}^2 = m_j^2 - m_k^2$, travel length L, and neutrino energy E_ν:

$$\mathcal{P}_{\nu_\alpha \to \nu_\beta} = \mathcal{P}_{\nu_\alpha \to \nu_\beta}(\theta_{jk}, \delta_{CP}, \Delta m_{jk}^2, L, E_\nu) \tag{2.5}$$

The CP-asymmetry can be estimated through a parameter $\mathcal{A}_{CP}^{\alpha \to \beta}$ defined as:

$$\mathcal{A}_{CP}^{\alpha \to \beta} = \frac{\mathcal{P}_{\nu_\alpha \to \nu_\beta} - \mathcal{P}_{\overline{\nu}_\alpha \to \overline{\nu}_\beta}}{\mathcal{P}_{\nu_\alpha \to \nu_\beta} + \mathcal{P}_{\overline{\nu}_\alpha \to \overline{\nu}_\beta}} \tag{2.6}$$

For a muon neutrino oscillating into an electron neutrino we can approximate $\mathcal{A}_{CP}^{\mu \to e}$ as [9]:

$$\mathcal{A}_{CP}^{\mu \to e} \approx \sin \delta_{CP} \frac{\cos \theta_{23} \sin 2\theta_{12}}{\sin \theta_{23} \sin \theta_{13}} \Delta_{21} \tag{2.7}$$

where $\Delta_{21} = \Delta m_{21}^2 L/(4E_\nu)$. Therefore CP-violation is maximal if $\delta_{CP} = \pm\pi/2$, and is not present at all if $\delta_{CP} = 0$ or π.

2.1.2 Neutrinos in Matter

Neutrinos rarely interact with matter, making their detection a tough challenge [1]. Nevertheless, there are several processes possible between a neutrino and an atomic nucleus [6]. Neutrinos passing through matter may interact with the nuclei via either elastic or inelastic interactions. Elastic interactions result in a neutrino getting scattered, but otherwise unchanged. On the other hand, inelastic collisions result in production of new particles that can be detected in an experiment [6]. Another way to characterize neutrino interactions is as either charged (CC) or neutral (NC) current. CC interactions are mediated by charged bosons $W^{\pm}$, while neutral current interactions are mediated by the chargeless Z boson . These interactions as well as their expected rates in the DUNE experiment are listed in Table 2.3.

As neutrinos propagate in matter, various processes cause an additional matter-antimatter asymmetry that is different from CP-violation [4, 9]. Therefore matter effects can interfere with measurements of δ_{CP} in neutrino baseline experiments. With matter effects oscillation probability from muon neutrino to electron neutrino, which is the primary oscillation in the DUNE experiment, becomes [9]:

$$\mathcal{P}_{\nu_\mu \to \nu_e} \approx \sin^2\theta_{23}\sin^2 2\theta_{13}\frac{\sin^2(\Delta_{31}-aL)}{(\Delta_{31}-aL)^2}\Delta_{31}^2+$$

$$+\sin 2\theta_{23}\sin 2\theta_{13}\sin 2\theta_{12}\frac{\sin(\Delta_{31}-aL)}{\Delta_{31}-aL}\Delta_{31}\frac{\sin aL}{aL}\Delta_{21}\cos(\Delta_{31}+\delta_{CP})+$$

$$+\cos^2\theta_{23}\sin^2 2\theta_{12}\frac{\sin^2 aL}{(aL)^2}\Delta_{21}^2 \tag{2.8}$$

where $\Delta_{jk} = \Delta m^2_{jk}L/(4E_\nu)$, $a = G_F N_e/\sqrt{2}$, G_F is the Fermi constant, N_e is number of electrons in matter per unit volume, L is baseline length, E_ν is the neutrino energy. Plots of oscillation probabilities $\mathcal{P}_{\nu_\mu \to \nu_e}$ and $\mathcal{P}_{\overline{\nu}_\mu \to \overline{\nu}_e}$ with matter effects can be found in Figure 2.2.

With matter effects, the asymmetry parameter $\mathcal{A}^{\mu \to e}_{CP}$ depends on the baseline length [9]. Plots of $\mathcal{A}^{\mu \to e}_{CP}$ as function of baseline length at the first and second oscillation maxima are presented in Figure 2.3. At the second oscillation maximum the difference in $\mathcal{A}^{\mu \to e}_{CP}$ between $\delta_{CP} = 0$ and $\delta_{CP} = \pi/2$ becomes large enough to precisely measure the value of δ_{CP} [9]. However, short baseline experiments ($< 1000\ km$) are not capable of detecting the second $\nu_\mu \to \nu_e$ oscillation maximum, due to neutrino energy being too low for detectors. On the other hand, at long baseline experiments, the neutrino energy at the second oscillation maximum is large enough to detect [9].

Production mode	ν_μ Events on Ar (Carbon)	$\overline{\nu}_\mu$ Events on Ar (Carbon)
CC QE ($\nu_\mu n \to \mu^- p$)	30,000 (28,000)	13,000 (15,000)
NC elastic ($\nu_\mu N \to \nu_\mu N$)	11,000 (11,000)	6,700 (68,00)
CC resonant ($\nu_\mu p \to \mu^- p \pi^+$)	21,000 (24,000)	0 (0)
CC resonant ($\nu_\mu n \to \mu^- n \pi^+ \, (p\pi^0)$)	23,000 (21,000)	0 (0)
CC resonant ($\bar{\nu}_\mu p \to \mu^+ p \pi^- \, (n\pi^0)$)	0 (0)	83,00 (7,800)
CC resonant ($\bar{\nu}_\mu n \to \mu^+ n \pi^-$)	0 (0)	12,000 (8,100)
NC resonant ($\nu_\mu p \to \nu_\mu p \pi^0 \, (n\pi^+)$)	7,000 (9,200)	0 (0)
NC resonant ($\nu_\mu n \to \nu_\mu n \pi^+ \, (p\pi^0)$)	9,000 (11,000)	0 (0)
NC resonant ($\bar{\nu}_\mu p \to \bar{\nu}_\mu p \pi^- \, (n\pi^0)$)	0 (0)	3,900 (4,300)
NC resonant ($\bar{\nu}_\mu n \to \bar{\nu}_\mu n \pi^-$)	0 (0)	4,700 (4,300)
CC DIS ($\nu_\mu N \to \mu^- X$ or $\overline{\nu}_\mu N \to \mu^+ X$)	95,000 (92,000)	24,000 (25,000)
NC DIS ($\nu_\mu N \to \nu_\mu X$ or $\overline{\nu}_\mu N \to \overline{\nu}_\mu X$)	31,000 (31,000)	10,000 (10,000)
CC coherent π^+ ($\nu_\mu A \to \mu^- A \pi^+$)	930 (1,500)	0 (0)
CC coherent π^- ($\overline{\nu}_\mu A \to \mu^+ A \pi^-$)	0 (0)	800 (1,300)
NC coherent π^0 ($\nu_\mu A \to \nu_\mu A \pi^0$ or $\overline{\nu}_\mu A \to \overline{\nu}_\mu A \pi^0$)	520 (840)	450 (720)
NC elastic electron ($\nu_\mu e^- \to \nu_\mu e^-$ or $\overline{\nu}_\mu e^- \to \overline{\nu_\mu} e^-$)	16 (18)	11 (12)
Inverse Muon Decay ($\nu_\mu e \to \mu^- \nu_e$)	9.5 (11)	0 (0)
Total CC	170,000 (170,000)	59,000 (61,000)
Total NC+CC	230,000 (230,000)	84,000 (87,000)

Table 2.3: Possible neutrino interactions and estimated interaction rates in the Near Detector on argon (carbon) at the DUNE experiment assuming 120 GeV proton beam energy and $1 \cdot 10^{20}$ protons on target 574 m away using cross-section predictions from GENIE software.[6, 11]

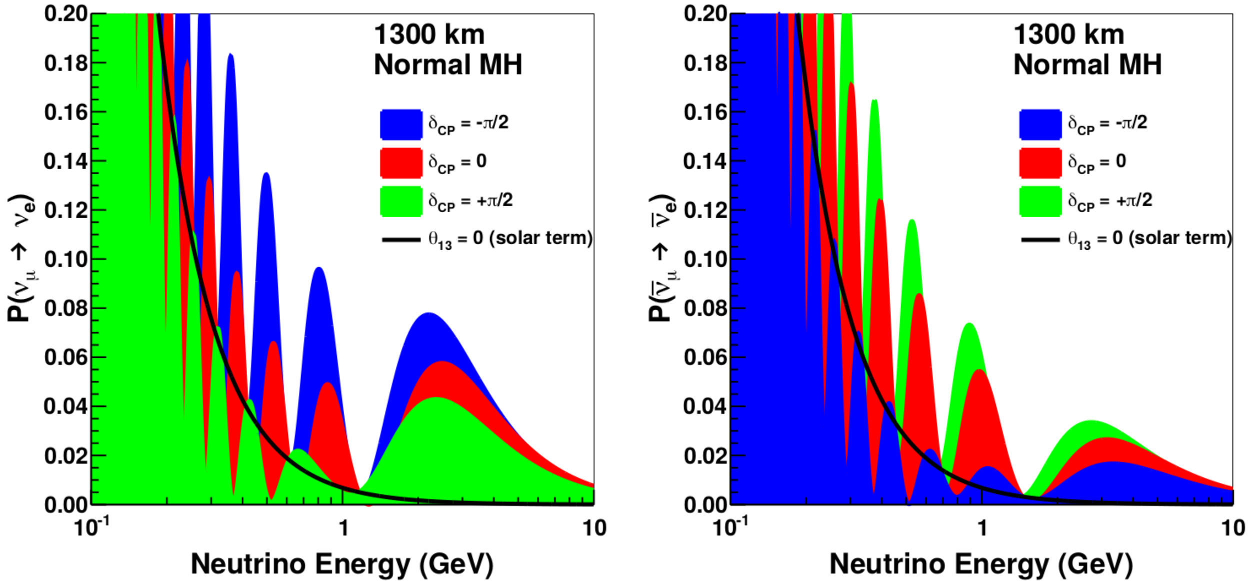

Figure 2.2: Oscillation probabilities at a baseline of 1300 km as a function of neutrino energy for neutrinos (left) and antineutrinos (right) for $\delta_{CP} = -\pi/2$ (blue), 0 (red), and $\pi/2$ (green) and normal mass hierarchy [6]. Matter effects are accounted for, which results in an additional asymmetry even at $\delta_{CP} = 0$.

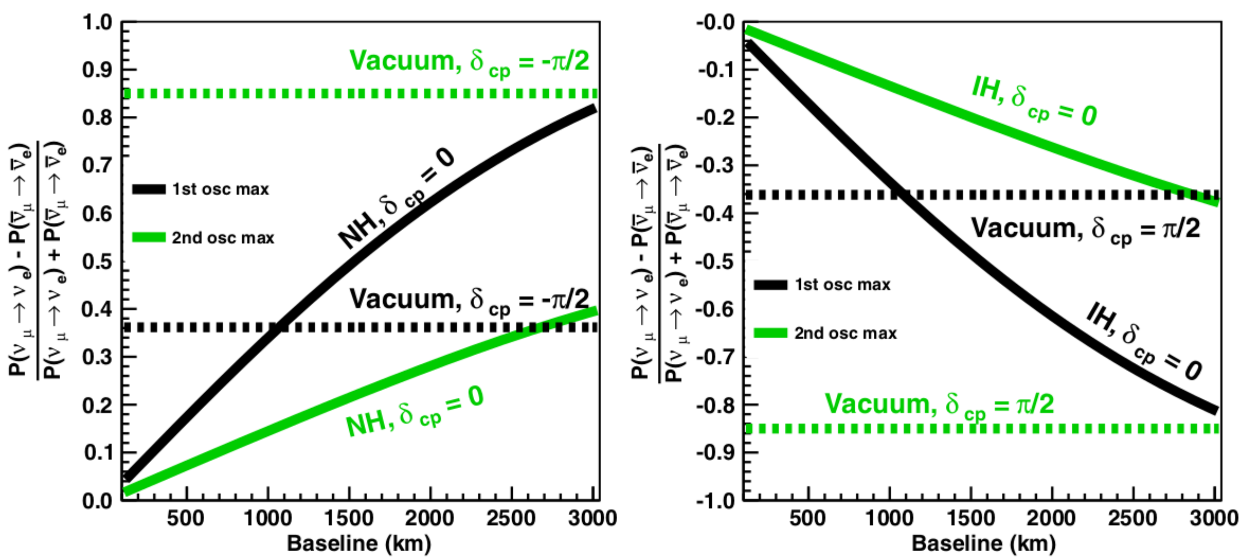

Figure 2.3: Value of $\mathcal{A}_{CP}^{\mu \to e}$ at the first and second oscillation maxima for $\delta_{CP} = 0$ with matter effects (solid line) and $\delta_{CP} = \pm\pi/2$ without matter effects (dashed line) for normal (left) and inverted (right) hierarchies as functions of baseline length [9].

2.2 Open Questions

2.2.1 Value of δ_{CP}

Present measurements of neutrino oscillation parameters have not excluded $\delta_{CP} = 0$ or π at 3σ confidence [5, 10]. This leaves open a question of whether neutrino and antineutrinos oscillate at different rates. Charge-parity violation is rare in the Standard Model [1], yet we observe dominance of matter over antimatter in the Universe. Any potential sources of CP-violation such as neutrino oscillations can help us better understand the phenomenology of this asymmetry in the Universe.

2.2.2 Neutrino Mass Hierarchy

Although cosmological models constrain the upper bound on neutrino mass to $\sum_j m_j < 0.12\ eV/c^2$ [12], the precise values for differences of neutrino masses squared Δm^2_{ij} are an open problem [6]. While Δm^2_{12} is known, the signs of Δm^2_{13} and Δm^2_{23} are undetermined [5, 6, 10]. This leads to two different orderings of the masses, known as mass hierarchies. The two mass hierarchies are normal ($m_1^2 < m_2^2 < m_3^2$) and inverted ($m_3^2 < m_1^2 < m_2^2$) [4]. The mass hierarchy is important as it affects the values and signs of oscillation parameters [5, 10]. Moreover, an inverted mass hierarchy would be unusual, since other fermions in the Standard Model increase in mass with each generation.

2.2.3 Sterile Neutrinos and Dark Matter Candidates

Several Standard Model extensions propose a new neutrino flavor that does not interact weakly, but only gravitationally [13, 14]. Standard Model neutrinos strongly violate parity: every neutrino is left-handed, while every anti-neutrino is right-handed [1]. Theories such as supersymmetry propose right-handed partners to neutrinos called sterile neutrinos [13].

Because sterile neutrinos do not interact weakly, the only way for such particles to be detected directly is through neutrino oscillations. This makes sterile neutrinos potential dark matter candidates [13]. If any sterile neutrinos exist, neutrino beamline experiments may detect discrepancies in neutrino flux compared to the one predicted using the SM and the PMNS matrix.

Chapter 3

Deep Underground Neutrino Experiment (DUNE)

3.1 Outline and Goals of DUNE

The Deep Underground Neutrino Experiment is a long-baseline neutrino experiment under construction. When operational, it will be the most advanced neutrino beamline experiment to date. The neutrino beam will be produced at Fermilab and propagate 1300 km to the SURF facility in Sanford, South Dakota, where the Far Detector is installed [7]. A schematic of the DUNE facilities is shown in Figure 3.1. The facility is planned to begin operation in the late 2020s [15].

The primary goal of DUNE is to precisely measure parameters that govern neutrino oscillations, mainly: the charge-parity violating phase δ_{CP}, the neutrino mass ordering Δm^2_{31}, and the mixing angle θ_{23}. DUNE will be capable of measuring the value of δ_{CP} at 3σ and determine

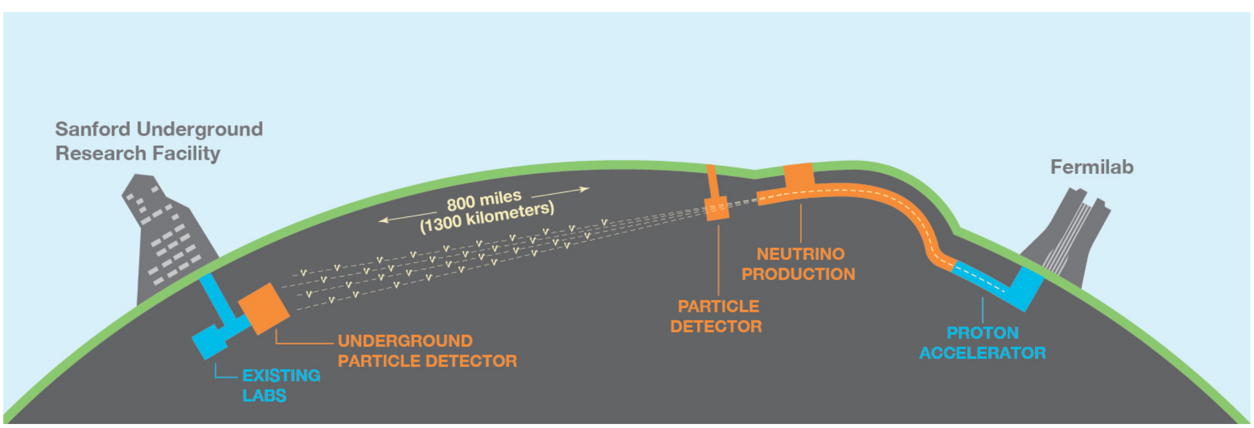

Figure 3.1: A simplified schematic of the DUNE experiment [7].

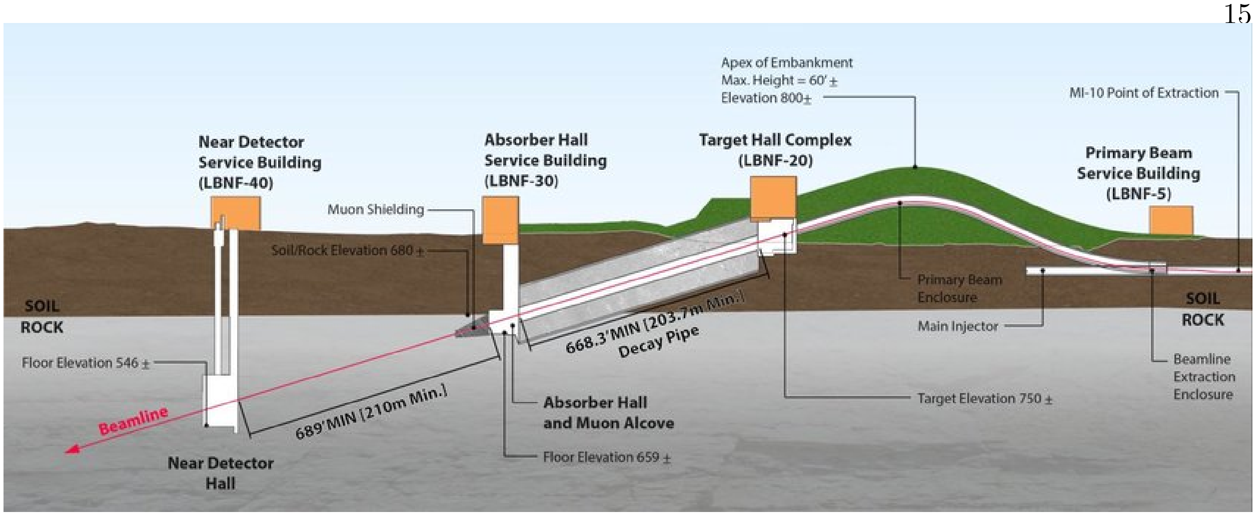

Figure 3.2: DUNE Near Site schematic [16].

neutrino mass hierarchy [6]. Additionally, DUNE will search for proton decay if any exists. Even if none occur, improved lower bounds on proton lifetime will be established [6]. Moreover, if any supernova event occurs within our galaxy within the lifetime of DUNE, the experiment will measure the incoming ν_e flux [6].

3.2 Neutrino Beam Generation

The neutrino beam generated at DUNE uses a conventional method for generation via hadron decays [16]. The Fermilab Main Injector (MI) at the DUNE Near Site accelerates protons to 60-120 GeV energy. The beam then travels to the Target Hall Complex, where it hits a solid target. Collisions with the target produce various hadrons, mostly pions and kaons [16]. The schematic of DUNE Near Site is shown in Figure 3.2.

Charged pions and kaons are then focused with electromagnetic horns to produce a hadron beam [16]. The magnetic horns focus hadrons with a particular charge, while rejecting hadrons with the opposite charge. Charge can be chosen to be either positive or negative by switching current direction. The schematic of the horn cross-section can be found in Figure 3.3. The beam then passes through the Decay Pipe, where pions and kaons decay [16].

Kaons have several decay modes with branching ratios larger than 1 per cent [3]. The decay

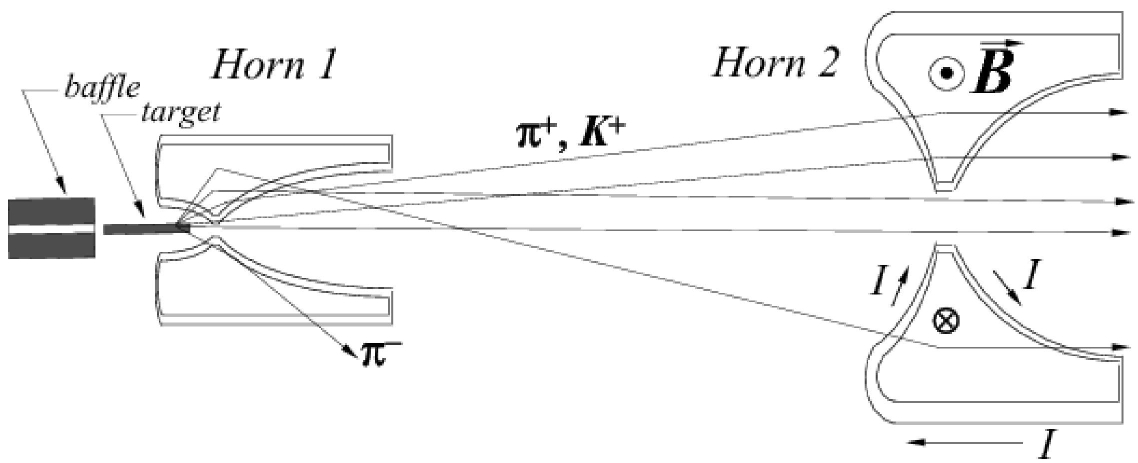

Figure 3.3: Cross-section of the magnetic horns used in the NuMI experiment [17]. DUNE will use horn design based on the NuMI designs[7].

Mode	% of decays
$\mu^+\nu_\mu$	63.56 ± 0.11
$\pi^+\pi^0$	20.67 ± 0.08
$\pi^+\pi^+\pi^-$	5.583 ± 0.024
$\pi^0 e^+\nu_e$	5.07 ± 0.04
$\pi^0\mu^+\nu_\mu$	3.352 ± 0.033
$\pi^+\pi^0\pi^0$	1.760 ± 0.023

Table 3.1: Main K^+ decay modes [3]. Decay modes with $< 1\%$ occurrence are omitted.

modes for kaons are listed in Table 3.1. Although there are multiple decay modes, most of them result in production of charged pions, neutral pions, muons and muon neutrinos, with a 5% of decays producing electrons and electron neutrinos.

Charged pions decay via the following mode [3]:

$$\pi^+ \to \mu^+\nu_\mu \text{ (99.988\% of decays)} \tag{3.1}$$

Neutral pions decay mainly via the mode [3]

$$\pi^0 \to \gamma\gamma \text{ (98.823\% of decays)} \tag{3.2}$$

and thus contribute neither to neutrino nor muon flux. Moreover, neutral pions have a short lifetime of $8.4 \cdot 10^{-17}$ s [3], and decay even before leaving the target.

In order to reduce background for muon measurements and prevent soil irradiation, hadrons that did not decay in the Decay Pipe end up absorbed in layers of either aluminum or steel at the Hadron Absorber [16]. The schematic of the proposed Hadron Absorber can be found in Figure 3.4.

This beam generation method produces a directed beam of mostly muons and muon neutrinos with a small admixture of electrons and electron neutrinos. Additionally, reversing current direction produces an antineutrino beam in a similar fashion.

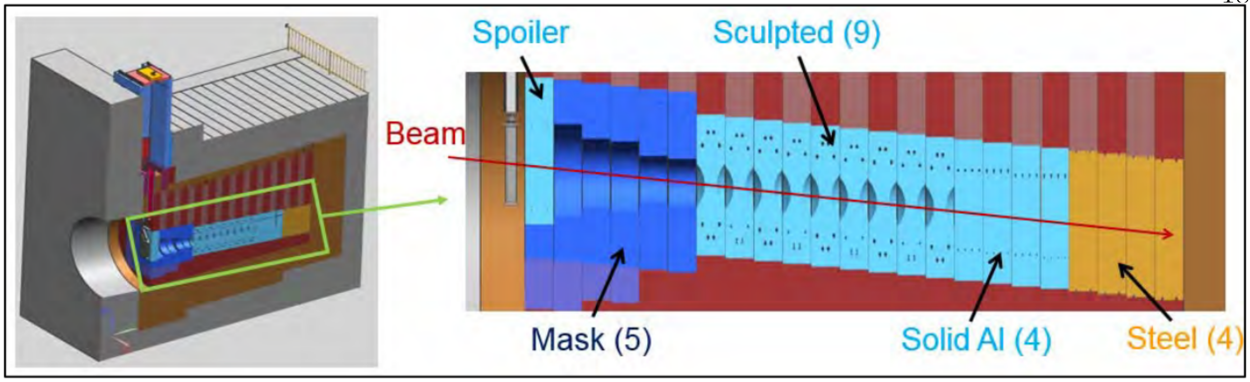

Figure 3.4: Proposed Hadron Absorber at DUNE [16].

3.3 DUNE Detectors

3.3.1 Muon Alcove

The beam, now consisting of muons and neutrinos, proceeds to the Muon Alcove. The schematic of the proposed Muon Alcove can be found in Figure 3.5. Because the expected hadron energy range and kinematics of their decay are known, gathering data about the muon flux allows to constrain the neutrino flux. DUNE is expected to measure muon flux with at most 5% error for muons above 6 GeV, which corresponds to 1.6 GeV for neutrinos in the beam [8].

For this purpose, several muon monitors are planned to be installed in the Muon Alcove to measure muon flux. They are Gas Cherenkov Monitors, Diamond Monitors, and Stopped Muon Monitors [8]. The Stopped Muon Monitors will be installed between layers of steel shielding, which is designed to slow muons down. Since muons lose energy when they pass shielding, the Stopped Muon Monitors will probe muons that had a range of initial momenta, producing measurements of flux for a spectrum of beam energies [8].

3.3.2 Near Detector

The Near Detector is planned to be installed about 0.5 km further down the beamline from the Muon Alcove to collect data on the initial neutrino flux [8]. The Near Detector will consist of a suite of neutrino detectors: Liquid Argon Time-Projection Chamber (LArTPC), discussed in

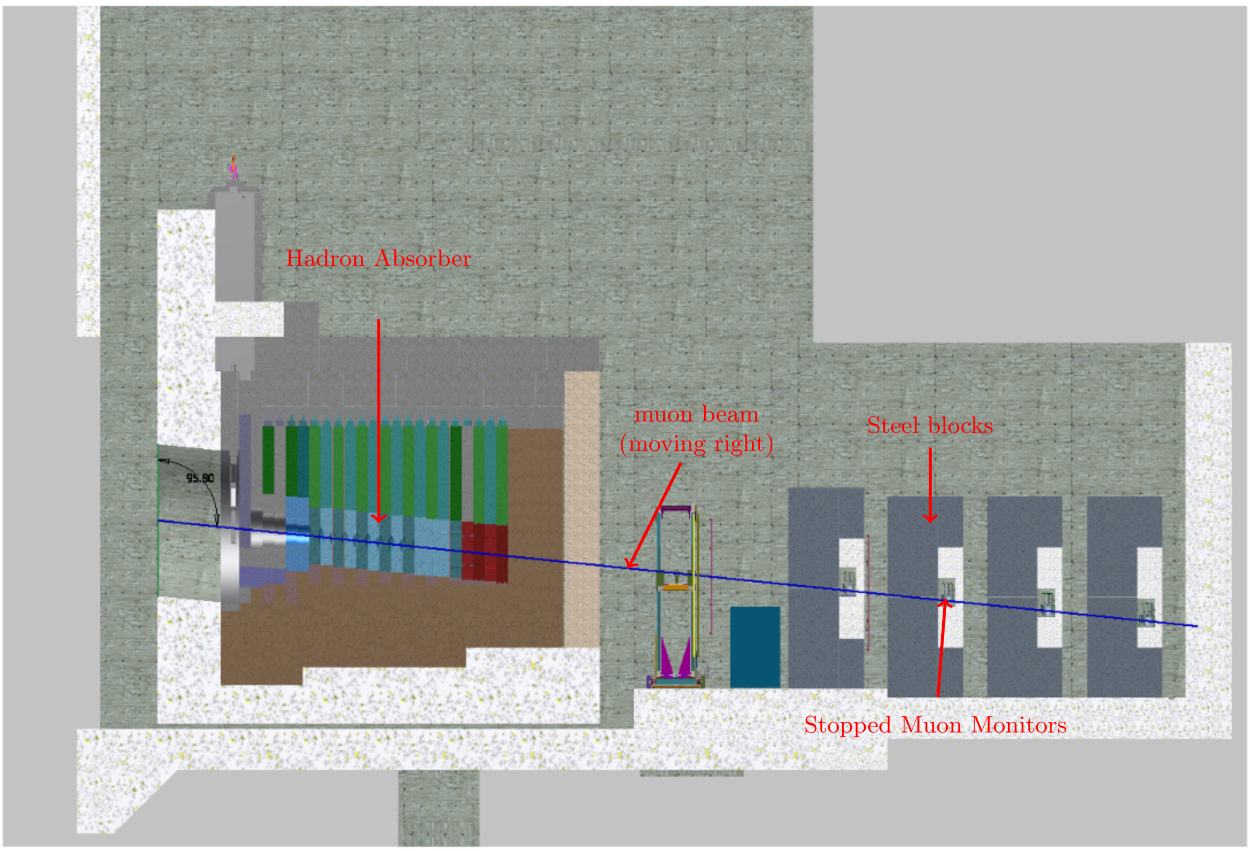

Figure 3.5: Proposed Hadron Absorber (left) and Muon Alcove (right) at DUNE with the beam profile (blue line) [8]. The Stopped Muon Monitors will be installed between blocks of steel (grey).

the subsection below, the Multi-Purpose Detector (MPD), and the Three-Dimensional Scintillating Tracker-Spectrometer (SAND) [18]. The reference design for the Near Detector can be found in Figure 3.6. These systems are implemented to compensate for a much smaller size and higher interaction rates of the Near Detector compared to the Far Detector, which results in neutrino-argon interaction products escaping the LArTPC [18].

3.3.3 Far Detector

The Far Detector is to be installed at Sanford at Homestake Mine 1300 km away from the Near Detector. It will have a fiducial mass of 40 kt of liquid argon to detect neutrinos using the Liquid Argon Time-Projection Chamber (LArTPC) technology [8]. A schematic of a cross-section of a 10 kt LArTPC designed for DUNE is shown in Figure 3.7. In the LArTPC, charged particles produced in interactions between neutrinos an argon nuclei travel through liquid argon and ionize matter on their path. The electric field between Anode Plane Assembly and Cathode Plane Assembly causes ionization charge to drift to the side of the chamber, where it is collected. This allows to get a two-dimensional track in the plane parallel to the charge collection plane. Charged matter additionally produces scintillation light, which is detected almost instantly. By recording time of each individual charge arrival, one can recreate the track in the axis perpendicular to the charge collection plane by comparing arrival times with scintillation detection times. This allows to probe depth, recreating a full three-dimensional track. Additionally, there is a magnetic field present in the chamber, making charged particles curve. By recording the magnitude of curvature and its direction, one can deduce the particle's momentum and charge respectively [8].

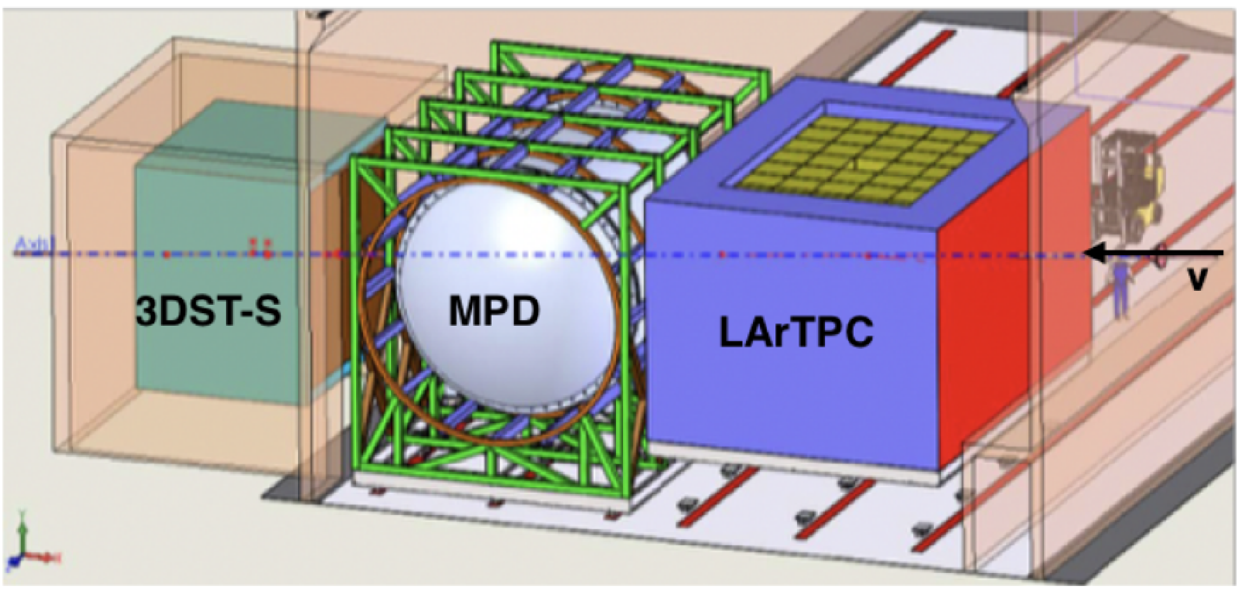

Figure 3.6: DUNE Near Detector reference design [18]. The neutrino beam is indicated by the dashed blue line.

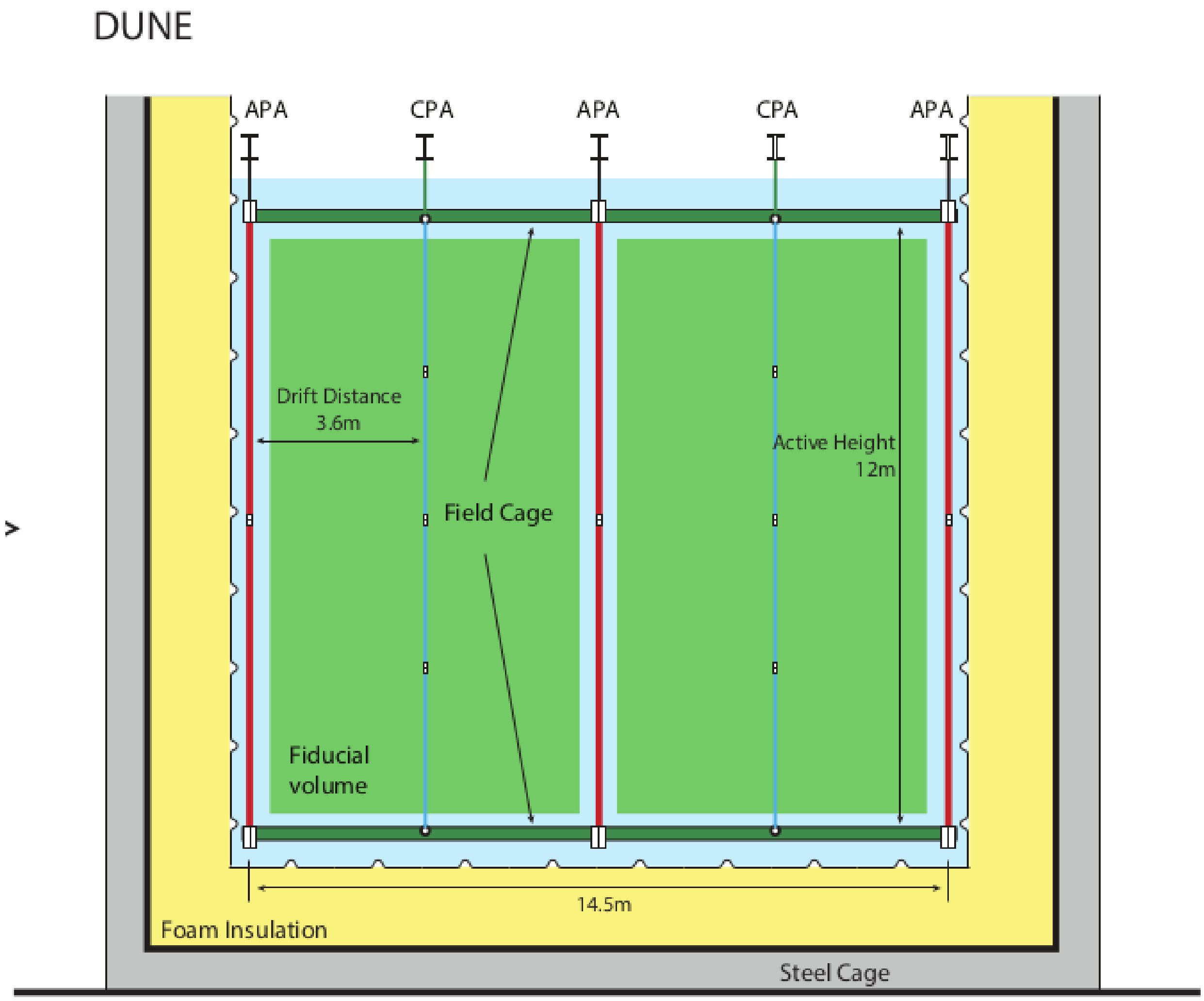

Figure 3.7: Cross section of the DUNE Far Detector 10 kt LArTPC [19]. APA stands for Anode Plane Assembly, CPA stands for Cathode Plane Assembly.

Chapter 4

Stopped Muon Monitor Description and Physics Background

4.1 Monitor Description

The Stopped Muon Monitor is a novel detector design that, rather than detecting all of the incoming muon flux like other muon monitors to be installed in the Muon Alcove, only detects muons that lost enough energy to stop completely. This gives it the advantage of being able to probe a specific energy range of the muon beam. By placing several SMMs in a cross-shaped formation, the flux distribution in the transverse plane can be estimated. Moreover, by placing several SMMs with steel blocks between them, various energy ranges can be probed. Therefore, the SMM can provide data on the muon beam flux both spatially and for multiple energy ranges.

The Stopped Muon Monitor is a bullet-shaped detector that is roughly 30 cm in diameter in all directions. It consists of two volumes: the Inner Detector (ID) and the Outer Detector (OD). The Inner Detector is completely encased by the Outer Detector, so that any particles that enter the ID have to pass through the OD first. Both the ID and the OD detect particles via light emitted from particles during travel inside the detectors. In order to collect that light, each volume has four photomultiplier tubes (PMT) attached. The ID and the OD are both encased in reflective metal shells to maximize light reflection and therefore light detection efficiency. The picture of the detector model in the Monte Carlo can be found in Figure 4.1.

The Inner Detector is designed to detect Cherenkov radiation that is produced by incoming muons and their decay products, electrons. Mineral oil is chosen because of its high refractive index $n \approx 1.46$, which in turn results in a low Cherenkov threshold of $\beta \approx 0.68$. This allows to detect

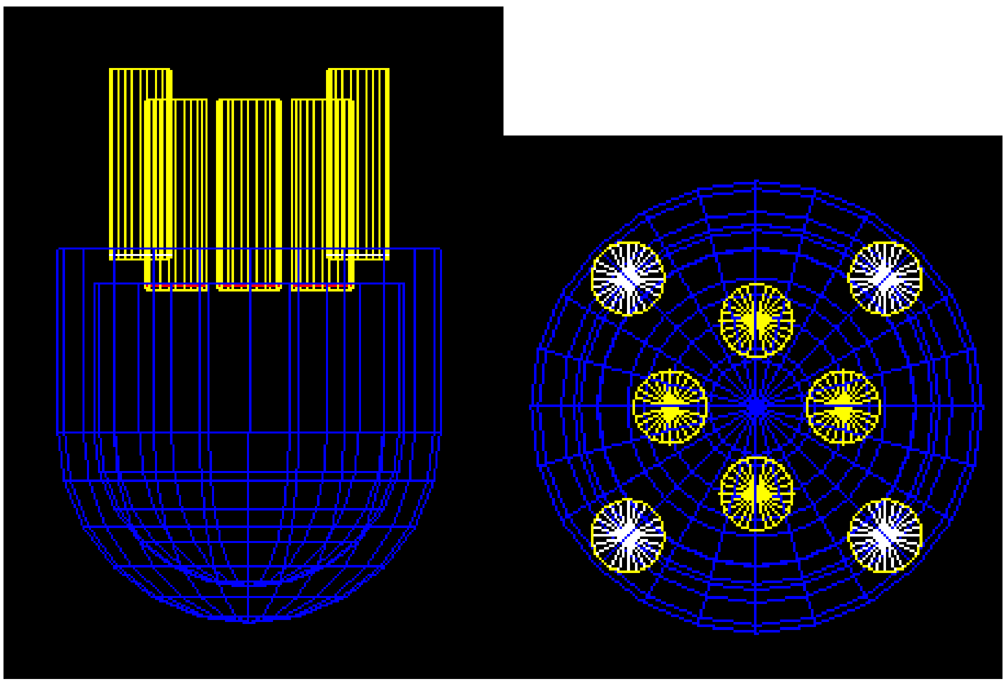

(a) (b)

Figure 4.1: Stopped Muon Monitor. View from the side (a) and from the top (b). Both the Inner and Outer Detectors are encased in metal shells (blue), and have 4 PMTs (yellow) each at the top.

incoming muons with total energy greater than 144 MeV. Electrons produced in muon decays are ultrarelativistic, and will emit Cherenkov light throughout most of their travel.

The Outer Detector is filled with toluene, an organic scintillating material. The purpose of the Outer Detector is to exclude undesired events by detecting muons and electrons coming from the Inner Detector. The time resolution on the PMTs is on the scale of nanoseconds [20], which is enough to see if a muon entered the detector after passing through the ID by looking at the time gap in PMT signal.

Before being deployed in the DUNE Muon Alcove, the Stopped Muon Monitor will be tested in the NuMI beamline. Before deployment at NuMI, the SMM prototype is tested at the University of Colorado Boulder using cosmic ray muons to collect data. One advantage of testing the SMM in Boulder is the increase in cosmic muon flux due to high altitude of 1600 m above sea level. Thus cosmic rays provide a natural and readily avaliable source of muons to test the SMM.

In order to evaluate the performance of the SMM in the NuMI, a Monte Carlo simulation of the SMM is desirable to compare data with. However, the Monte Carlo first has to match the data from cosmic ray muon tests at the University of Colorado. Therefore, a simulation of the SMM exposed to cosmic ray muons is needed.

4.2 Physics Background

4.2.1 Photomultiplier Tubes

The Stoppped Muon Monitor detects particles inside of it using light collected by photomultiplier tubes. PMTs consist of a photocathode, an anode, and multiple dynodes between them [20]. When a photon hits the photocathode, it may knock off an electron via photoelectric effect. The electron is then accelerated towards the first dynode, where it collides with enough energy to produce multiple electrons. These electrons then proceed to the second dynode and so on. As a result, multiple electrons arrive at the anode, with total energy much greater than the initial electron from the photocathode. This allows to detect faint light signals with high precision. However, PMTs are limited in the range of wavelengths they are sensitive to [20]. This is characterized by quantum efficiency, which is the ratio of photons that produced an electron in the photocathode. The graph of quantum efficiency vs wavelength for the PMT used in the SMM can be found in Figure 4.2.

4.2.2 Cosmic Ray Muons

The SMM prototype at the University of Colorado uses cosmic ray muons to collect data. Cosmic rays are various high-energy particles produced in astrophysical interactions in the upper Earth atmosphere. Muons constitute the majority of cosmic ray flux on the ground [3].

The mean energy of muons at sea level is about 3-4 GeV. A small portion of the muon flux is in the MeV range of energies, which are small enough for muons to stop in the SMM. In the MeV range, the energy distribution of muons is uniform [3].

While the energy distribution of MeV muons is known, there is little data on the angular distribution of these muons. For cosmic ray muons with mean energy of 3 GeV, the differential flux per solid angle is known to be proportional to $\cos^2\theta$, where θ is the particle zenith angle [21]. The zenith angle is 0 for particles traveling straight down, and $\pi/2$ for particles traveling parallel to the horizon. Plot of angular distributions of muons with momenta in the range 1-1000 GeV can be found in Figure 4.3. As muon energy decreases, the angular distribution becomes steeper, with less muons at high zenith angles. It is therefore expected that the angular distribution at the MeV range is significantly steeper than for 3 GeV muons.

4.2.3 Passage of Muons Through Material

Muons passing through matter lose energy primarily through ionization [3]. As a charged particle travels through matter, the Coulomb forces between the particle and electrons in an atom may be strong enough to ionize the atom. The resulting energy loss of the passing particle is described by the Bethe formula [3]:

$$-\left\langle \frac{dE}{dx} \right\rangle = Kz^2 \frac{Z}{A} \frac{1}{\beta^2} \left(\frac{1}{2} \ln \frac{2m_e c^2 \beta^2 \gamma^2 T_{max}}{I^2} - \beta^2 - \frac{\delta}{2} \right) \tag{4.1}$$

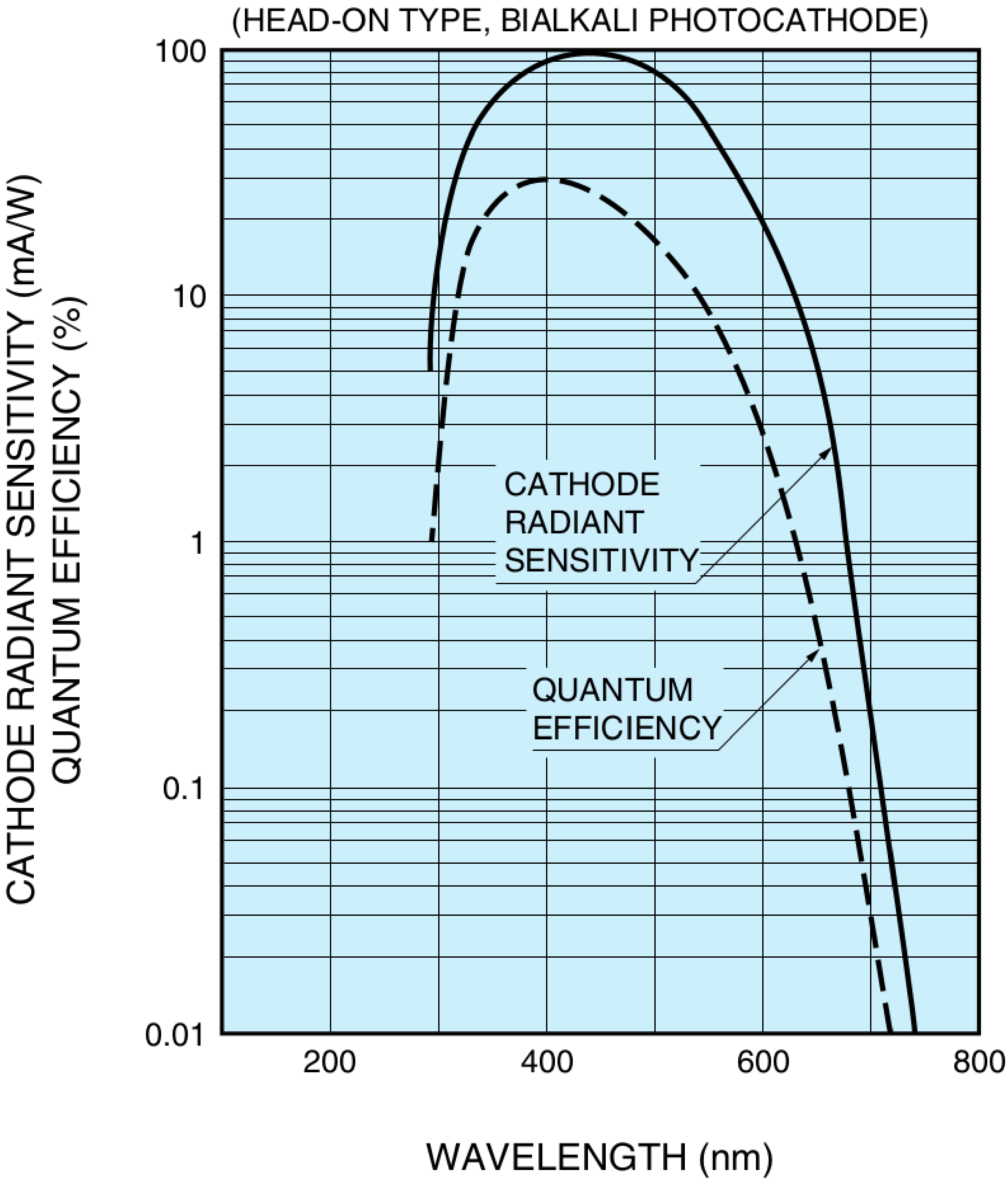

Figure 4.2: PMT quantum efficiency (dashed line) versus photon wavelength for a bialkali photocathode [20] used in the SMM PMT. At wavelengths less than 300 nm, glass on the photocathode becomes opaque.

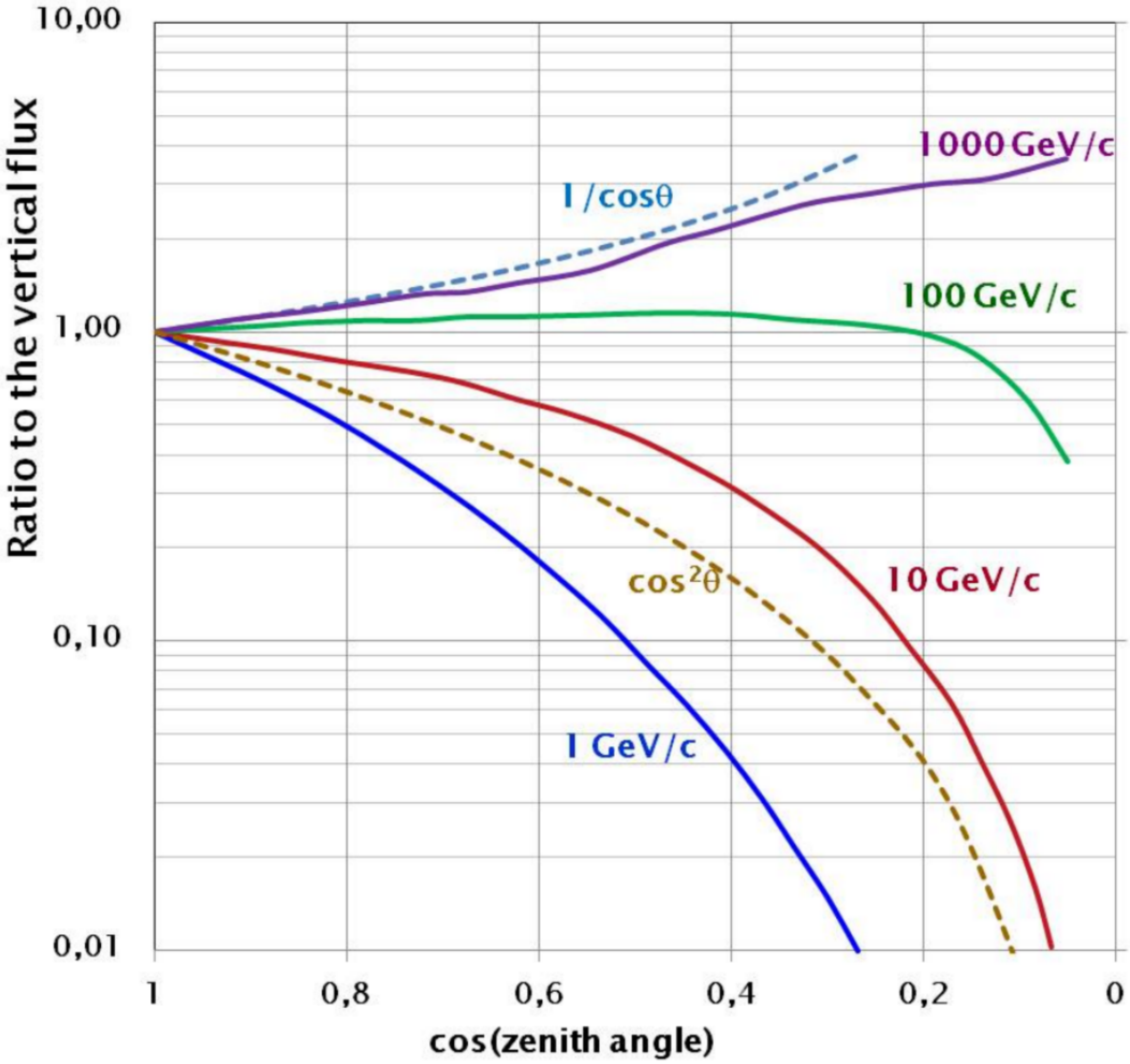

Figure 4.3: Cosmic ray muon flux distribution versus muon zenith angle [21]. Solid lines represent data at various muon momenta. Dashed lines are reference distributions for differential flux being proportional to $\cos^2\theta$ (orange) and $\cos^{-1}\theta$ (blue) respectively.

where $\langle dE/dx\rangle$ is mean energy loss per distance, K is, z is, Z and A are atomic number and weight of the material respectively, T_{max} is the maximum kinetic energy that can be transferred to an electron in a collision, I is mean excitation energy, and δ is a relativistic parameter that gets significant at the ultrarelativistic limit $\beta\gamma >> 1$. The graph of muon stopping power versus momentum is shown in Figure 4.4. For the energy distribution used in the Stopped Muon Monitor Monte Carlo ($\approx$ 100 MeV/c), muons experience exponentially less stopping power the more momentum they have. Therefore, one expects an upper threshold on muon momenta, where muons below the threshold stop, while muons above the threshold do not lose enough energy and escape the SMM.

4.2.4 Scintillation

Passing muons will be detected in the SMM using scintillation light emitted by them in the Outer Detector. Scintillation is a phenomenon where a charged particle passing through certain crystals and organic materials causes them to emit light [22]. The emission rate is governed by Birks' Law [22]:

$$\frac{dL}{dx} = S\frac{dE/dx}{1 + k_B dE/dx} \tag{4.2}$$

where dL/dx is light yield per distance, S is scintillation efficiency, dE/dx is energy loss per distance, and k_B is Birks' constant, which depends on the scintillating material. In the lower limit $dE/dx << k_B^{-1}$, Birks' law can be approximated as a simple proportionality relation

$$\frac{dL}{dx} \approx S\frac{dE}{dx} \tag{4.3}$$

while in the upper limit $dE/dx >> k_B$, light yield becomes constant

$$\frac{dL}{dx} \approx \frac{S}{k_B} \tag{4.4}$$

For the scintillator used in the experiment, toluene, $k_B^{-1} \approx 8\ MeV/mm$, which is considerably larger than muon energy loss when passing through matter [3]. Therefore the lower limit can be used, so scintillation light yield is proportional to the energy loss of the muon.

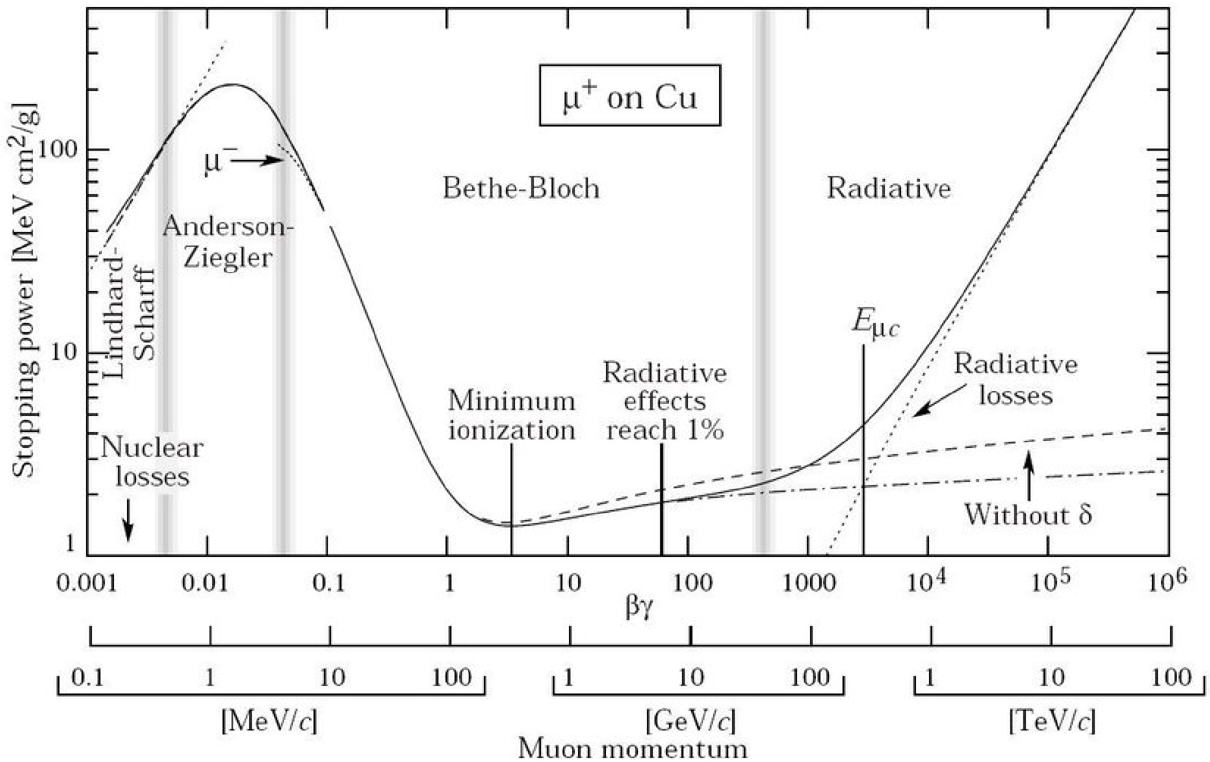

Figure 4.4: Muon stopping power when passing through copper [3].

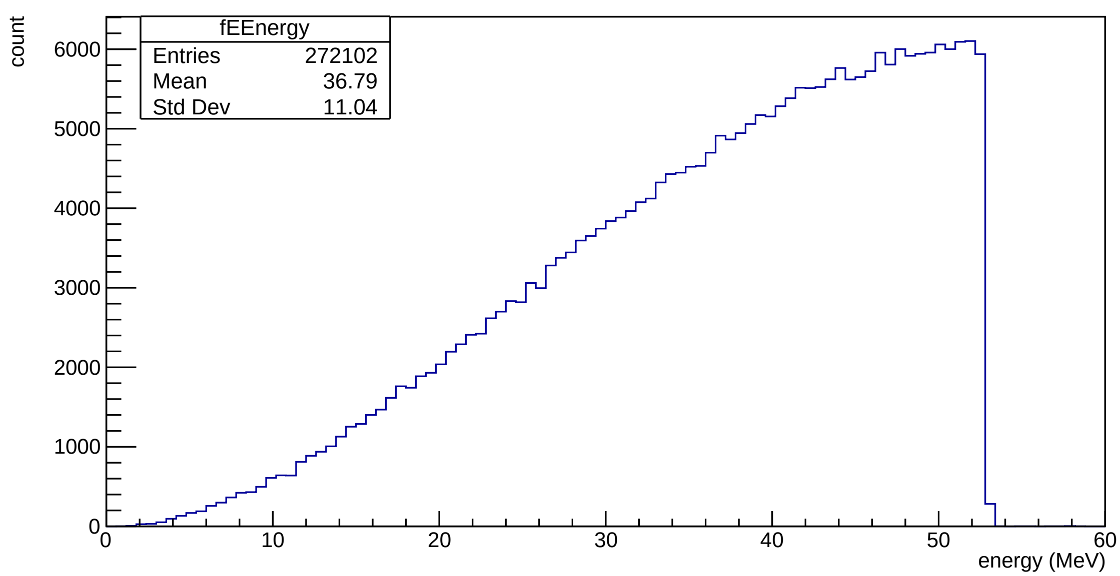

Figure 4.5: Energy spectrum of Michel electrons. Data obtained from Geant4 simulation.

4.2.5 Muon Decays

As muons pass through the SMM and lose energy, they may eventually stop inside the detector. Muons are second-generation charged leptons, and as such, are unstable. Their mean lifetime is 2.20 μs [3]. Muon decay happens almost exclusively via the following mode [3]:

$$\mu^- \rightarrow e^- \bar{\nu}_e \nu_\mu \text{ } (\approx 100\% \text{ of decays}) \tag{4.5}$$

The precise kinematics of the secondary particles in muon decays can be derived analytically [3]. The energy distribution of the decay electron is well-known and follows the Michel spectrum. The graph of Michel spectrum can be found in Figure 4.5. Since the mean energy of Michel electrons is much greater than the electron mass, Michel electrons travel close to the speed of light, which makes them emit Cherenkov radiation when traveling in the Inner Detector.

4.2.6 Cherenkov Radiation

Cherenkov radiation is a phenomenon, where a particle traveling in a medium with a refractive index $n > 0$ at a speed exceeding the speed of light in the medium c/n emits photons [3]. This phenomenon has been known since the 1930s and has become a useful charged-particle detection tool.

Cherenkov radiation travels in a cone, whose center axis is collinear with the momentum vector. The cone's half angle θ is given by:

$$\cos\theta = \frac{1}{\beta n} \tag{4.6}$$

where β is fraction of particle's speed relative to the speed of light in vacuum [3]. For ultrarelativistic particles like Michel electrons, $\beta \approx 1$, and so the angle is constant in a uniform material.

The number of Cherenkov photons N emitted per unit distance dx per unit wavelength $d\lambda$ is given by

$$\frac{d^2N}{dx d\lambda} = \frac{2\pi\alpha z^2}{\lambda^2}\left(1 - \frac{1}{\beta^2 n^2}\right) \tag{4.7}$$

where α is the fine-structure constant, z is particle charge [3]. This formula produces a characteristic wavelength distribution of Cherenkov light, which can be found in Figure 4.6. A significant portion of the light is ultraviolet ($< 380\ nm$), but the mean wavelength is about 420 nm, which gives Cherenkov light a peculiar blue color. Notably, PMT photocathodes are opaque to a large portion of the high-frequency spectrum [20], so some light from Michel electrons is not detected in the PMTs.

4.2.7 Muon Capture

Occasionally, muons that completely stop may be close enough to a nucleus that the muon is attracted to the nucleus in a process called muon capture [23]:

$$\mu^- p \to \nu_\mu n \tag{4.8}$$

The neutron produced in muon capture is electrically neutral and produces no Cherenkov or scintillation photons. Muon capture chance can be estimated by comparing mean lifetimes of a muon τ_{μ^-} and antimuon τ_{μ^+} in material. The longer a muon spends inside a material the higher the chance that it gets captured. Therefore muon capture reduces muon lifetime. The capture chance can be estimated as

$$\frac{\tau_{\mu^+} - \tau_{\mu^-}}{\tau_{\mu^+}} \tag{4.9}$$

From the data available on muon lifetimes in various materials [23], muon capture rate is $(8.0 \pm 0.9)\%$ for carbon, the main element by mass in mineral oil and toluene; and $(90.8 \pm 0.2)\%$ for iron, the main component of the metal shells in the SMM.

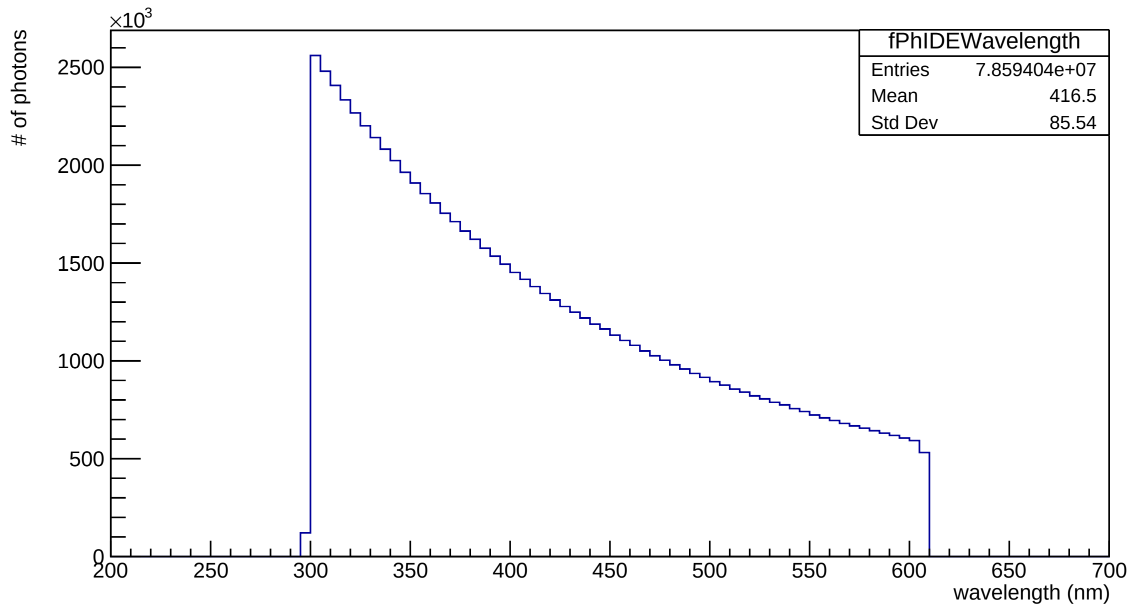

Figure 4.6: Wavelength spectrum of Cherenkov light emitted by a Michel electron in mineral oil. Data obtained from Geant4 simulation.

Chapter 5

Monte Carlo Setup and Results

5.1 Monte Carlo Setup

The Monte Carlo simulation in this paper uses CERN's Geant4 toolkit. Geant4 is a C++ suite used for particle physics simulations. The user sets up physics models, detector geometry, and particle generation algorithm to create a simulation [24].

Monte Carlo simulation in this paper uses pre-built Geant4 physics classes, which provide physics models of quantum electrodynamics, muon decay, and muon capture. Together, these provide everything required for muons in the simulation to stop and decay, while emitting optical photons.

The detector geometry in the Monte Carlo is based on the dimensions and material composition of the SMM prototype at the University of Colorado Boulder. The geometry includes PMTs, where photons hitting a photocathode volume are tallied to compute signal in PMTs.

The various tests performed below all use a similar setup for muon generation. The simulation aims to realistically model cosmic ray muon flux for low energy muons. In the Monte Carlo, muons are uniformly generated on a disk 40 cm above detector center, just above the PMTs. The disk radius in the main test is 60 cm. This choice of radius of is discussed in Section 5.2.2. Muon momentum is uniformly distributed in the azimuthal plane, because there is little dependence of cosmic ray muon flux on the azimuthal angle. Muon momentum depends on the polar angle, also called zenith angle, using the assumption that the differential flux per unit steradian is proportional to $\cos^2\theta$, where θ is zenith angle. This choice of polar dependence of muon momentum is discussed in Section 5.2.1. The initial muon kinetic energy is uniformly distributed between 0 and 150 MeV in all tests. The upper bound of 150 MeV was chosen by empirically as energy at which muons no longer stop in the SMM. There are $5 \cdot 10^7$ muons simulated in the main test with one muon per event. Muons are generated in ratio of two μ^+ for every μ^-.

These muons are simulated in Geant4 using several subdivisions of a simulation. The largest unit of Geant4 simulation is a run: physics and geometry are initialized once during the beginning of a run, and are then followed by events. An event generates a particle with pseudorandom position and momentum distributions specified by the user. This primary particle then travels and interacts with other objects in the simulation such as detector volumes or other particles produced in interactions. The smallest unit of a simulation is a step. Interactions occur during steps, and most of the data tracked after the beginning of an event is tracked using steps [24].

The data is tracked during the course of either a run, an event, or a step. In the main test, the Monte Carlo tracks muon and Michel electron 4-positions and 4-momenta on emergence, and when they enter either ID or OD. The total number of photons that hit all PMTs in either ID or OD is tracked. Since the voltage output of the PMTs increases with photon flux on the photocathode, I define “signal in ID” and “signal in OD” to be that total number of photons in 4 PMTs in the ID and the OD respectively. Moreover, I will refer to signal from photons as “muon signal” if these photons were emitted before muon decay, and “electron signal” if the photons were emitted after the decay. Each individual photons’ wavelength on arrival to the PMTs is also tracked.

The muons and Michel electrons have vastly different kinematics and behavior in the simulation, but both produce photons when moving in the SMM. Therefore, the signal in the PMTs needs to be separated by particle of origin. This is done in the simulation by tracking the time of muon decay during an event. Every photon detected in the PMT before the decay is counted as having originated from a muon, while a photon detected after the decay is counted as having originated from an electron.

The tracked data is then collected and analyzed using CERN’s ROOT software. ROOT is a C++ library that allows to manage ntuples, make histograms, and selection cuts [25]. Ntuples are data structures, where data from each event is uniquely stored as a list of values. By setting limits on a subset of values, a user can sieve out unwanted events. This sieving process is used to make selection cuts on data.

5.2 Preliminary Tests

There are two parameters in the setup discussed above that require tests to determine their values. Cosmic ray flux depends on the zenith angle. Therefore two models of angular flux distribution were tested in Section 5.2.1. The radius of the disk, where muons are generated, is chosen in Section 5.2.2 by making sure that most of the muons that could potentially reach the detector are simulated.

5.2.1 Zenith Angle Dependence Test

Cosmic ray muons have a non-constant angle distribution. The distribution depends on the muon momentum. This dependence is discussed in Section 4.3.1. Currently, there is very little research on the angle distribution of low-energy (< 1 GeV) cosmic ray muons. Therefore, two models for the angle distribution were tested.

In the first model, data curves in Figure 4.2 are fit to a power function

$$I = Acos^{n}\theta \tag{5.1}$$

and then the values of n for each curve are fit to a polynomial of the logarithm of muon momentum:

$$n = 3.5 - 2.158\log_{10} p + 0.215(\log_{10} p)^2 \tag{5.2}$$

To account for the divergence at zero momentum, muons with momentum less than 0.1 MeV/c were given a constant power of 6. I will refer to this model as the polynomial model for the rest of the discussion.

The second model assumes that differential flux per steradian is proportional to $\cos^2\theta$ as in Figure 4.3. This distribution is much simpler, and does not extrapolate data, but is not accurate for MeV muons. However, since the detector is not very oblong, and since in both models the majority of muons come straight down, it was hypothesized that models will not show significant differences in signal.

The plots of the angle distribution of muons that entered the SMM are shown in Figure 5.1. As expected, the polynomial model produces a much steeper distribution with most muons almost vertical. The $\cos^2\theta$ distribution is shallower, but nevertheless most muons are relatively close to vertical.

The resulting muon momenta distributions in the xz-plane for both models are shown in Figure 5.2. Similar to Figure 5.1, muons in the polynomial model have more momentum in the z-axis compared to $\cos^2\theta$ and less momentum spread in the xy-plane.

The signal versus energy distributions for muons and Michel electrons are shown in Figure 5.3. While slightly different, the signal distributions do not vary much between the two models. The means and standard deviations for muon signal in the OD and the ID, and for electrons in the ID are all within 1 standard deviation of each other. The shapes of these distributions does not change significantly. While in the polynomial model 14% of muons entering the SMM decay in the ID, only 11% of muons do so in the $\cos^2\theta$ due to more muons being more vertical and therefore traversing more distance in the SMM. However, the number of decayed muons only affects the rate of data collection in the SMM prototype, but not the signal itself.

Because the only experimentally measurable quantity, PMT signal, did not vary significantly with angle distributions, I chose the $\cos^2(\theta)$ distribution, since there is data available near this distribution in Figure 4.2, while my polynomial fit model is speculative and extrapolated.

5.2.2 Initial Muon Distribution Radius Test

After the $\cos^2\theta$ model was chosen for the simulation, an appropriate radius for the disk was empirically found. To include as complete of a dataset as possible, the cutoff for the disk radius was chosen to be three standard deviations radially away from the center of the disk for muons that reached the SMM. The plot of xy-position of muons that reached the SMM is shown in Figure 5.4.

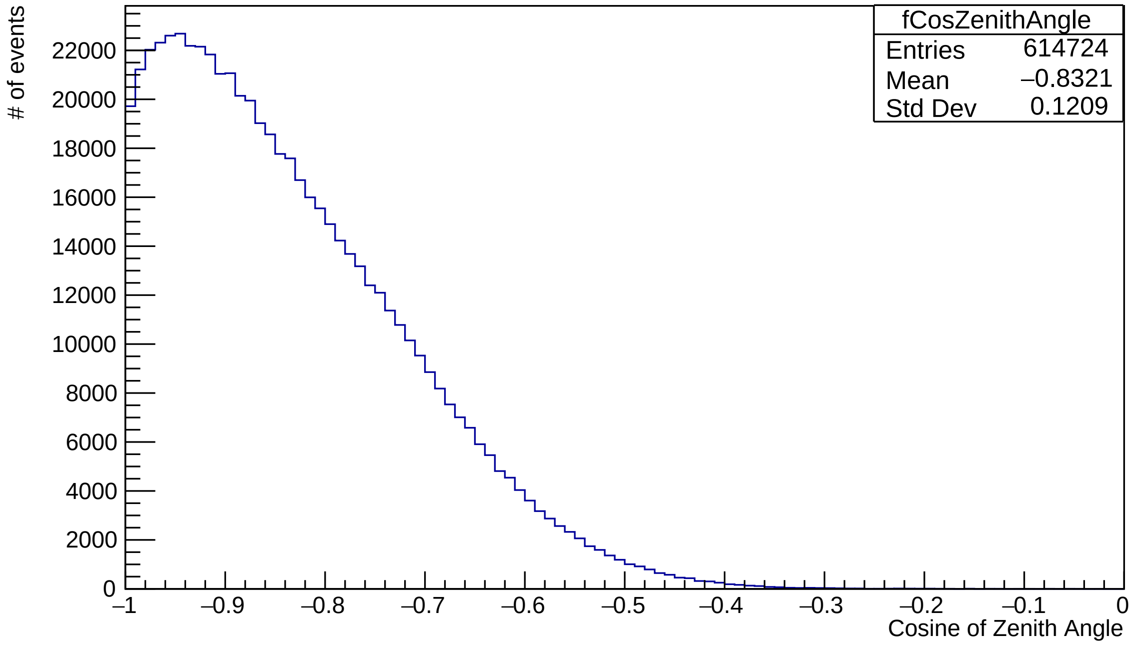

(a)

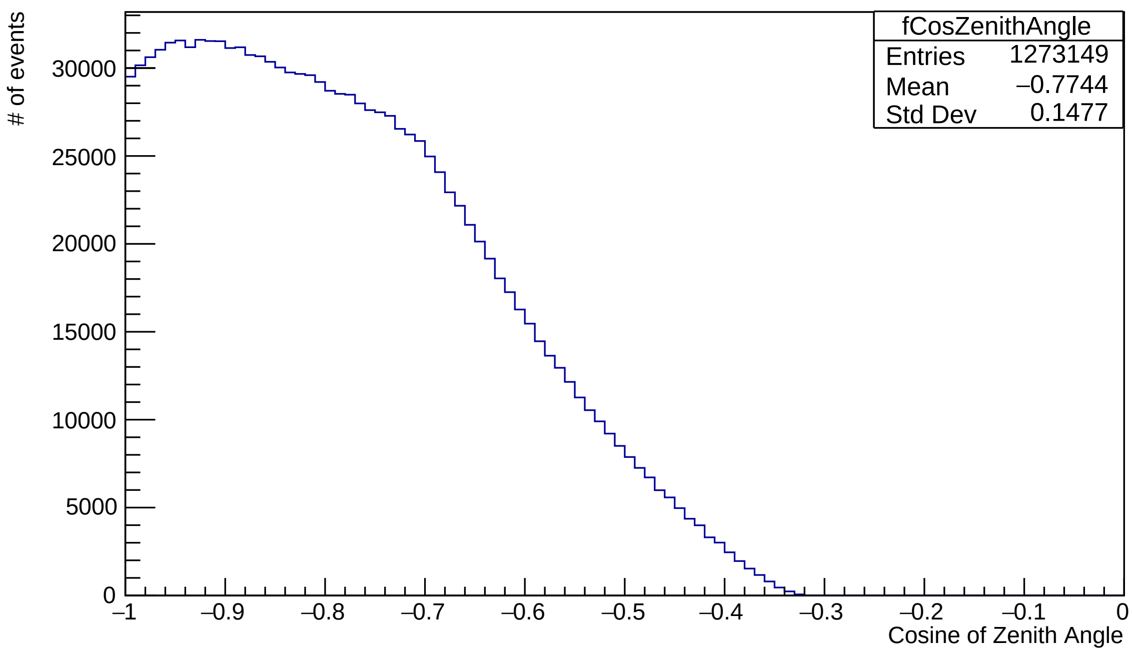

(b)

Figure 5.1: Cosine of zenith angle distribution for muons that hit the SMM for the polynomial (c) and $\cos^2\theta$ (d) fits.

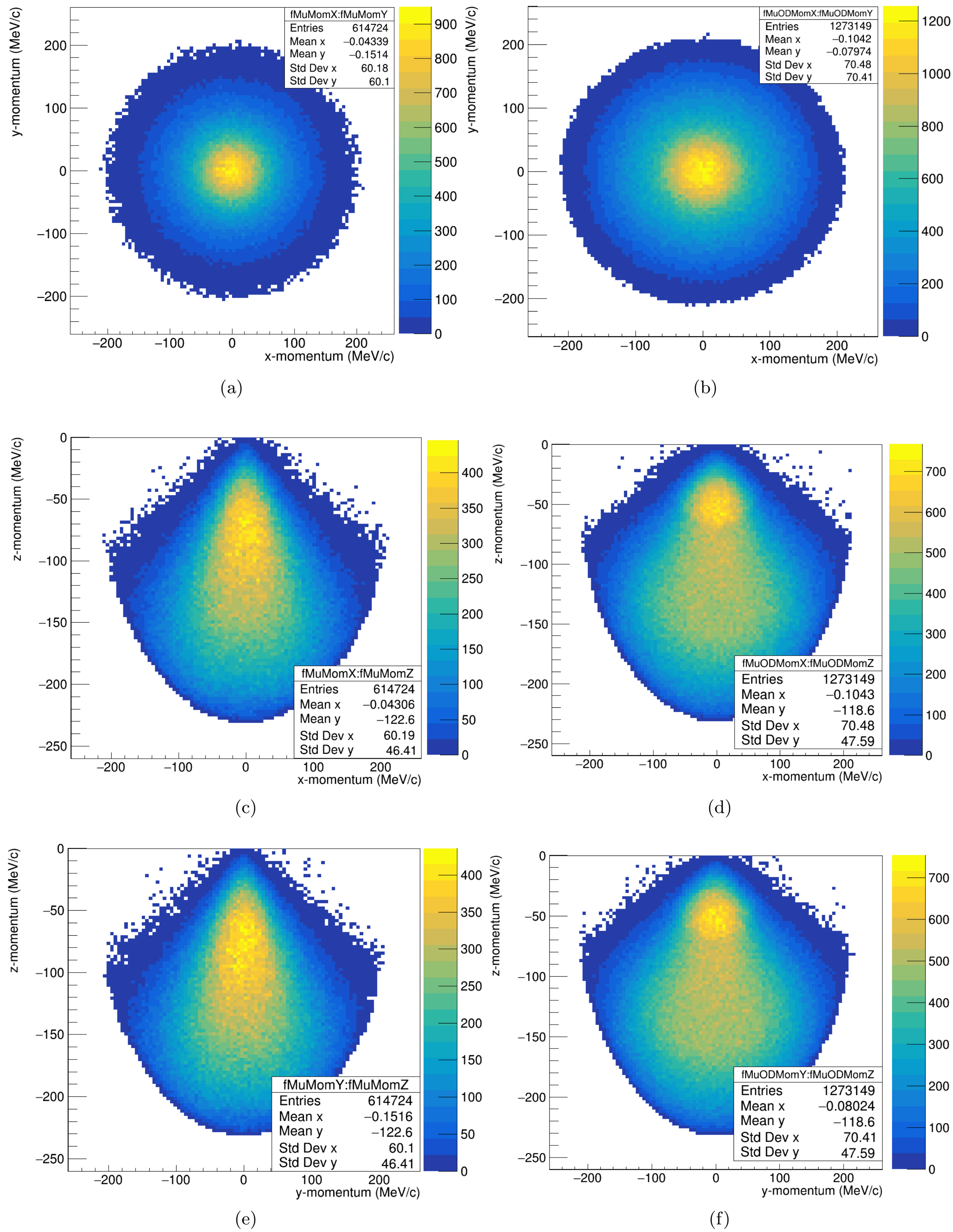

Figure 5.2: Projections of muon momentum on entry to the SMM in the xy (a,b), xz (c,d), and yz (e,f) planes for the polynomial (a,c,e) and $\cos^2\theta$ (b,d,f) models. Enlarged plots in Appendix.

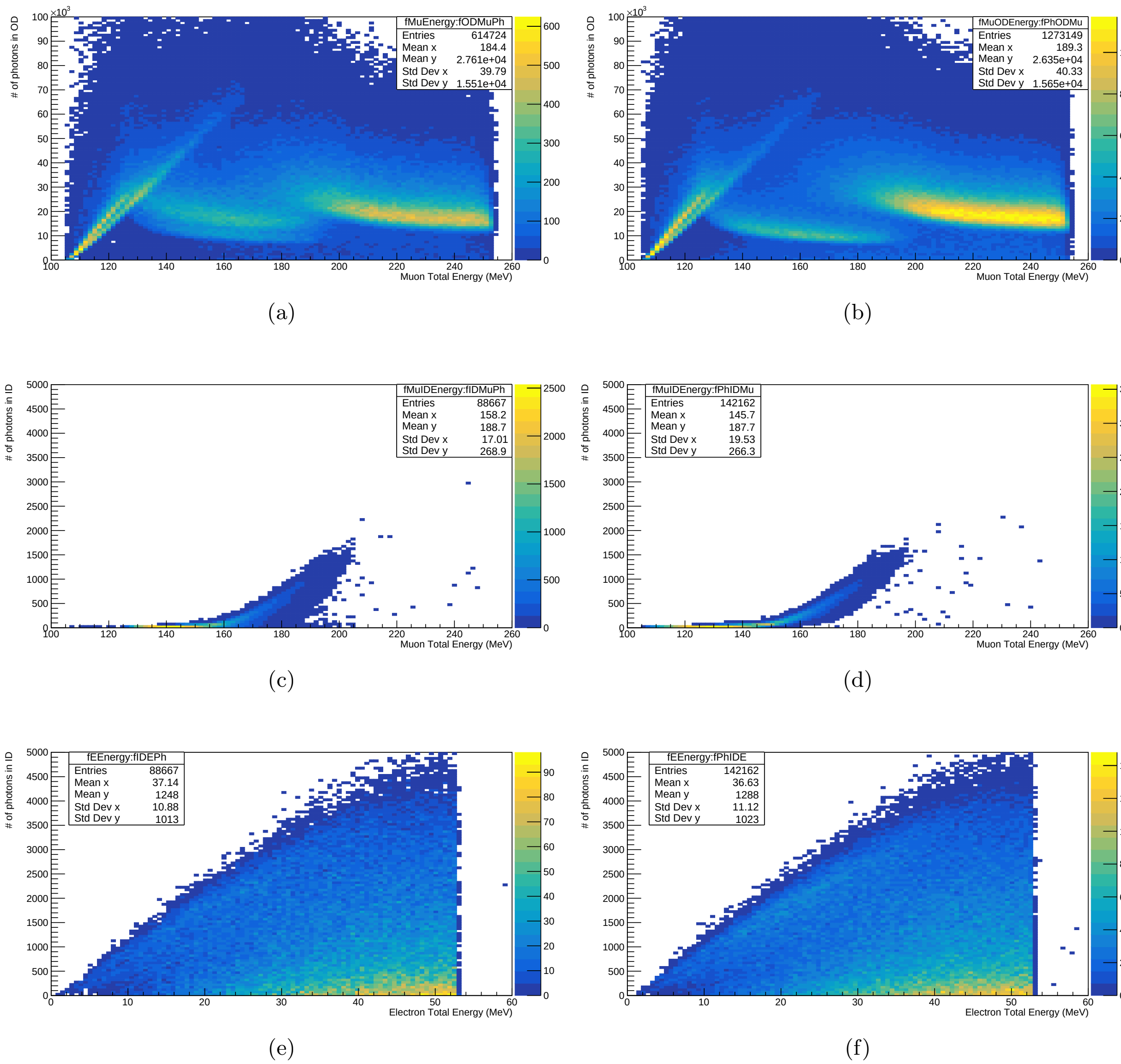

Figure 5.3: Signal vesus particle total energy of muons in OD (a,b), muons in ID (c,d), and electrons in ID (e,f) for the polynomial (a,c,e) and $\cos^2\theta$ (b,d,f) models. Enlarged plots in Appendix.

Since the standard deviation is 22.6 cm, 60 cm was chosen as a radius for the disk, so that most of the muon flux reaching SMM is simulated. This resulted in a 2.4% hit rate for muons in the Monte Carlo. Even though this is a small hit chance, Geant4 takes little computational time to simulate muons in air, and ROOT's ntuple compression algorithms result in almost no extra memory space taken up by events, where a muon missed the SMM.

5.3 Main Test

5.3.1 Dataset Partitions

While only the total photon flux is measured in the PMTs, a set of selection cuts can help make physical sense of the data by looking at the trajectory that a muon and its decay electron traveled. More precisely, the signal in the Inner and Outer Detectors will depend on the order of detectors (ID and OD) which each muon and its Michel electron entered chronologically. Therefore, the dataset was partitioned into 13 selection cuts based on the detector entry chronology. These cuts are labeled using the following scheme:

(1) For each detector (either ID or OD) a muon entered, chronologically add the first letter of that detector to the cut label.

(2) Label the fate of the muon by letters ϵ (muon escaped), κ (muon got captured), or δ (muon decayed).

(3) For decays (δ), add the first letter of the detector where the muon decayed.

(4) If the daughter Michel electron entered other detectors, label them chronologically similar to (1).

For instance, if a muon stopped in the ID, decayed, and the Michel electron escaped the detector, that event would be in the $OI\delta IO$ cut. In this context, I define an event as "contained" if it is $OI\delta I$, "uncontained" otherwise.

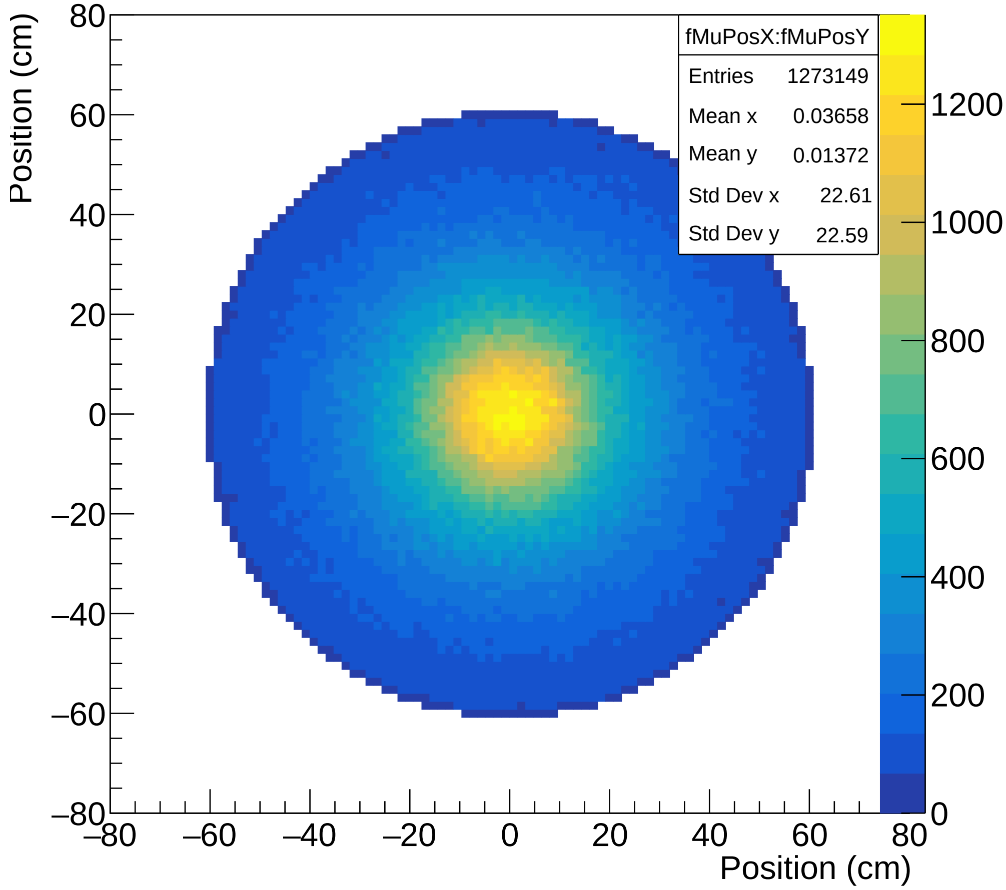

Figure 5.4: Initial xy-position of muons that hit the SMM in the Monte Carlo with $\cos^2\theta$ zenith angle distribution

The ratios of events for each of these cuts can be found in Table 5.1. The corresponding pie charts can be found in Figure 5.5. The majority of muons, 75.3%, escape the detector. Muons that stop (24.7%) then either decay (22.4%) or get captured (2.3%). Of events, where a muon decayed, 52.3% and 47.7% decayed in the ID and the OD respectively. Contained events ($OI\delta I$ cut) account for 3.5% of all SMM hit events, 15.5% of all decays, and 29.6% of all decays in the ID.

Because the ratio of muons to antimuons is 1-to-2 in the Monte Carlo, the capture rate for μ^- is $(30.9 \pm 0.2)\%$, which is significantly higher than the expected rate of $(8.0 \pm 0.9)\%$. This increase in capture rate could be caused by additional capture in much denser steel shell between the ID and the OD, where capture rate is $(90.8 \pm 0.2)\%$. This is further supported by an increased relative number of $OIO\kappa$ events, which account for 21.3% of captures; when compared to $OIO\delta$ events, which only account for 10.3% of decays. This increase could be due to muons passing through steel on escape from the ID for OIO events. Additionally, there are many more muon captures in the OD than in the ID: 68.2% and 31.8% respectively. This may be because some muons that could have escaped were captured instead. Since all muons that could escape have to travel through the OD, but only 56% travel through the ID, this would increase the rate of muon capture in the OD relative to the ID compared to muon decay. This factor may contribute the overall increase in capture rate compared to the expected $(8.0 \pm 0.9)\%$.

5.3.2 Muon Signal

I will consider signal produced by muons in the OD and the ID to look for particular features in the signal distribution that indicate SMM geometry. First, the signal for a muon entering the OD for various partitions is shown in Figure 5.6. These histograms show some features that we can use to make sense of the physics in the Monte Carlo.

Contained events (Figure 5.6(b)) are clustered in the range of 130 - 210 MeV with mean total energy of 157.9 ± 0.4 MeV, which implies that there are lower and upper energy thresholds for contained muons. Muons with energy below 130 MeV experience the most energy loss due to ionization and thus stop in the OD without reaching the ID. On the other hand, muons with energy

Cut	Overall Ratio	Relative Ratio
$O\epsilon$	33.1%	44.0%
$OIO\epsilon$	42.2%	56.0%
$O\kappa$	1.1%	47.0%
$OI\kappa$	0.7%	31.8%
$OIO\kappa$	0.5%	21.2%
$O\delta O$	6.0%	27.0%
$O\delta OI$	1.4%	6.2%
$O\delta OIO$	1.0%	4.4%
$OI\delta I$	3.5%	15.5%
$OI\delta IO$	8.2%	36.8%
$OIO\delta O$	1.5%	6.5%
$OIO\delta OI$	0.5%	2.4%
$OIO\delta OIO$	0.3%	1.4%

Table 5.1: Geometry-based cuts, ratio of number of events in the cut to number of events, where a muon entered SMM (overall ratio); and ratio of number of events in the cut to number of events for cuts with the same Greek letter (relative ratio).

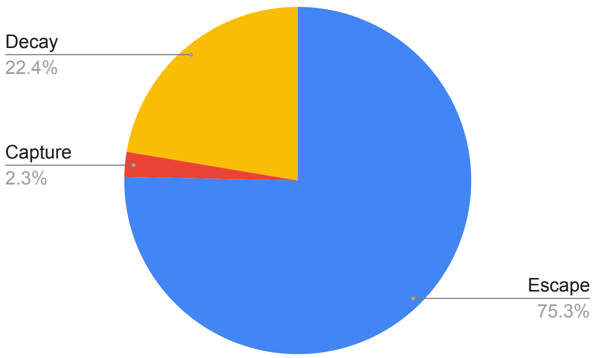

(a) Entered SMM

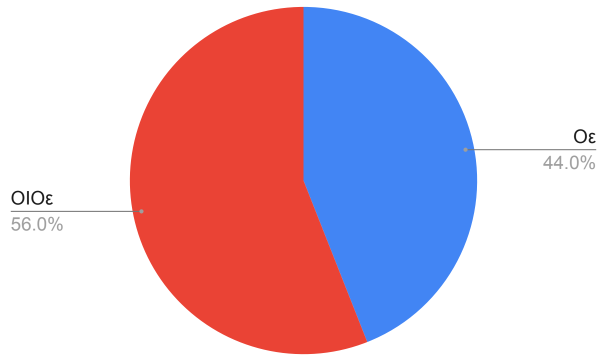

(b) Escaped Muon

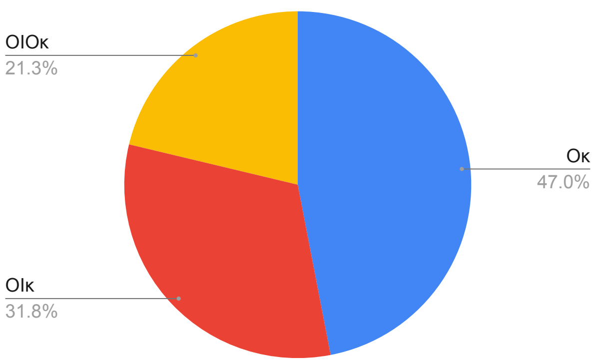

(c) Captured Muon

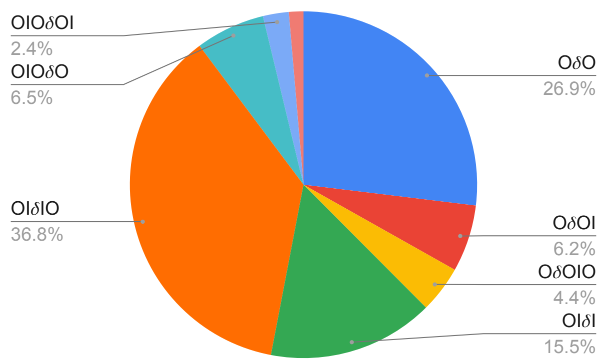

(d) Decayed Muon

Figure 5.5: Pie charts of ratios in Table 5.1 for muon fate (a), and relative ratios: muon escape (b), muon capture (c), muon decay (d). The relative ratio of $OIO\delta OIO$ (pink) in (d) is too small to label.

above 210 MeV have lower energy loss and do not lose enough momentum to stop in the ID.

The $OIO\delta$ distribution (Figure 5.6(d)) looks very similar to the contained distribution, while also being more spread-out with the mean signal higher than $OI\delta I$. This is to be expected as muons end up having more energy and thus entering the OD twice, therefore producing more signal.

In the $O\delta$ distribution (Figure 5.6(c)) the mean muon total energy is 126.8 ± 0.4 MeV, which indicates that muons that stopped in the SMM, but did not enter the ID are too low energy to do so, consistent with the 130 MeV threshold for contained events. Because muons only moved in the OD without entering the ID, scintillation light was collected continuously for the entire duration of muon travel in the SMM. This produces an approximately proportional relation between muon energy and light yield, as increasing travel length increases total energy loss and thus total scintillation light yield.

The $O\epsilon$ distribution (Figure 5.6(e)) looks similar to $O\delta$ in that many of the muons are below the 130 MeV threshold. Additionally, there are events with higher total energy above 130 MeV, which have signal uniformly distributed. This could be caused by muons being angled in such a way that they do not traverse much of the monitor and escape almost immediately. Therefore, energy loss can vary significantly from mean energy loss described by the Bethe formula. Because scintillation yield is proportional to energy loss, the signal varies significantly with total energy for events above 140 MeV.

The $OIO\epsilon$ distribution indicates that in order to traverse both the OD and the ID and then escape requires muons to have on average 220 MeV total energy, which is close to the upper bound in the $OI\delta I$ distribution. Therefore, muons above 210-220 MeV total energy are guaranteed to escape the SMM.

It is clear to see from Figure 5.6, that overall signal energy spectrum (Figure 5.6(a)) can be "deconstructed" into distinct event-geometry partitions of signal (Figure 5.6(b-f)). These partitions show how initial muon energy and event geometry can drastically affect whether or not the muon stopped and whether or not it entered the ID. Once data from the prototype will be collected, the positions of maxima of the PMT signal distribution in the OD from muons can be compared to

Figure 5.6(a). These maxima are directly related to contained and escaped events, and so give information about event geometry.

Next, I consider signal in the ID from muons arriving from the OD. The histograms for different partitions look very similar, so I will only look at the contained events, and at the overall dataset, which are plotted in Figure 5.7. For both plots, muons below the Cherenkov threshold at 120 MeV produce no signal as expected. In Figure 5.7(b) contained muons are now in the range of 120-180 MeV with mean energy of 146.7 ± 0.7 MeV similar to Figure 5.6(b). Therefore, contained muons lose on average 11.2 ± 1.1 MeV in the OD before they reach the ID.

5.3.3 Electron Signal

I will now consider Michel electron signal in the ID, since this is the signal used to count stopped muons. Plots of signal from electrons in the ID for all events and contained events and partitions can be found in Figure 5.8. In Figure 5.8(a), there does not seem to be any correlation between the signal in the ID and the energy of the electrons. This is similar to the $O\epsilon$ distribution for muons in Figure 5.6(e). Escaped electrons close to the edge of the OD do not travel much and therefore do not produce much signal in the ID. On the other hand, in Figure 5.8(b) there is a clear linear proportionality between signal and electron energy similar to Figure 5.6(c). This is due to electrons initially emerging in the ID and stopping in the ID. Therefore Cherenkov light is collected throughout the entire energy loss from initial energy to zero energy. Consequently, the signal in the ID is proportional to the initial energy of the Michel electron.

The mean signal in contained events is 1864 ± 9 photons, which is 1.5 times higher than the mean signal for all events at 1288 ± 3 photons. Moreover, the peak signal for contained events is not close to zero photons, unlike the peak for uncontained events. Therefore, contained events can be reliably used to count muons due to a distinct peak in signal with most contained events' signal close to that peak signal.

In order to test that escaped electrons in Figure 5.8(a) produce little signal is because of short travel time and to better understand how Michel electrons are distributed spatially in the ID,

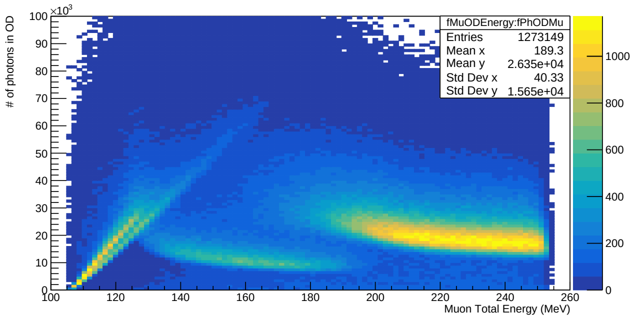

(a) Entered SMM

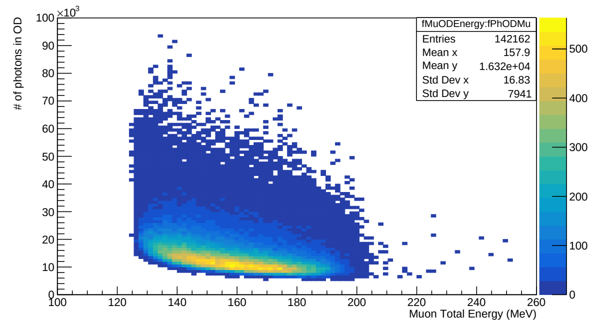

(b) $OI\delta$

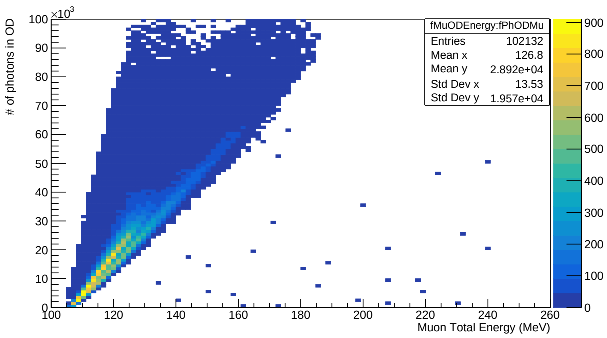

(c) $O\delta$

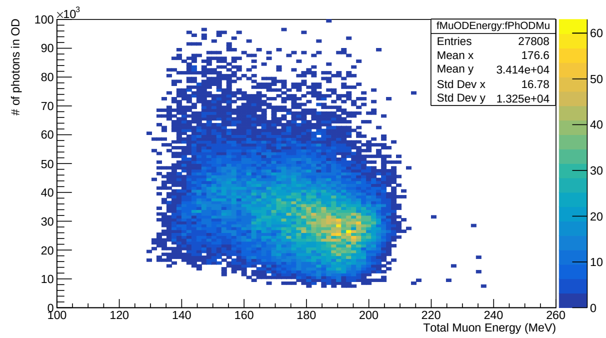

(d) $OIO\delta$

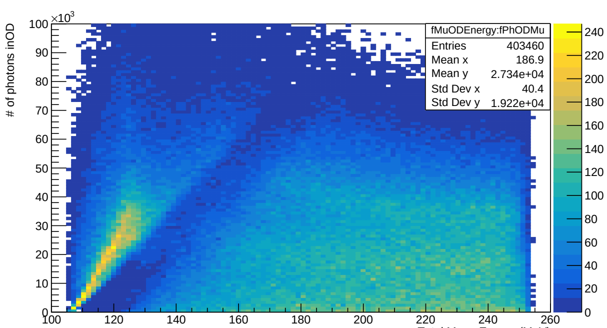

(e) $O\epsilon$

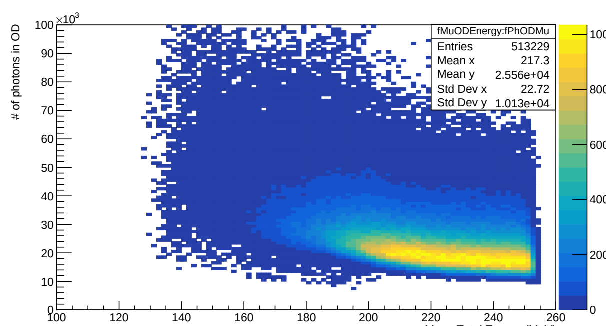

(f) $OIO\epsilon$

Figure 5.6: Muon signal in the OD versus total energy on entry for all muons that entered the SMM (a), $OI\delta$ cut (b), $O\delta$ cut (c), $OIO\delta$ cut (d), $O\epsilon$ cut (e), and $OIO\epsilon$ cut (f). Enlarged plots in Appendix.

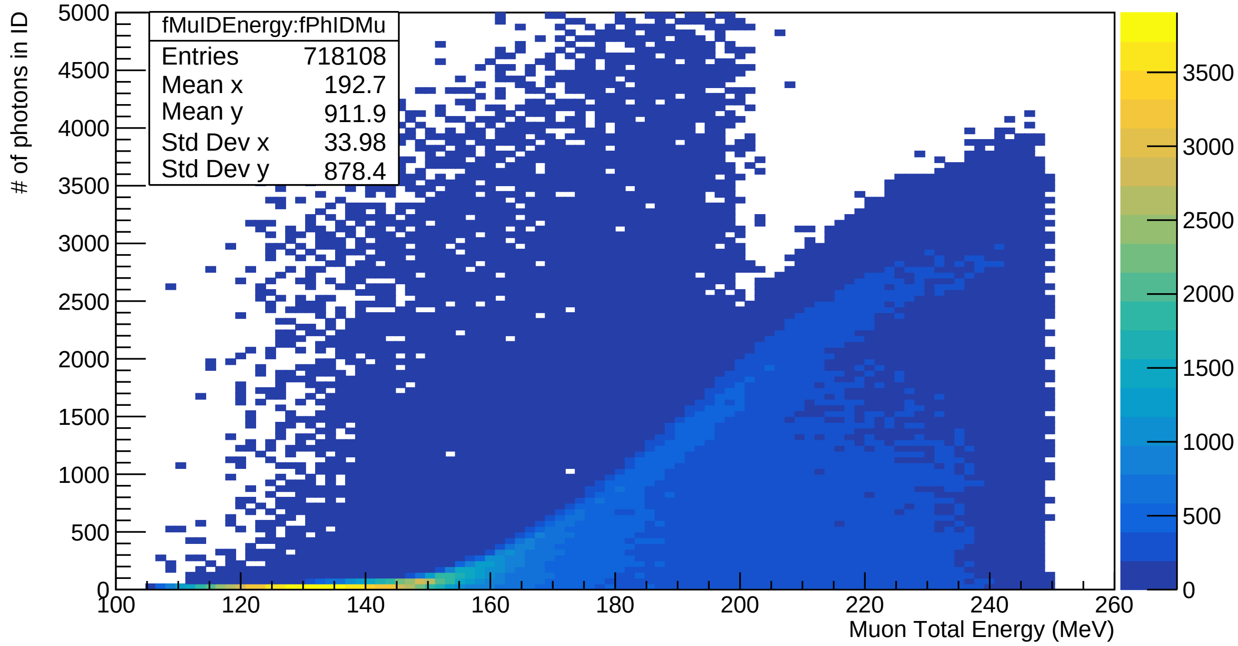

(a) Entered ID

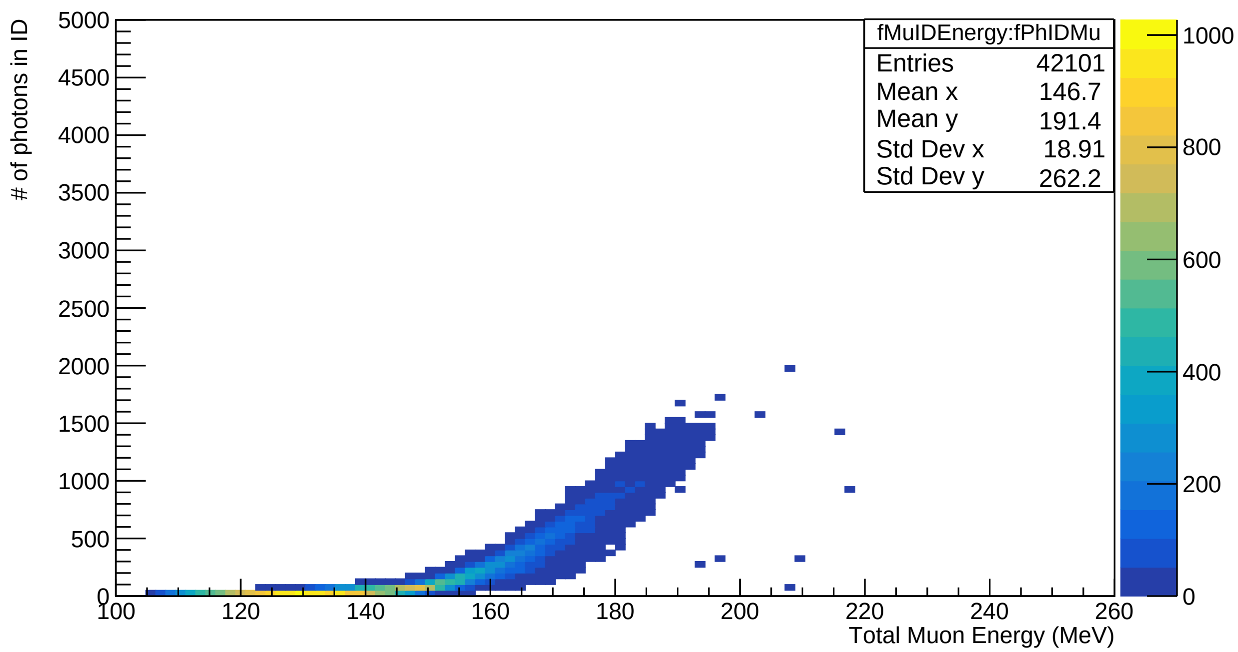

(b) $OI\delta I$

Figure 5.7: Muon signal in the ID versus total energy for muons entering OD (a) and only contained events (b).

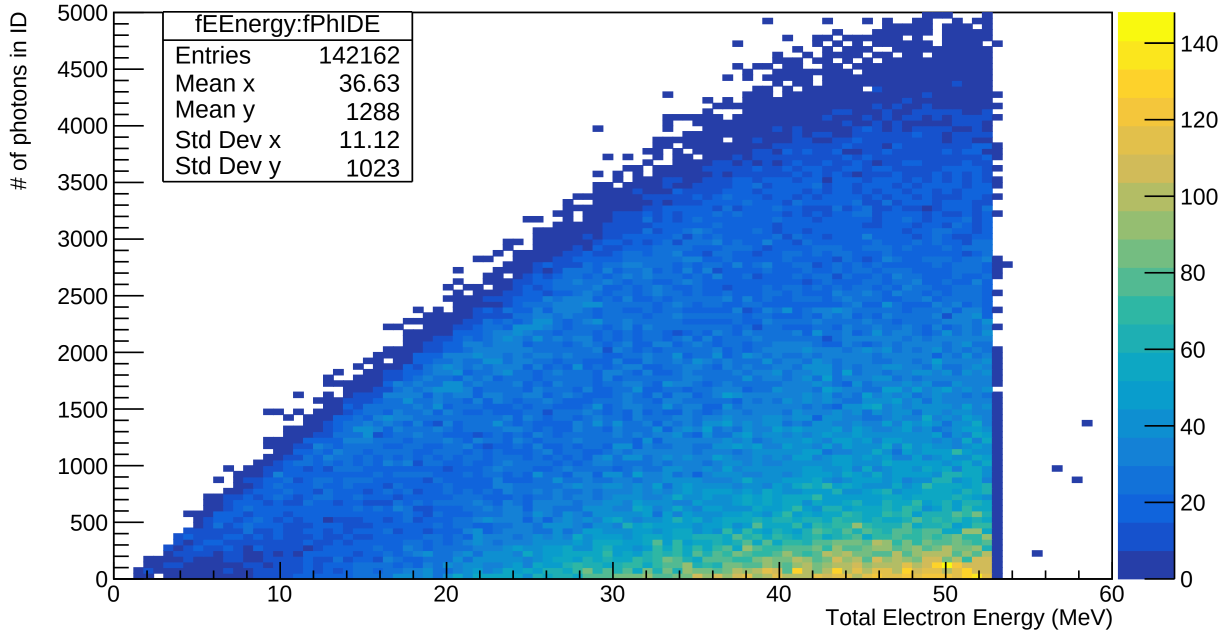

(a)

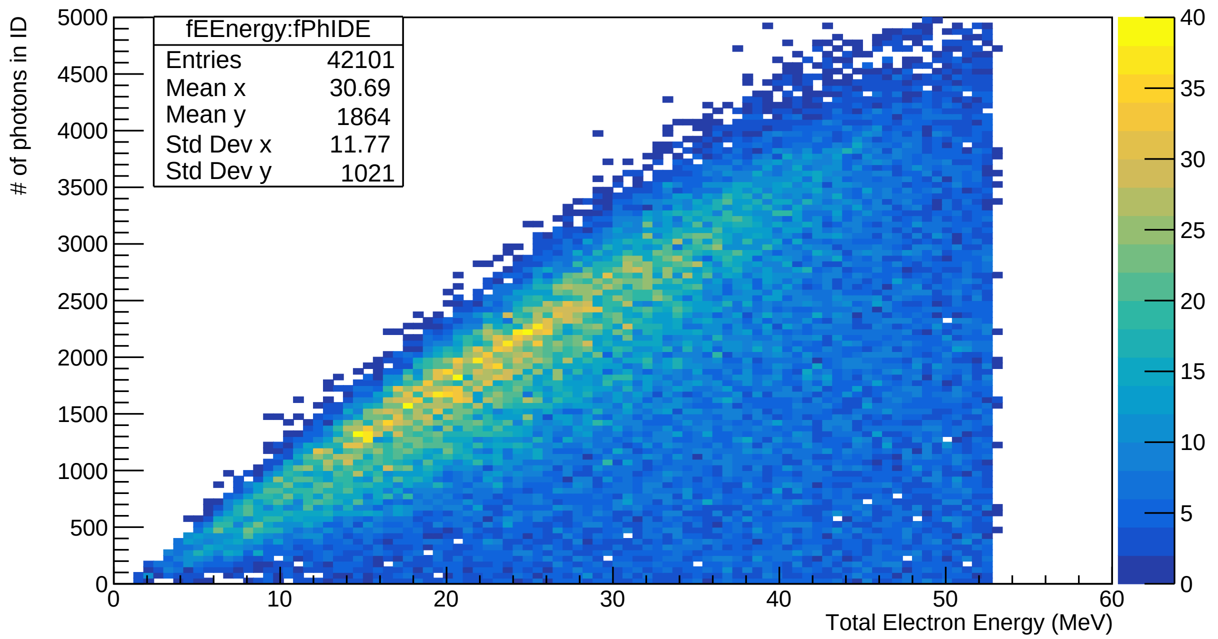

(b)

Figure 5.8: Electron signal in the ID versus electron total energy for any electron in ID (a) and only contained events (b).

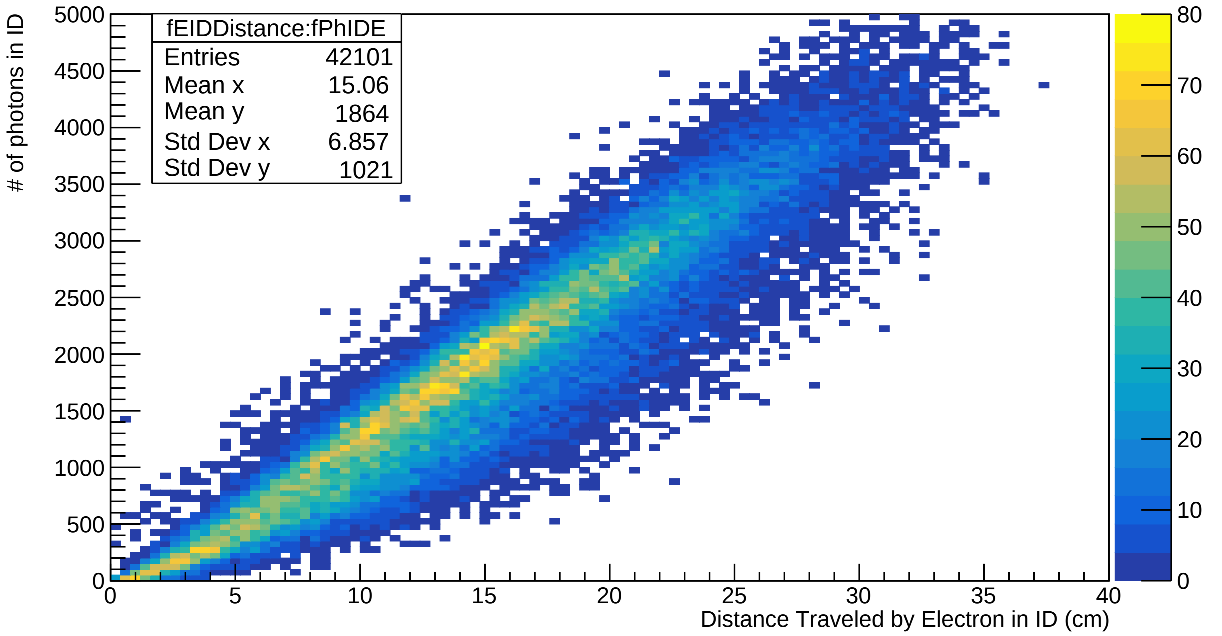

(a) $OI\delta I$

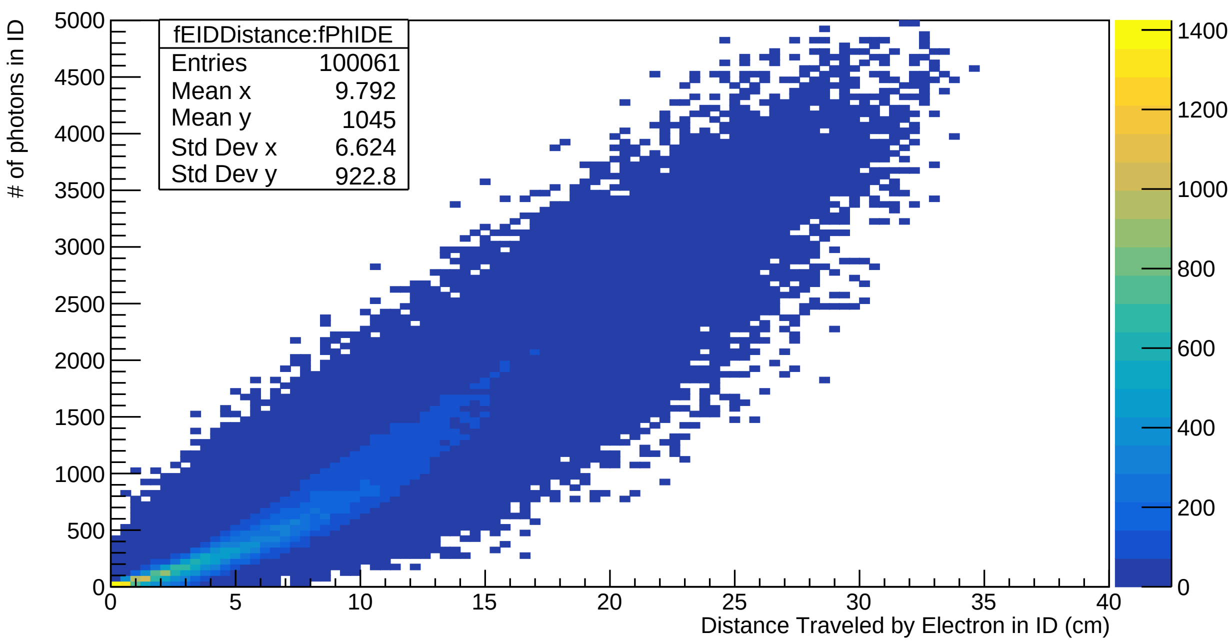

(b) $OI\delta IO$

Figure 5.9: Signal in the ID versus distance traveled in the ID by electrons for contained (a) and uncontained (b) events.

consider plots of signal versus distance for electrons in the ID in Figure 5.9. In both contained and uncontained events longer travel length in the ID results in more Cherenkov signal. In contained events (Figure 5.9(a)) electrons travel on average 15.06 ± 0.07 cm, close to the radius of ID. In uncontained events (Figure 5.9(b)) electrons only travel 9.79 ± 0.03 cm on average, with the distribution heavily skewed to close to 0 cm. This indicates that low light yields for uncontained events are due to Michel electrons being close to the edge of the ID and traveling outwards.

To further see the decay geometry in the ID, consider projections of initial electron position in the ID in Figure 5.10. Contained electrons (Figure 5.10 (a,c,e)) tend to be more clustered in the center of the ID, where they are evenly distributed in all directions. This gives them enough travel length to stop completely and avoid escape. On the other hand, uncontained electrons (Figure 5.10 (b,d,f)) are clustered at the top of the ID, decrease in number with decreasing z-position, and more spread out from the center in the xy-plane. For electrons closer at the top of the ID, electrons with positive z-momentum travel very little distance in the ID, which is consistent with Figure 5.9(b).

5.3.4 Quantum Efficiency Weights

As mentioned in Section 4.2, not all photons knock an electron off of a PMT photocathode. To account for that in the Monte Carlo, I weighted each photon's tally by quantum efficiency as function of photon wavelength using Figure 4.2. Ten lines equally were drawn between equally spaced points between 295 nm and 720 nm wavelength. The y-value of these lines was used to approximate quantum efficiency. The line fit parameters can be found in the Appendix.

Plots of weighted and unweighted signal in OD and ID can be found in Figure 5.11. After weighting data the magnitude of signal decreased by a factor of six. However, the shapes of signal distributions did not significantly change with quantum efficiency weights. Therefore, despite only detecting on average one out of six incident photons, PMTs can still recover information about muons and electrons in the SMM.

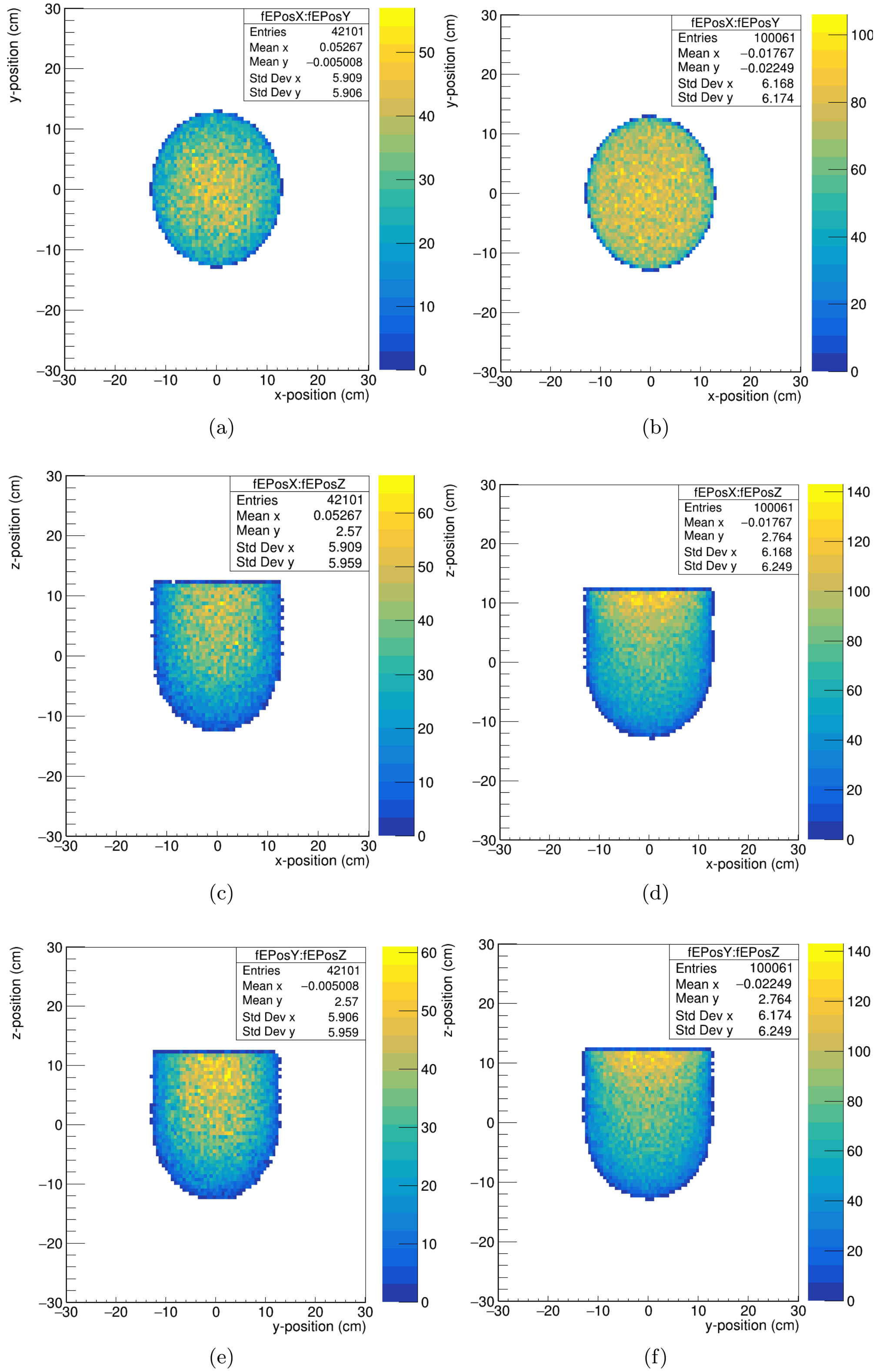

Figure 5.10: Projections of initial Michel electron position in the ID in the xy (a,b), xz (c,d), yz (e,f) planes for contained (a,c,e) and uncontained (b,d,f) electrons. Enlarged plots in Appendix.

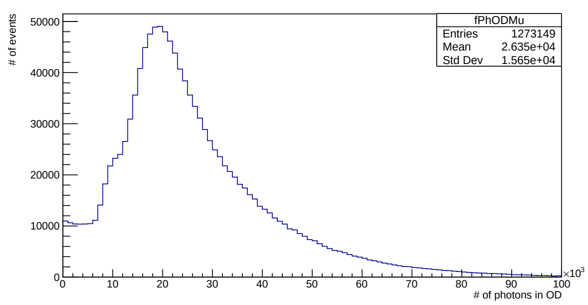

(a) unweighted

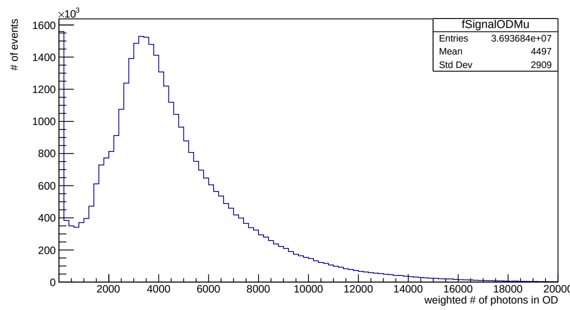

(b) weighted

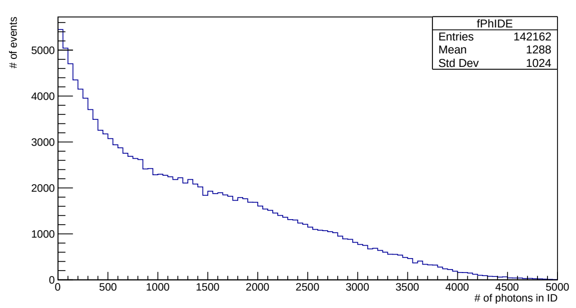

(c) unweighted

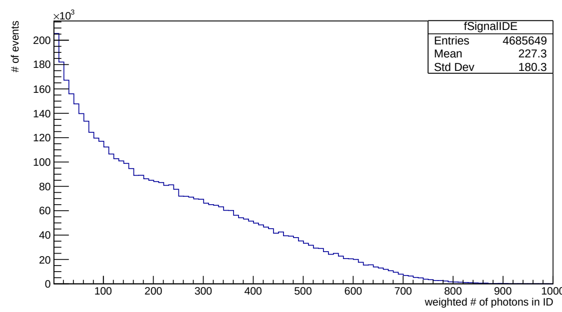

(d) weighted

Figure 5.11: Signal distribution for muons in OD (a,b) and electrons in ID (c,d) without quantum efficiency weights (a,c) and with weights (b,d). Enlarged plots in Appendix.

Chapter 6

Conclusion and Future Work

In this paper, I have discussed the background and the results of the Monte Carlo simulation of the DUNE Stopped Muon Monitor prototype at University of Colorado Boulder. The Stopped Muon Monitor will be used in the DUNE experiment to measure muon flux from neutrino beam generation, which will then constrain neutrino flux due to known hadron decay kinematics. The initial test of the SMM prototype is being conducted at the University of Colorado Boulder, where cosmic ray muons are used to collect detector data. The Monte Carlo simulation in this paper simulates the SMM prototype geometry when exposed to cosmic ray muon flux.

The Monte Carlo results were interpreted to better understand the geometry of cosmic ray muon and Michel electron distributions. It was found that the SMM is not sensitive to the zenith angle distribution of muon flux due to SMM's round shape. 75.3% of cosmic ray muons with 0-150 MeV kinetic energy do not stop in the detector and escape. 52.3% of decays occur in the ID. Only 29.4% of Michel electrons that emerged in the ID did not escape the ID. Therefore, 3.5% of events in the SMM are contained in this muon energy range. Although this is a small amount of flux in the DUNE beamline, the SMM is sensitive enough to detect singular muon decays. Therefore, even if a small number of muons stop in the SMM, it will be able to detect them.

Of the stopped muons, the muon capture rate was found to be $(30.9 \pm 0.2)\%$ for μ^-, which is significantly higher than the predicted rate of $(8.0 \pm 0.9)\%$. This increase could be caused by additional capture in steel shell separating the ID from the OD, where muon capture rate is about $(90.8 \pm 0.2)\%$. Additionally, some muons that were meant to escape could have been captured, increasing the overall capture rate.

Scintillation light from muons in the OD was found to have an energy spectrum with distinct regions that depend on event geometry. In particular, it was found that every contained event is bounded to 130-210 MeV of initial total muon energy before entering the SMM. The mean energy of contained events was found to be 157.9 ± 0.4 MeV. These contained muons lose on average 11.2 ± 1.1 MeV of energy in the OD before entering the ID. Additionally, muons above 210 MeV total energy are too high energy to stop and are guaranteed to escape. Both the contained and escaped muons produce characteristic peaks for signal in the OD. The signal distribution in the OD can be measured in an experiment to compare with Monte Carlo and apply corrections.

Michel electrons in the ID were found to have different signal spectra and event geometries for contained and uncontained events. In particular, contained events are uniformly clustered in the ID center, while uncontained events tend to cluster at the top of the ID. Contained electrons travel on average 15.06 ± 0.07 cm in the ID, while uncontained electrons only travel 9.79 ± 0.03 cm on average with heavy skew towards smaller distances. Moreover, contained events produce Cherenkov light yield proportional to the electron's initial energy. This produces a signal with a mean of 1864 ± 9 photons and a distinct peak in signal with most events spread around that peak. Consequently, contained muon decays in the ID can be reliably counted.

In the future, data collected from the prototype at CU will be used to make corrections to the Monte Carlo discussed in this paper. Once enough corrections will have been made to match the data, the Monte Carlo SMM geometry will be used to simulate the SMM in the NuMI and DUNE beamlines.

Bibliography

[1] D. Griffiths, Introduction to elementary particles. 2008.

[2] W. Haxton, R. Hamish Robertson, and A. M. Serenelli, "Solar neutrinos: Status and prospects," Annual Review of Astronomy and Astrophysics, vol. 51, p. 2161, Aug 2013.

[3] M. Tanabashi et al., "Review of Particle Physics," Phys. Rev., vol. D98, no. 3, p. 030001, 2018.

[4] S. F. King and C. Luhn, "Neutrino Mass and Mixing with Discrete Symmetry," Rept. Prog. Phys., vol. 76, p. 056201, 2013.

[5] M. Scott, "Latest oscillation results from T2K," J. Phys. Conf. Ser., vol. 1342, no. 1, p. 012043, 2020.

[6] R. Acciarri et al., "Long-Baseline Neutrino Facility (LBNF) and Deep Underground Neutrino Experiment (DUNE), Volume 2: The Physics Program for DUNE at LBNF," 2015.

[7] R. Acciarri et al., "Long-Baseline Neutrino Facility (LBNF) and Deep Underground Neutrino Experiment (DUNE), Volume 1: The LBNF and DUNE Projects," 2016.

[8] R. Acciarri et al., "Long-Baseline Neutrino Facility (LBNF) and Deep Underground Neutrino Experiment (DUNE), Volume 4: The DUNE Detectors at LBNF," 2016.

[9] M. Bass et al., "Baseline Optimization for the Measurement of CP Violation, Mass Hierarchy, and θ_{23} Octant in a Long-Baseline Neutrino Oscillation Experiment," Phys. Rev., vol. D91, no. 5, p. 052015, 2015.

[10] I. Esteban, M. C. Gonzalez-Garcia, A. Hernandez-Cabezudo, M. Maltoni, and T. Schwetz, "Global analysis of three-flavour neutrino oscillations: synergies and tensions in the determination of θ_{23}, δ_{CP}, and the mass ordering," JHEP, vol. 01, p. 106, 2019.

[11] C. Andreopoulos, C. Barry, S. Dytman, H. Gallagher, T. Golan, R. Hatcher, G. Perdue, and J. Yarba, "The genie neutrino monte carlo generator: Physics and user manual," 2015.

[12] N. Palanque-Delabrouille, C. Yche, J. Baur, C. Magneville, G. Rossi, J. Lesgourgues, A. Borde, E. Burtin, J.-M. LeGoff, J. Rich, and et al., "Neutrino masses and cosmology with lyman-alpha forest power spectrum," Journal of Cosmology and Astroparticle Physics, vol. 2015, p. 011011, Nov 2015.

[13] M. Drewes, "The phenomenology of right handed neutrinos," International Journal of Modern Physics E, vol. 22, p. 1330019, Aug 2013.

[14] J. P. Pinheiro and C. A. d. S. Pires, "Vacuum stability and spontaneous violation of the lepton number at low energy scale in a model for light sterile neutrinos," 2020.

[15] B. Abi et al., "The DUNE Far Detector Interim Design Report Volume 1: Physics, Technology and Strategies," 2018.

[16] J. Strait et al., "Long-Baseline Neutrino Facility (LBNF) and Deep Underground Neutrino Experiment (DUNE), Volume 3: Long-Baseline Neutrino Facility for DUNE," 2016.

[17] T. Nakaya and R. K. Plunkett, "Neutrino oscillations with the MINOS, MINOS+, t2k, and NOvA experiments," New Journal of Physics, vol. 18, p. 015009, jan 2016.

[18] K. Duffy, "High-Pressure Gaseous Argon TPC for the DUNE Near Detector," in Meeting of the Division of Particles and Fields of the American Physical Society (DPF2019) Boston, Massac 2019.

[19] B. Abi et al., "The DUNE Far Detector Interim Design Report, Volume 2: Single-Phase Module," 2018.

[20] Hamamatsu, Photomultiplier Tubes and Related Products.

[21] S. Cecchini and M. Spurio, "Atmospheric muons: experimental aspects," 2012.

[22] S. Burdin, M. Horbatsch, and W. Taylor, "A correction to birks' law in liquid argon ionization chamber simulations for highly ionizing particles," Nuclear Instruments and Methods in Physics Research Section A: Accelerators, Spectrometers, Detectors and Associated Equipment, vol. 664, no. 1, pp. 111 – 116, 2012.

[23] T. Suzuki, D. F. Measday, and J. P. Roalsvig, "Total nuclear capture rates for negative muons," Phys. Rev. C, vol. 35, pp. 2212–2224, Jun 1987.

[24] Geant4 user's guide for application developers.

[25] ROOT data analysis framework user's guide.

Appendix A

Line #	wavelength range (nm)	slope (nm^{-1})	y-intercept
1	295-337.5	0.4	-117
2	337.5-380	0.235	-61.41
3	380-422.5	0.0235	19.06
4	422.5-465	-0.188	108.53
5	465-507.5	-0.188	108.53
6	507.5-550	-0.0941	60.76
7	550-592.5	-0.134	82.76
8	592.5-635	-0.0565	36.76
9	635-677.5	-0.0191	13
10	677.5-720	-0.00188	1.37

Table A.1: Figure 4.2 fit parameters

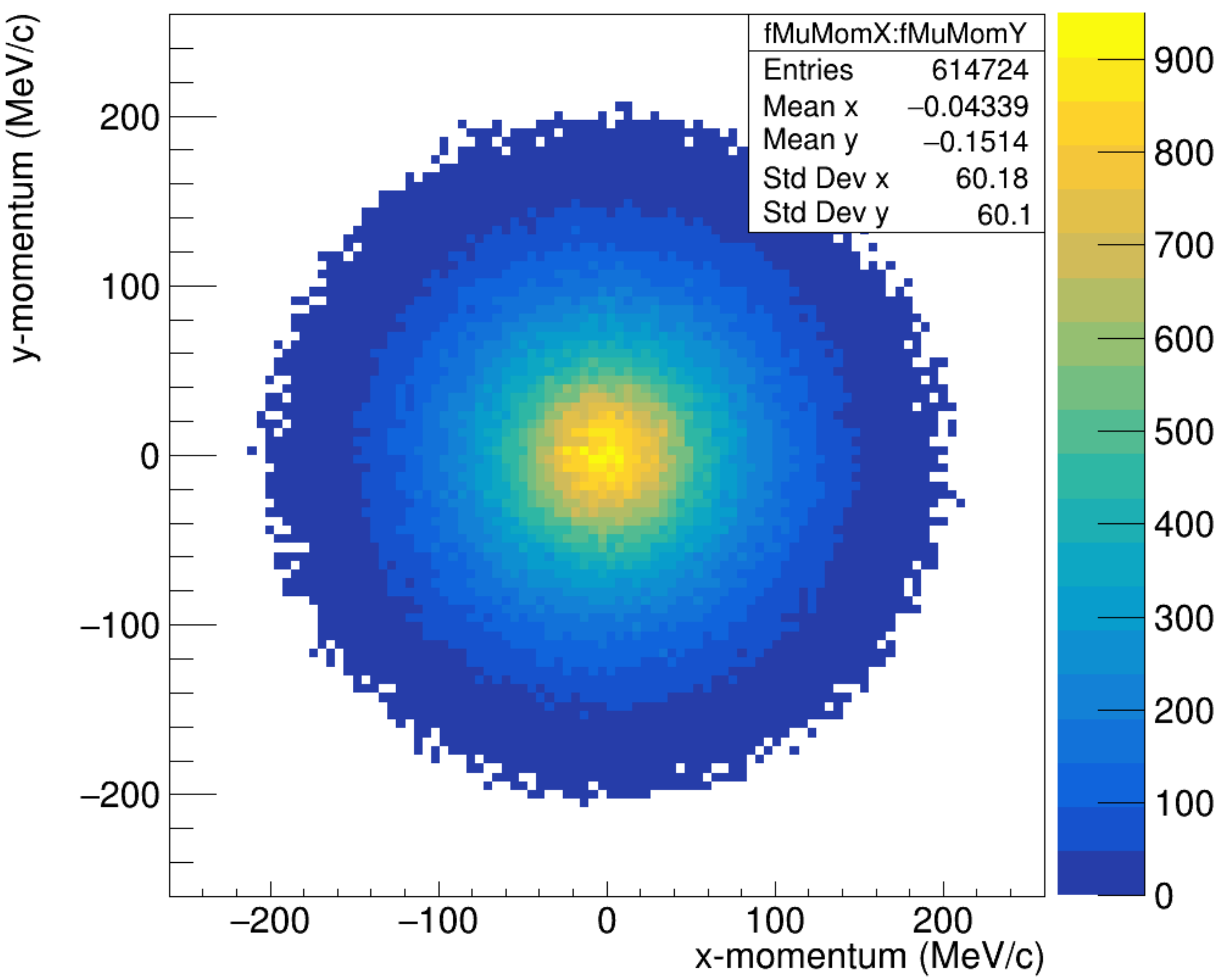

fMuMomX:fMuMomY
Entries 614724
Mean x −0.04339
Mean y −0.1514
Std Dev x 60.18
Std Dev y 60.1
y-momentum (MeV/c)
x-momentum (MeV/c)

Figure 5.2(a)

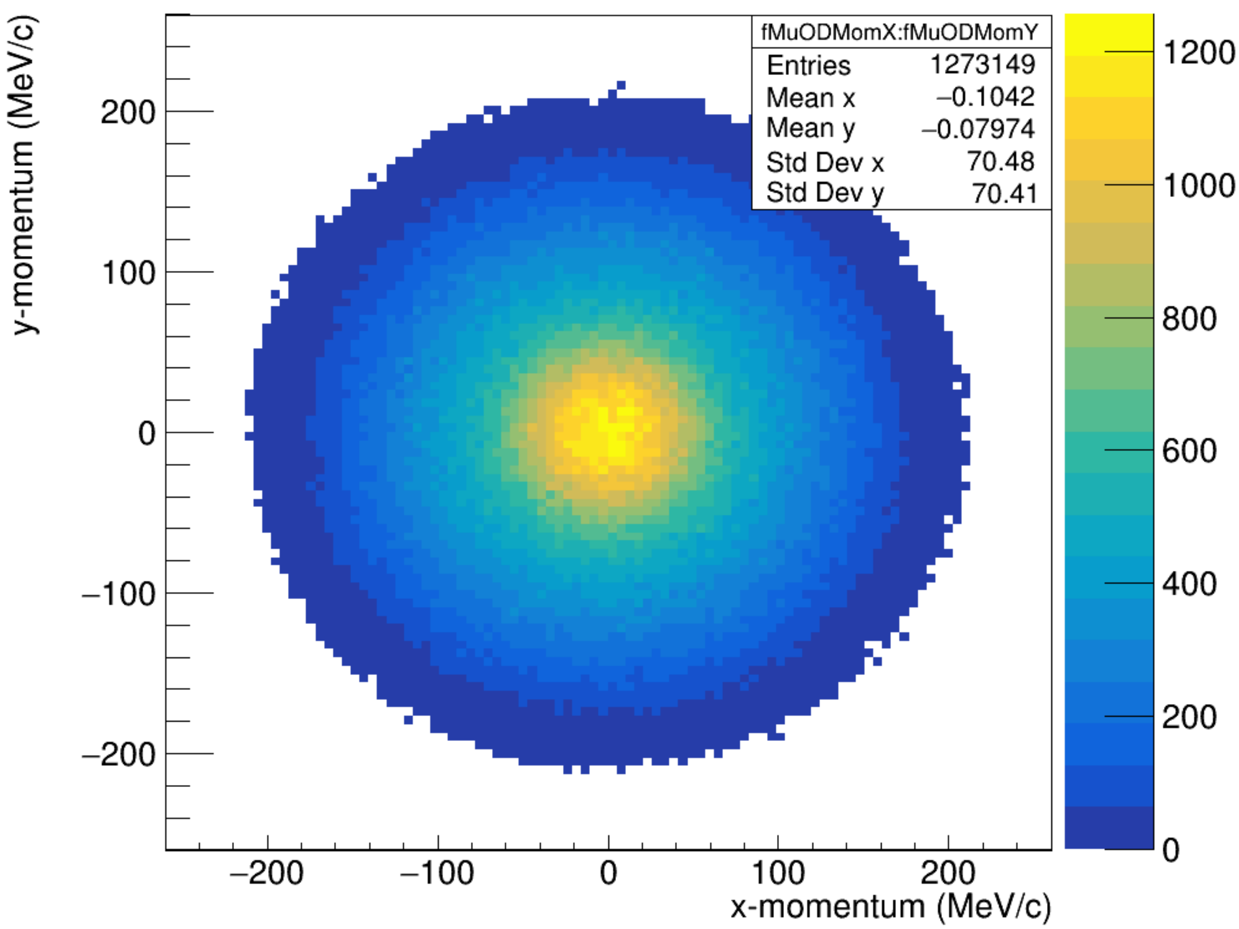
fMuODMomX:fMuODMomY
Entries 1273149
Mean x −0.1042
Mean y −0.07974
Std Dev x 70.48
Std Dev y 70.41
y-momentum (MeV/c)
x-momentum (MeV/c)
200
100
0
−100
−200
1200
1000
800
600
400
200
0

Figure 5.2(b)

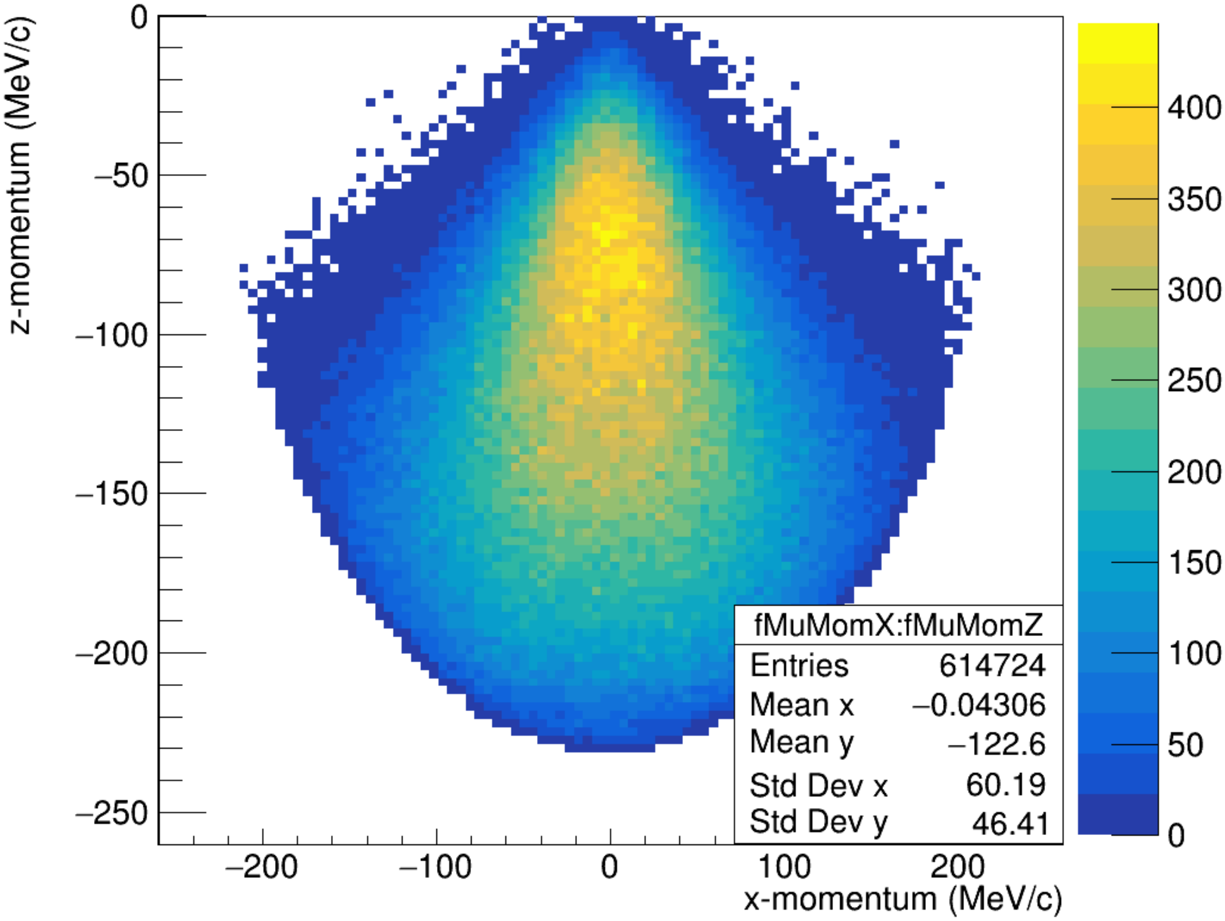
z-momentum (MeV/c)
x-momentum (MeV/c)
0
−50
−100
−150
−200
−250
−200
−100
0
100
200
400
350
300
250
200
150
100
50
0
fMuMomX:fMuMomZ
Entries 614724
Mean x −0.04306
Mean y −122.6
Std Dev x 60.19
Std Dev y 46.41

Figure 5.2(c)

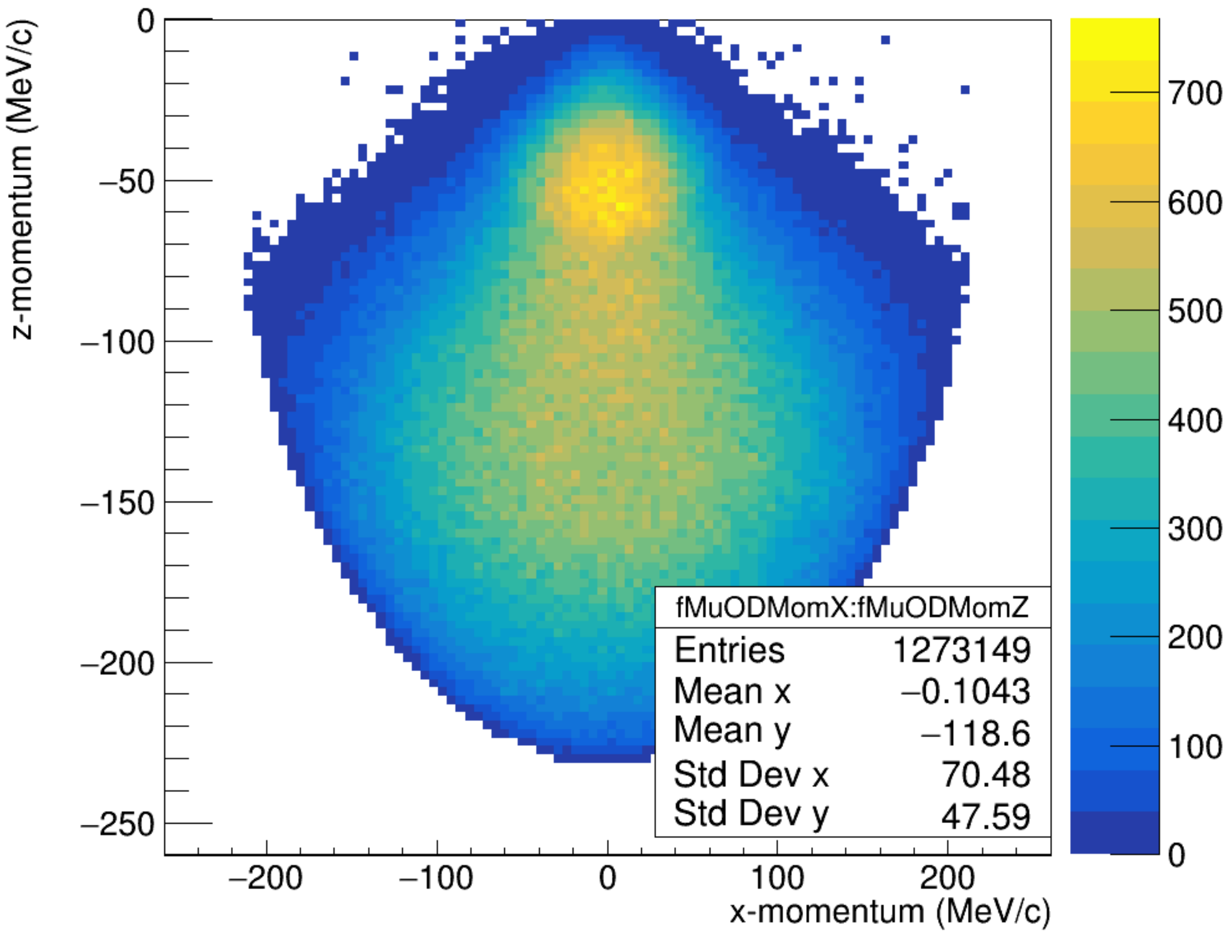

z-momentum (MeV/c)
0
−50
−100
−150
−200
−250
−200
−100
0
100
200
x-momentum (MeV/c)
700
600
500
400
300
200
100
0
fMuODMomX:fMuODMomZ
Entries 1273149
Mean x −0.1043
Mean y −118.6
Std Dev x 70.48
Std Dev y 47.59

Figure 5.2(d)

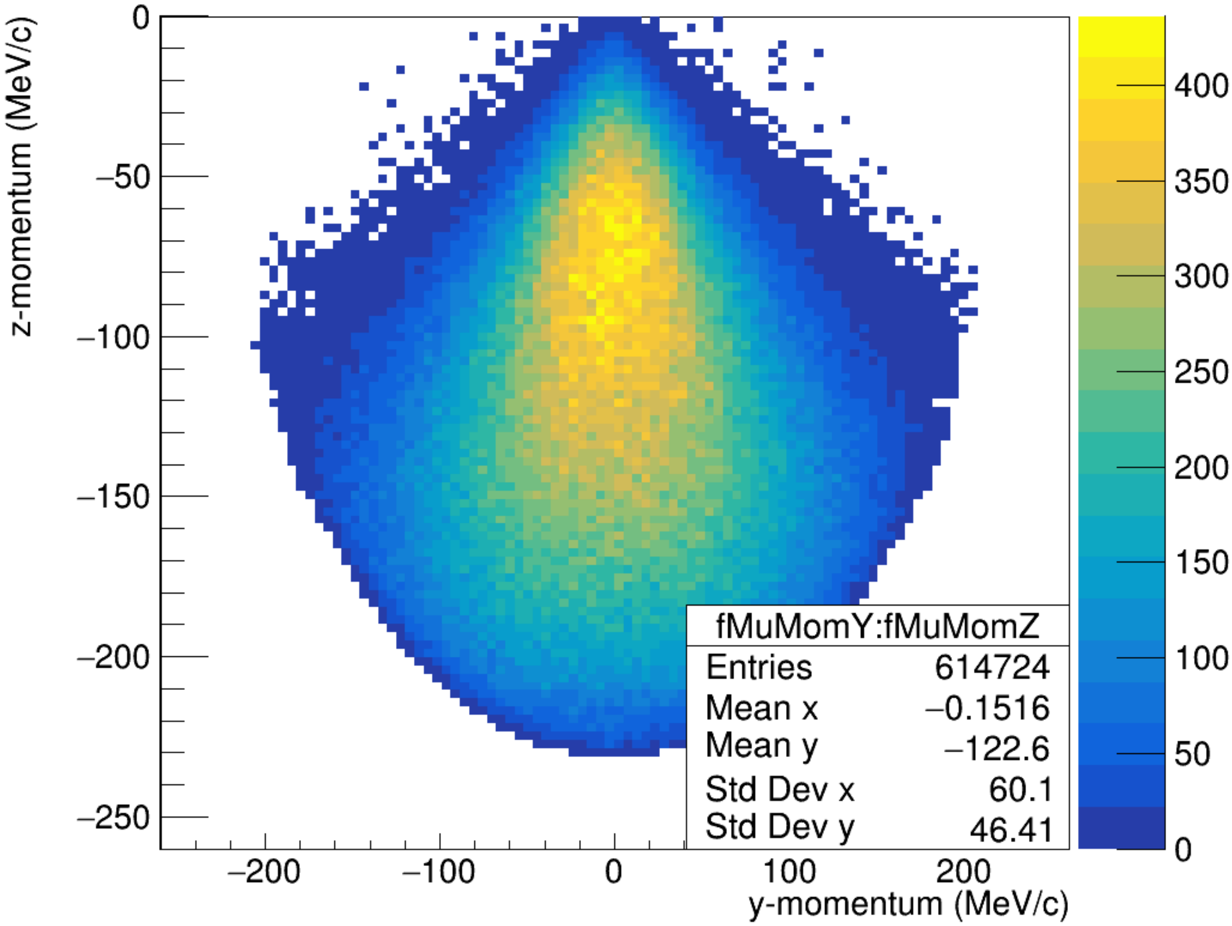

z-momentum (MeV/c)
0
−50
−100
−150
−200
−250
−200
−100
0
100
200
y-momentum (MeV/c)
400
350
300
250
200
150
100
50
0
fMuMomY:fMuMomZ
Entries 614724
Mean x −0.1516
Mean y −122.6
Std Dev x 60.1
Std Dev y 46.41

Figure 5.2(e)

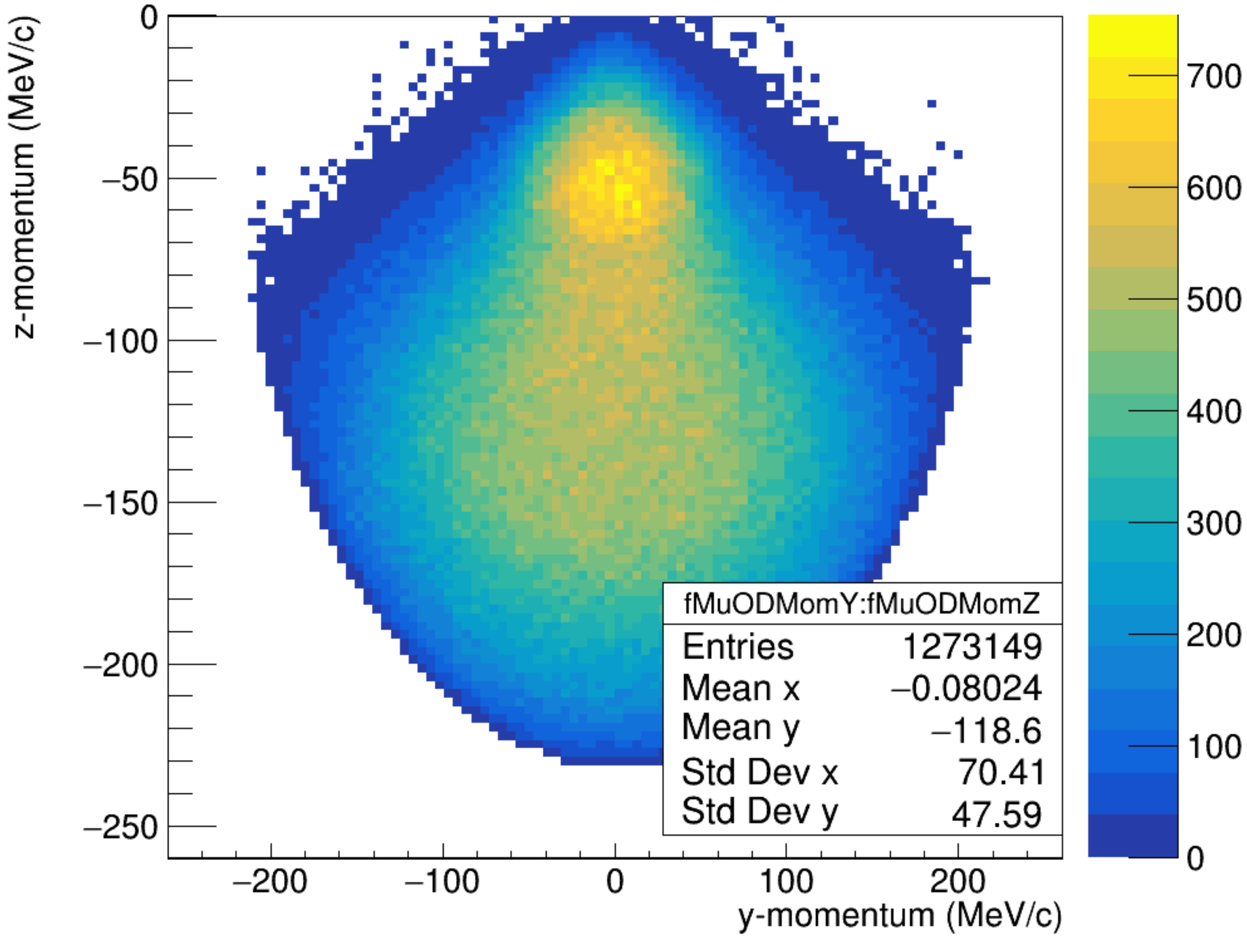

Figure 5.2(f)

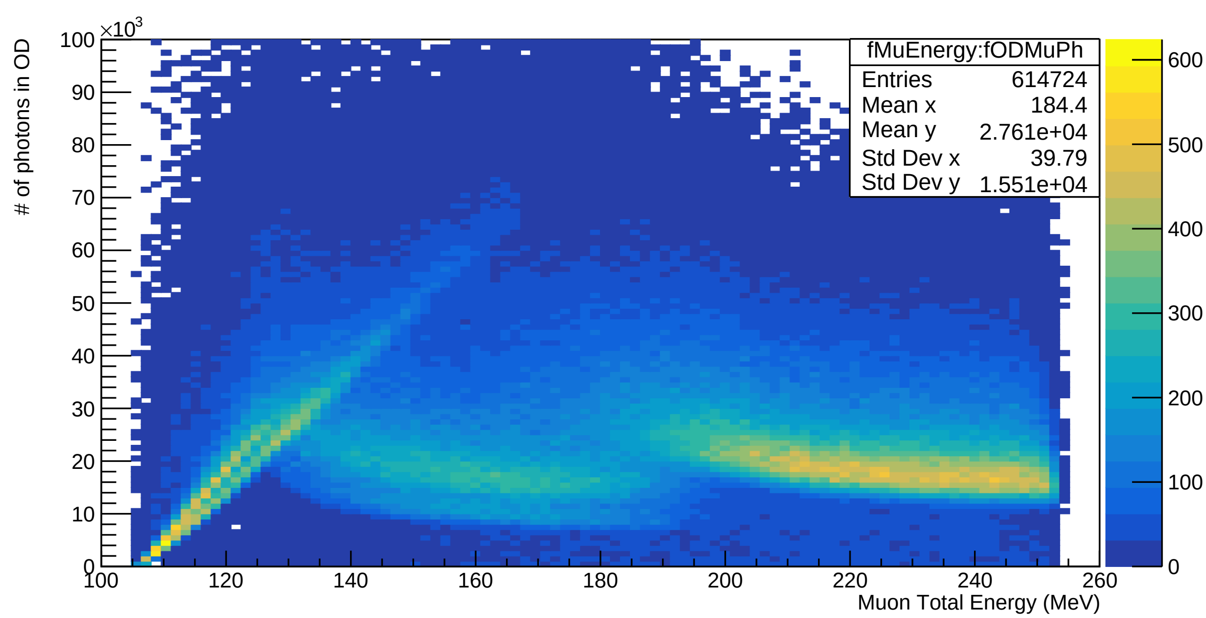

Figure 5.3(a)

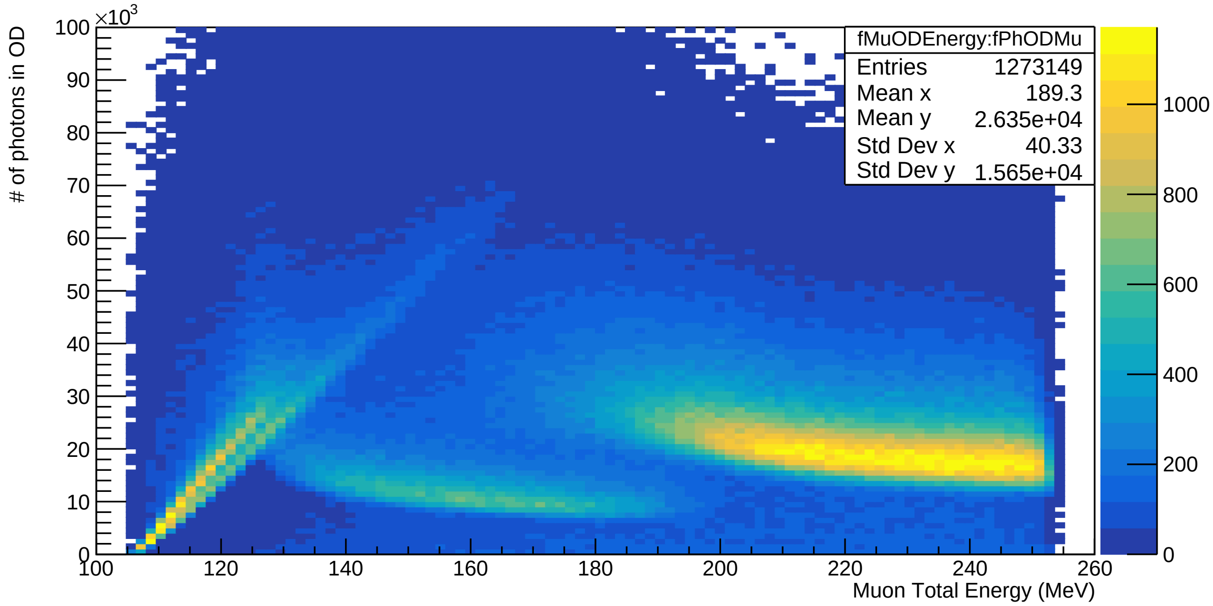

Figure 5.3(b)

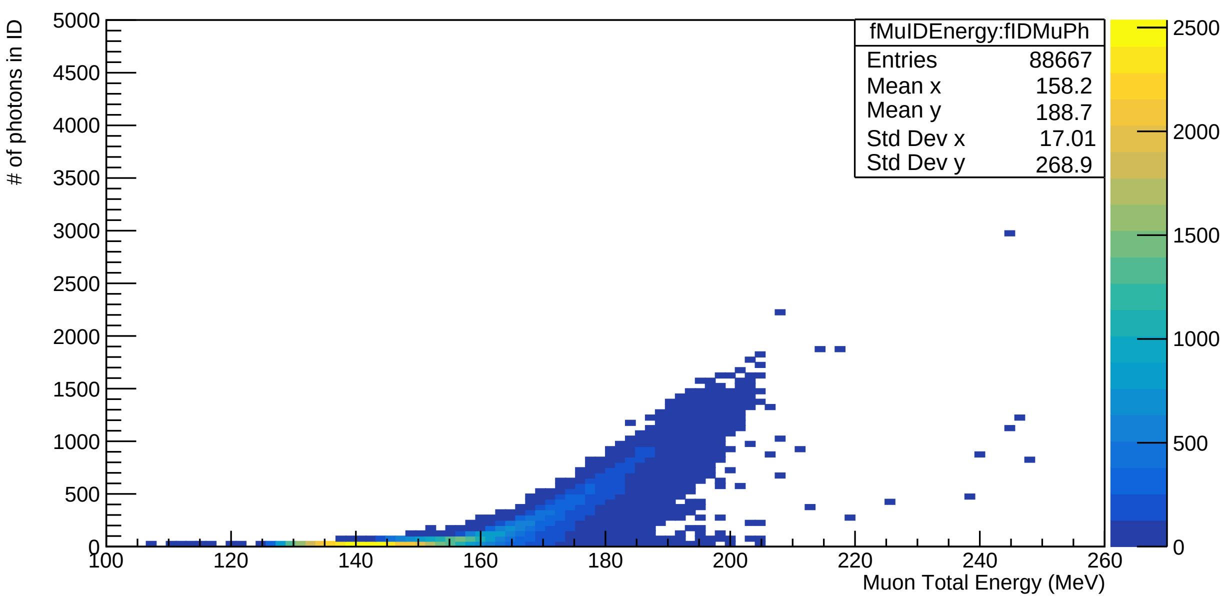

Figure 5.3(c)

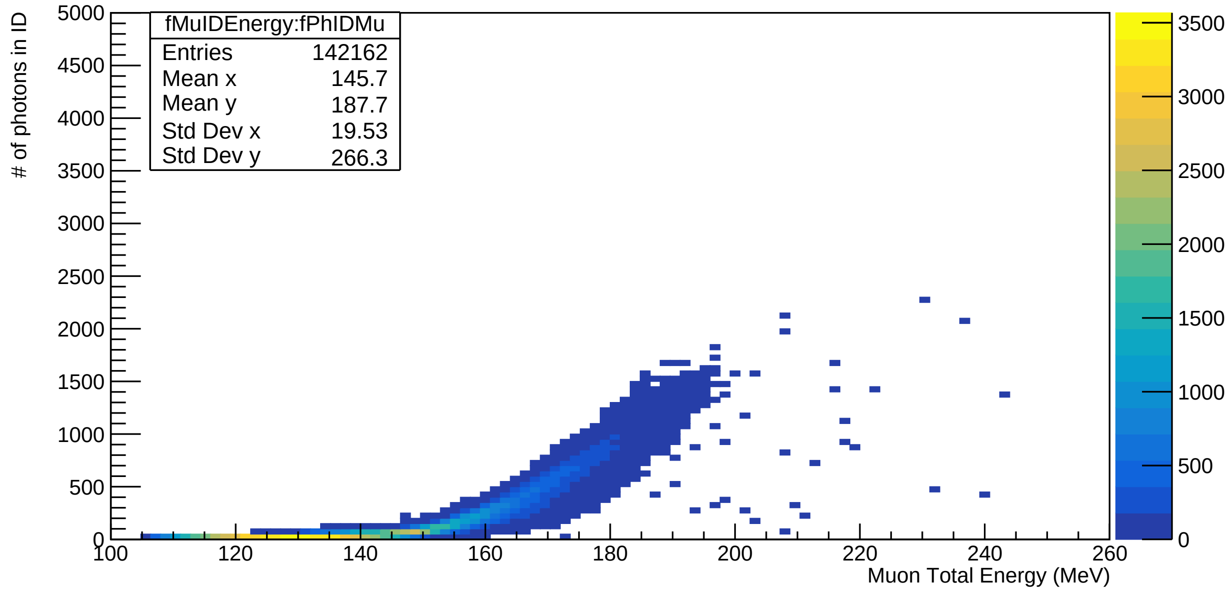

Figure 5.3(d)

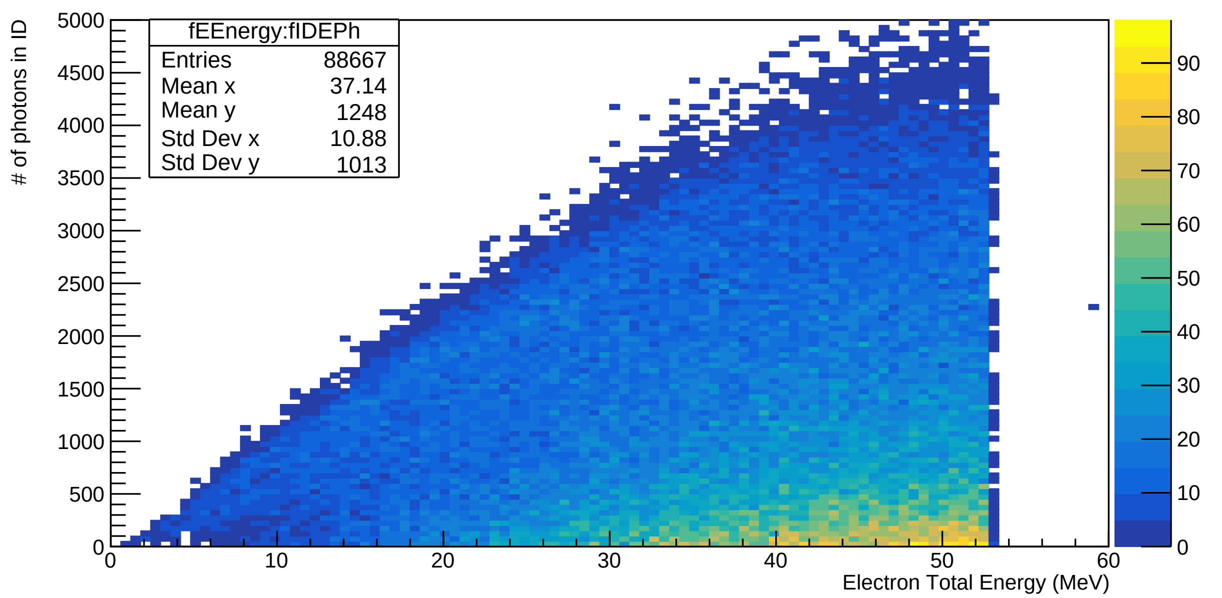

Figure 5.3(e)

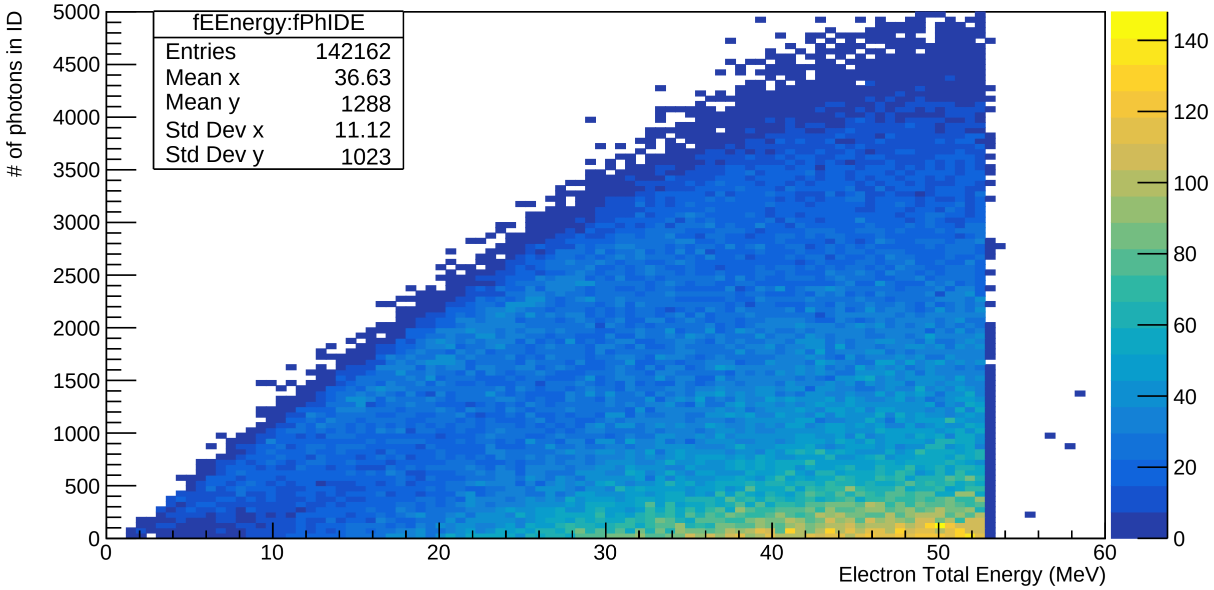

Figure 5.3(f)

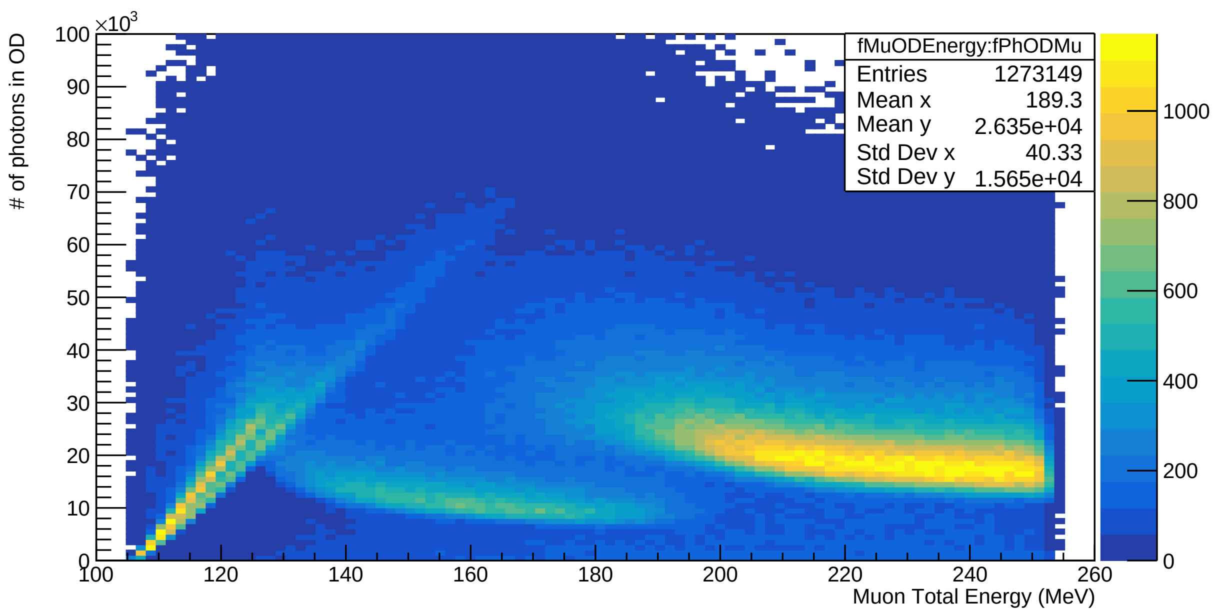

Figure 5.6(a)

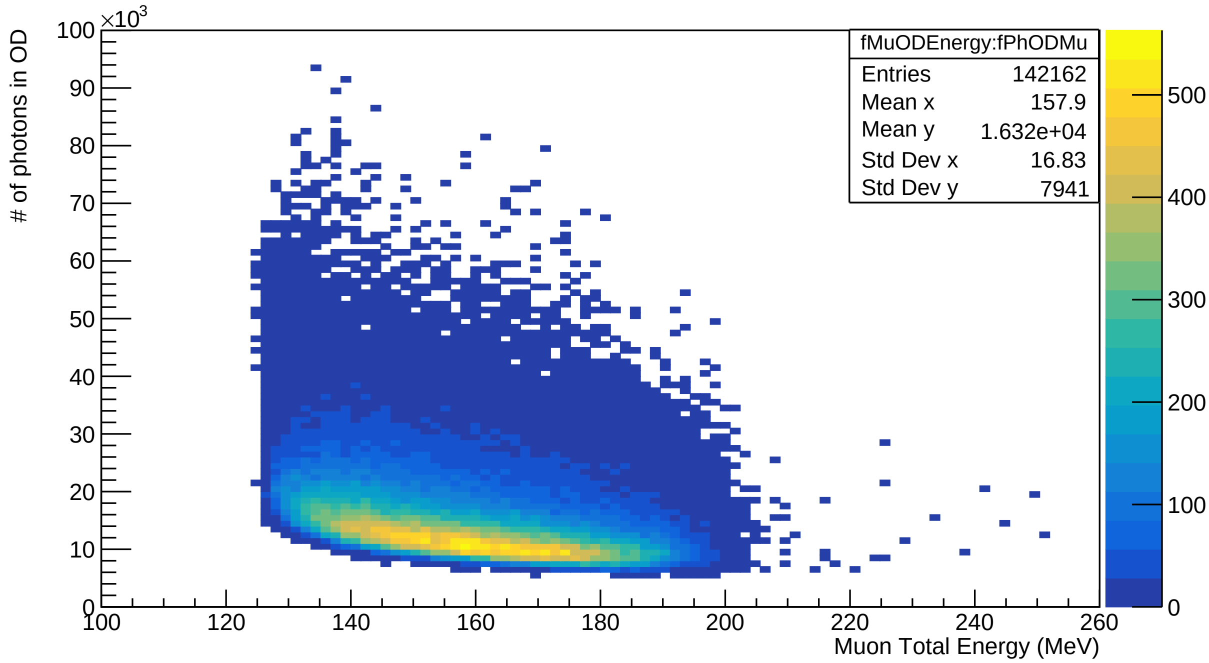

Figure 5.6(b)

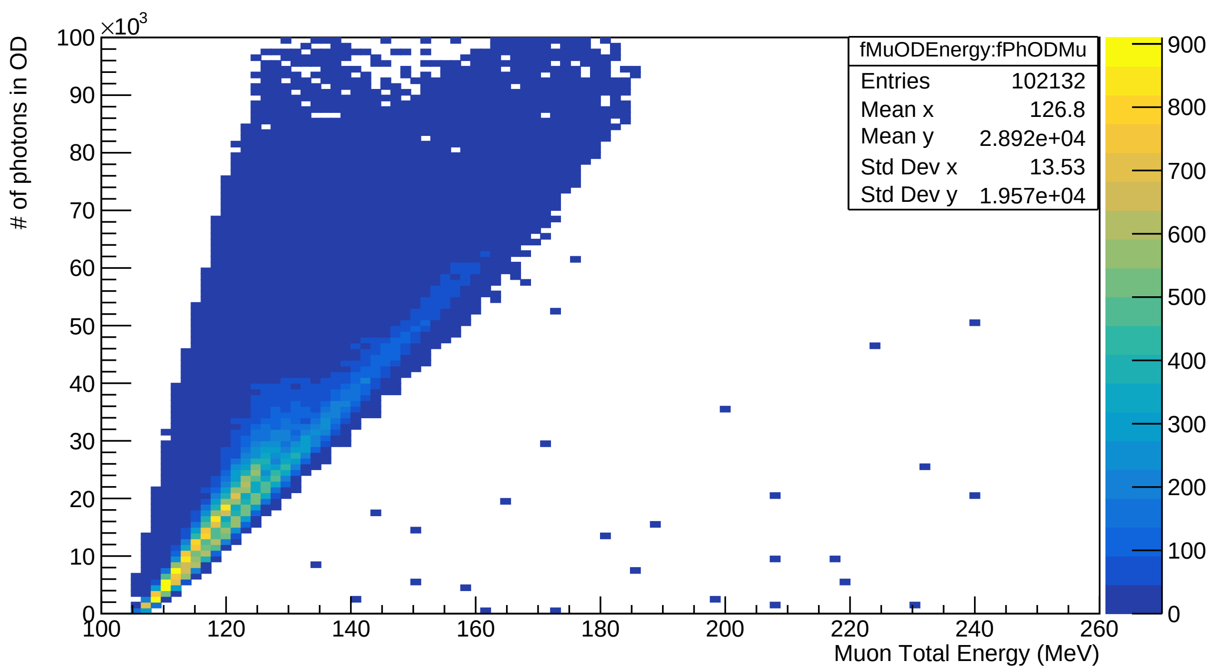

Figure 5.6(c)

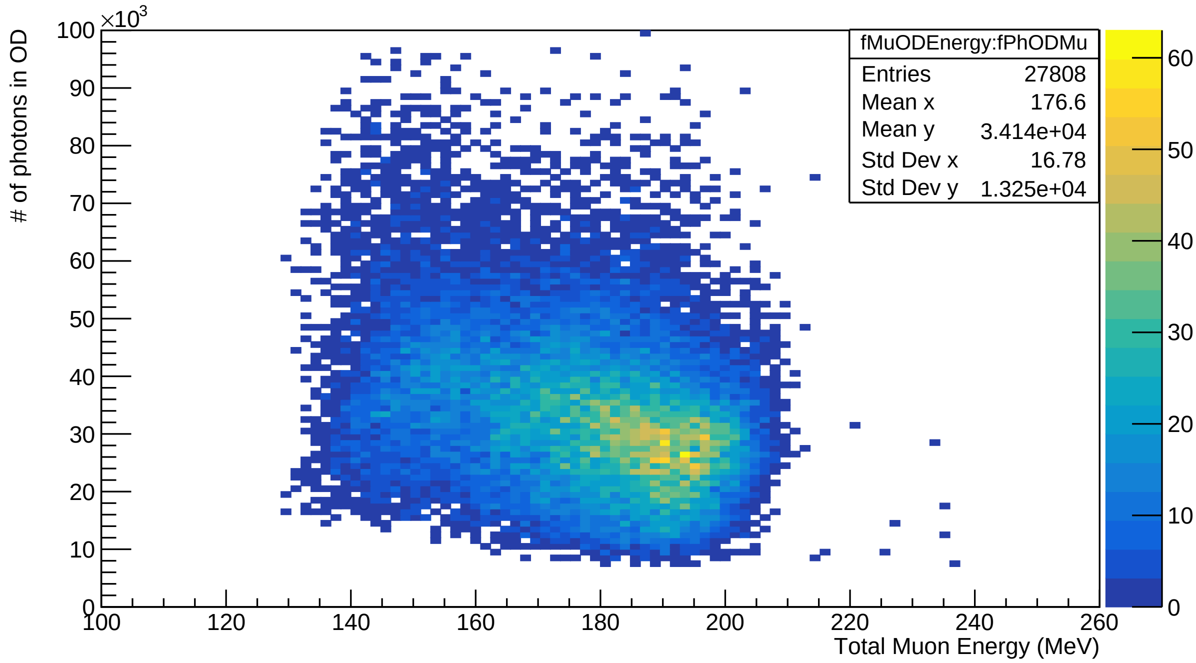

Figure 5.6(d)

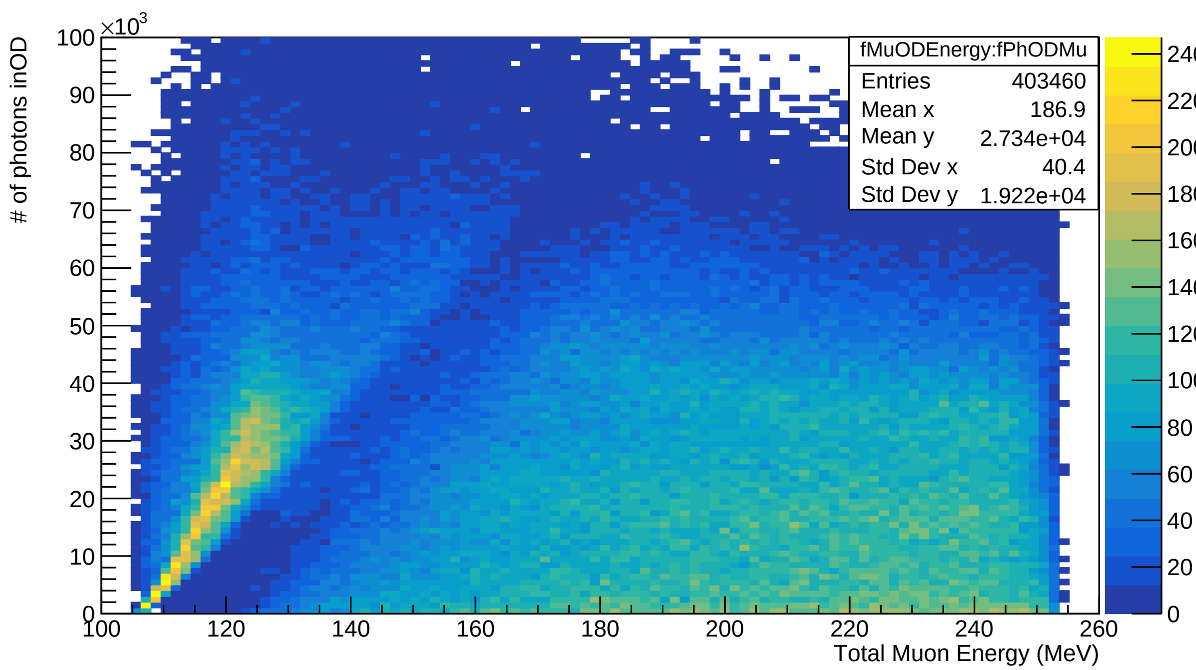

Figure 5.6(e)

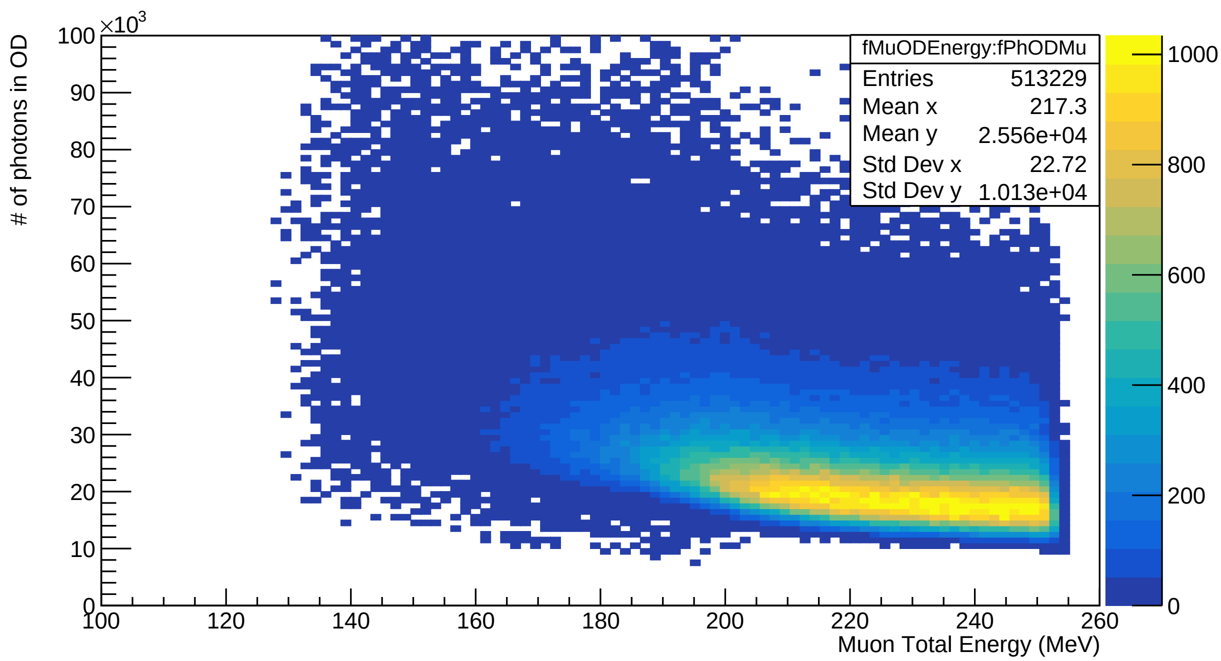
fMuODEnergy:fPhODMu
Entries 513229
Mean x 217.3
Mean y 2.556e+04
Std Dev x 22.72
Std Dev y 1.013e+04
# of photons in OD
×10^3
100
90
80
70
60
50
40
30
20
10
0
100
120
140
160
180
200
220
240
260
Muon Total Energy (MeV)
1000
800
600
400
200
0

Figure 5.6(f)

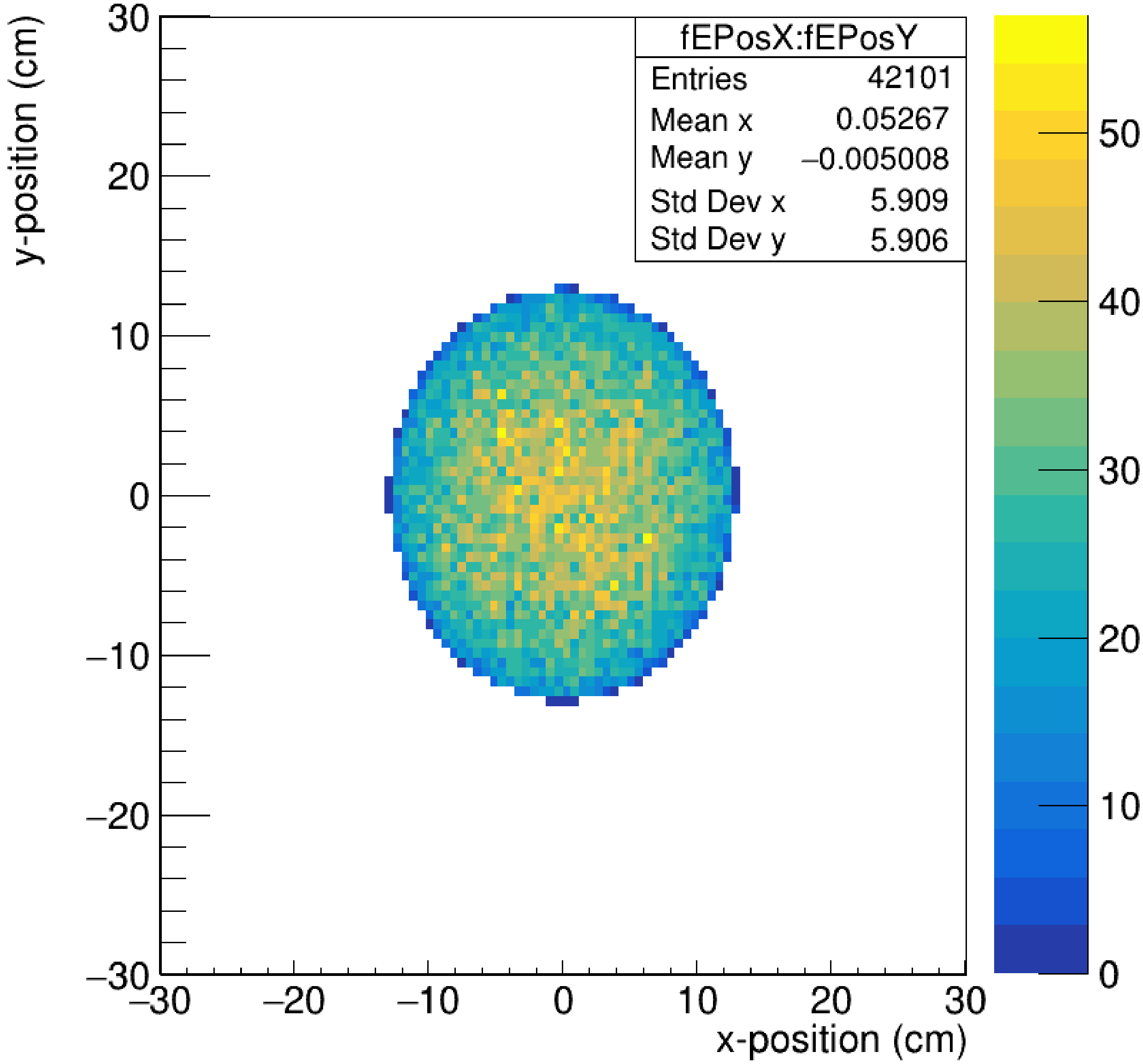
fEPosX:fEPosY
Entries 42101
Mean x 0.05267
Mean y −0.005008
Std Dev x 5.909
Std Dev y 5.906
y-position (cm)
x-position (cm)
30
20
10
0
−10
−20
−30
50
40
30
20
10
0

Figure 5.10(a)

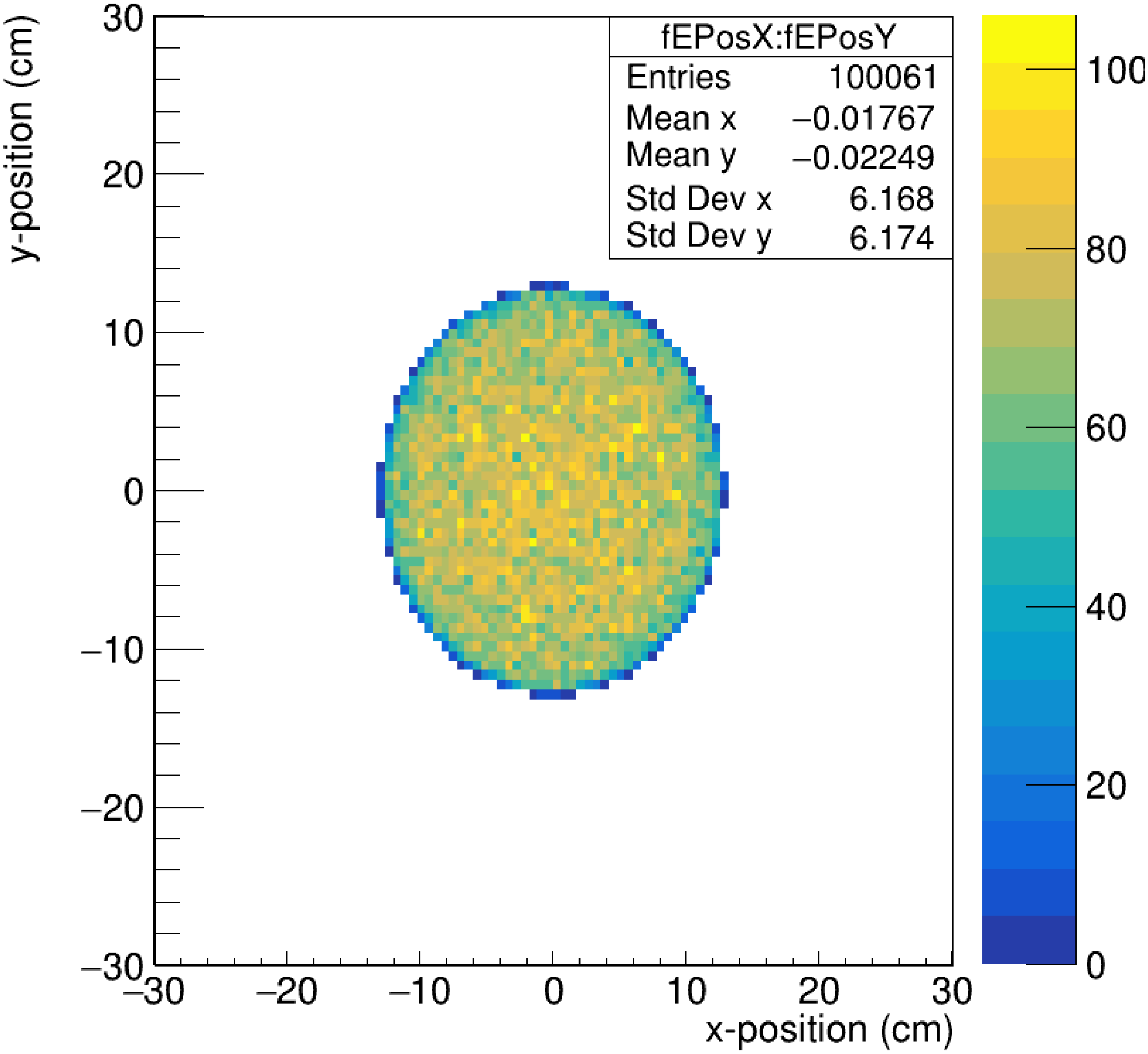

fEPosX:fEPosY
Entries 100061
Mean x −0.01767
Mean y −0.02249
Std Dev x 6.168
Std Dev y 6.174
y-position (cm)
x-position (cm)
30
20
10
0
−10
−20
−30
100
80
60
40

Figure 5.10(b)

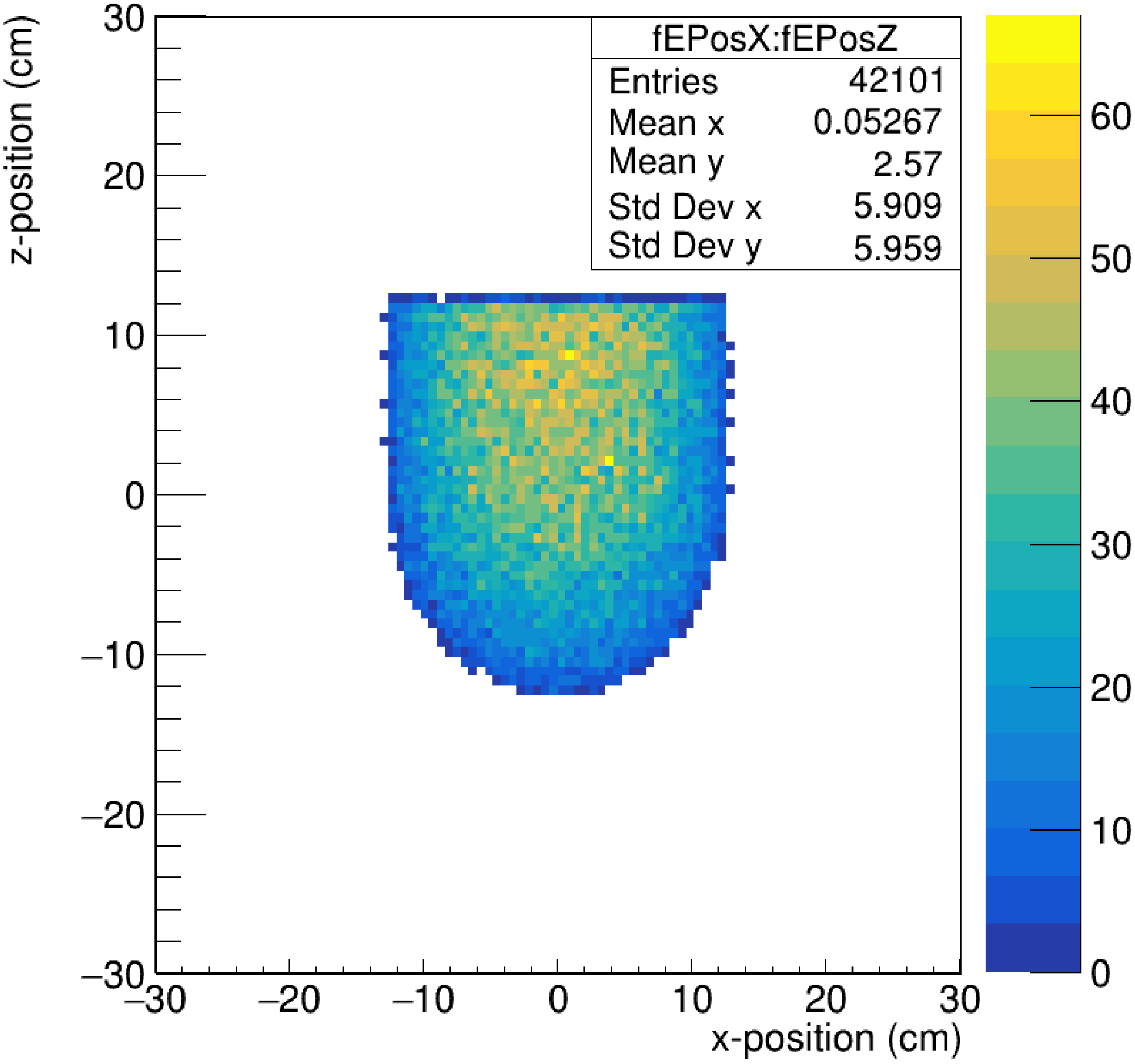
fEPosX:fEPosZ
Entries 42101
Mean x 0.05267
Mean y 2.57
Std Dev x 5.909
Std Dev y 5.959
z-position (cm)
x-position (cm)
30
20
10
0
−10
−20
−30
60
50
40
30
20
10
0

Figure 5.10(c)

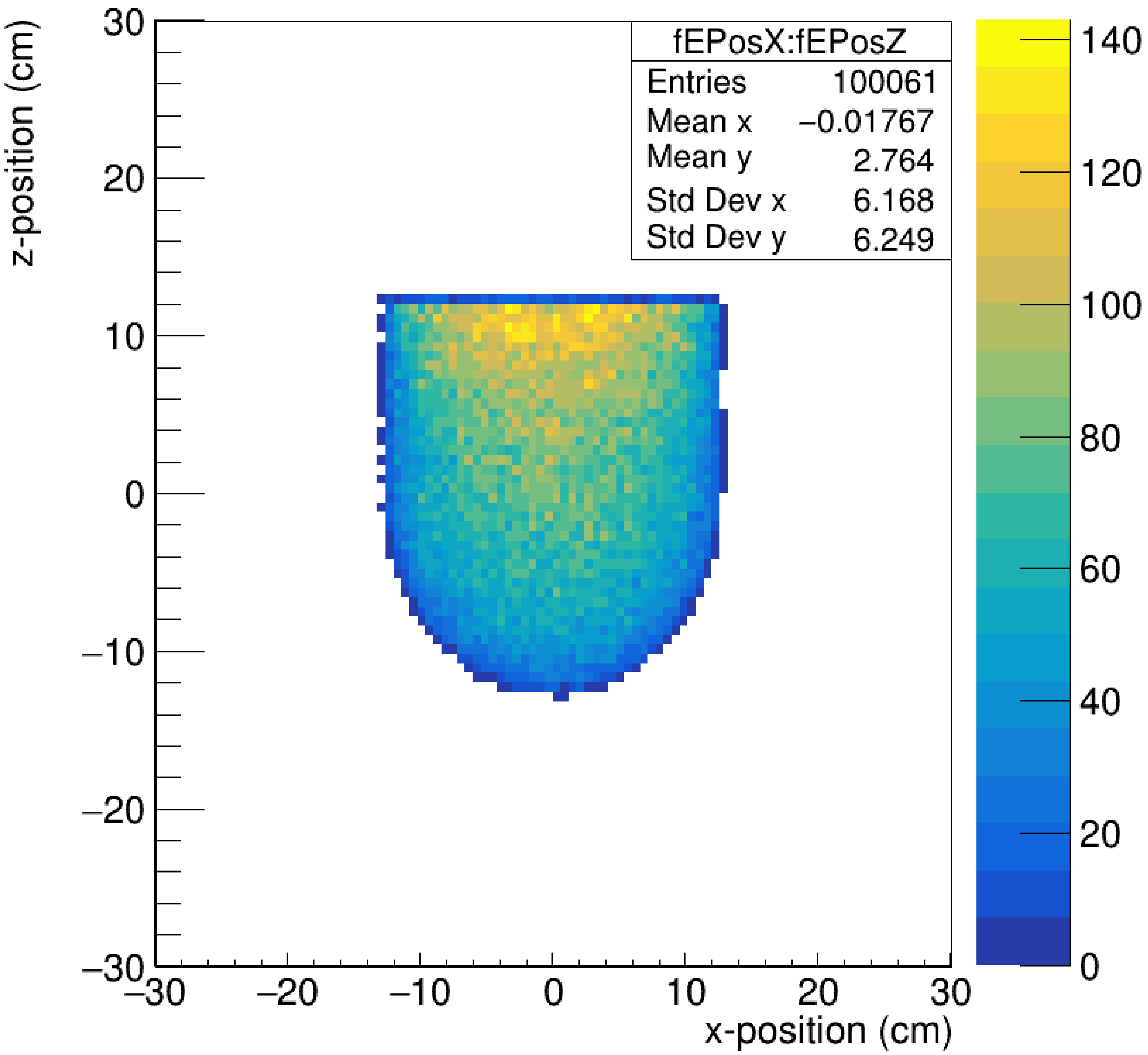

fEPosX:fEPosZ
Entries 100061
Mean x −0.01767
Mean y 2.764
Std Dev x 6.168
Std Dev y 6.249
z-position (cm)
x-position (cm)
30
20
10
0
−10
−20
−30
140
120
100
80
60
40
20
0

Figure 5.10(d)

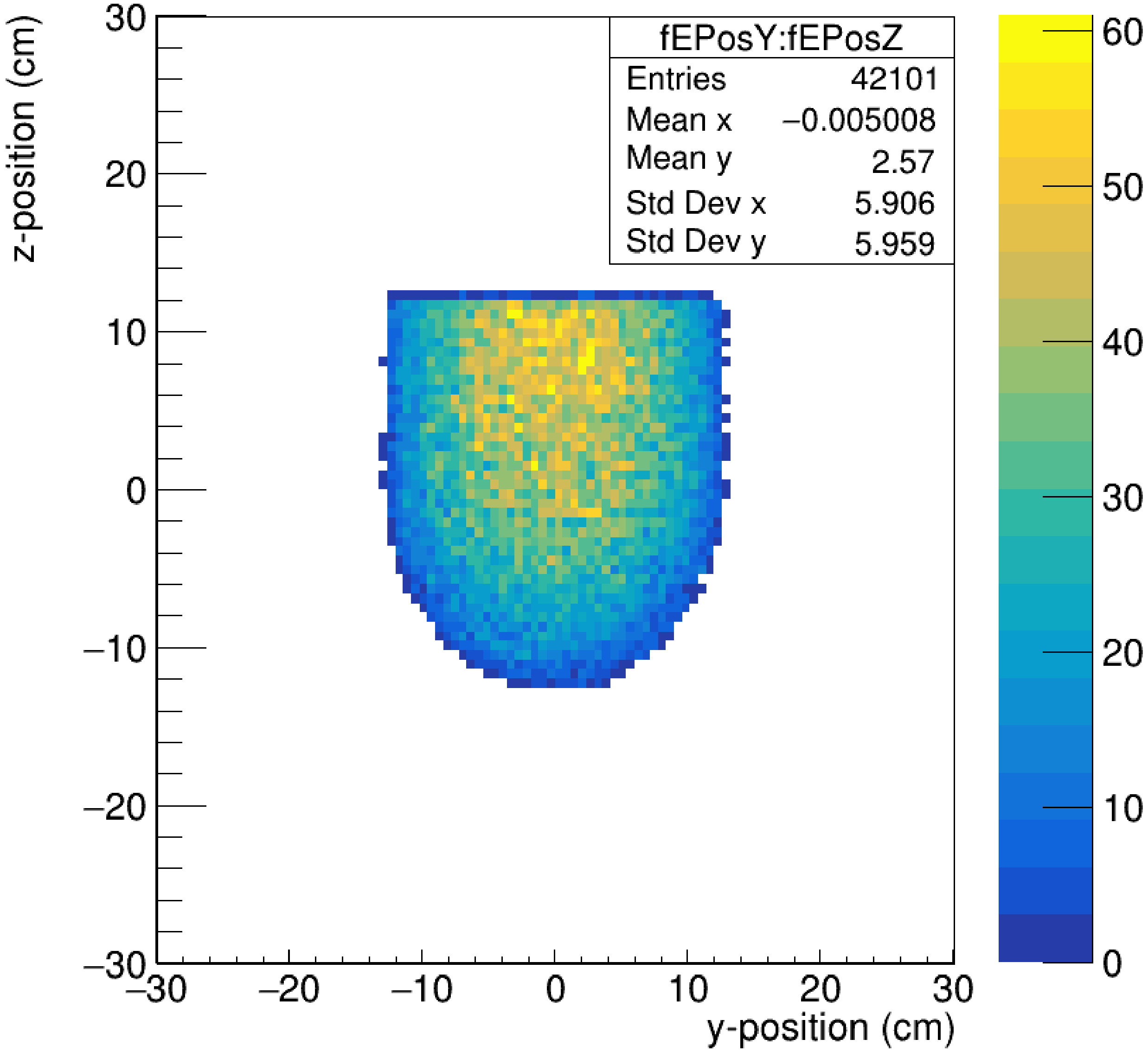
fEPosY:fEPosZ
Entries 42101
Mean x −0.005008
Mean y 2.57
Std Dev x 5.906
Std Dev y 5.959
z-position (cm)
y-position (cm)
30
20
10
0
−10
−20
−30
60
50
40
30
20
10
0

Figure 5.10(e)

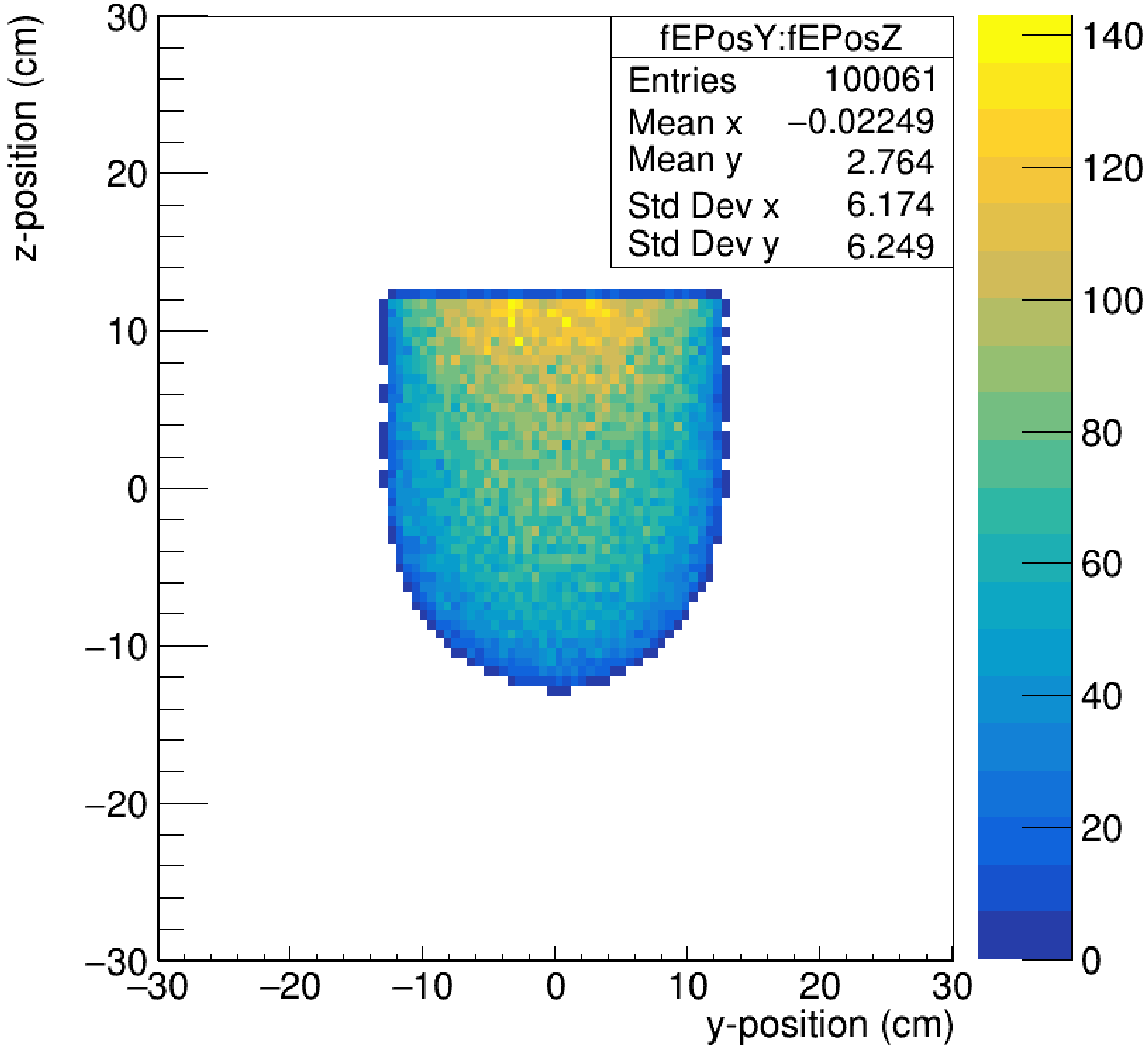

fEPosY:fEPosZ
Entries 100061
Mean x −0.02249
Mean y 2.764
Std Dev x 6.174
Std Dev y 6.249
z-position (cm)
y-position (cm)
30
20
10
0
−10
−20
−30
140
120
100
80
60
40
20
0

Figure 5.10(f)

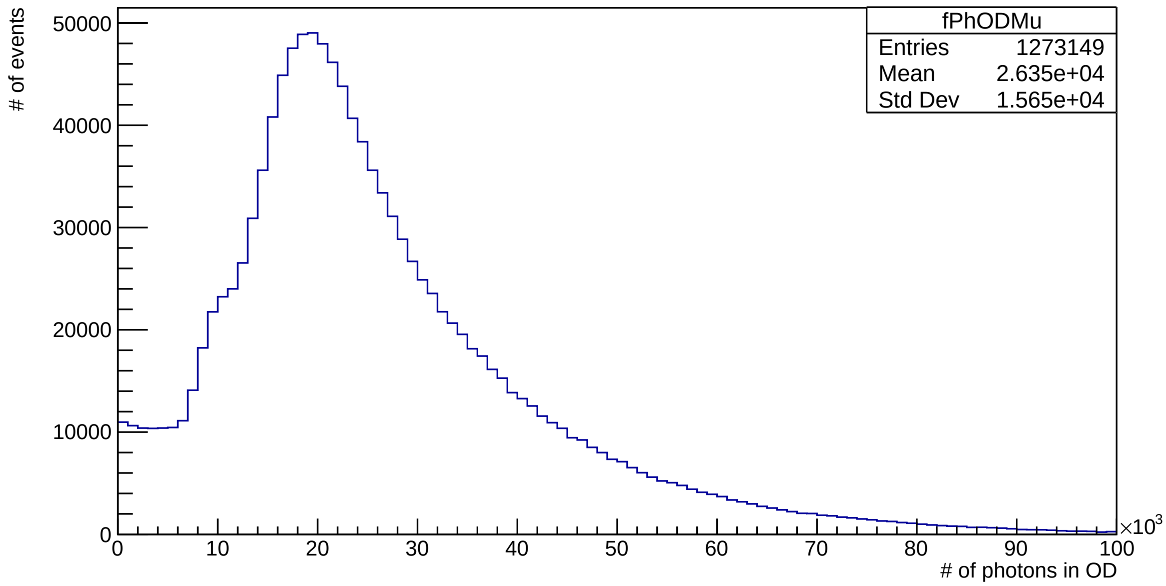

Figure 5.11(a)

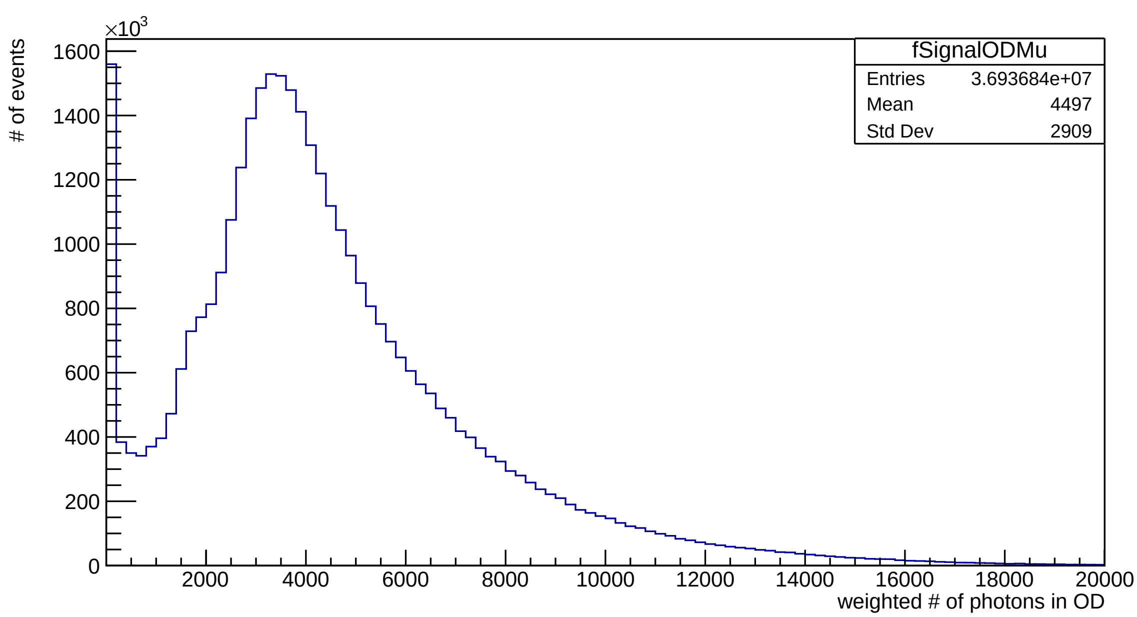

Figure 5.11(b)

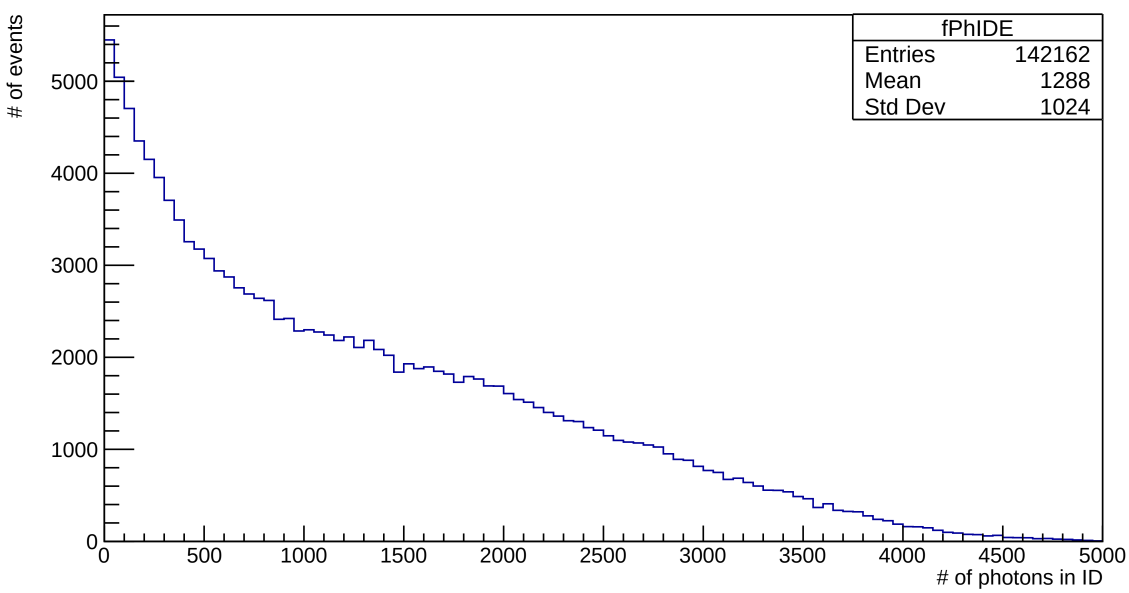

Figure 5.11(c)

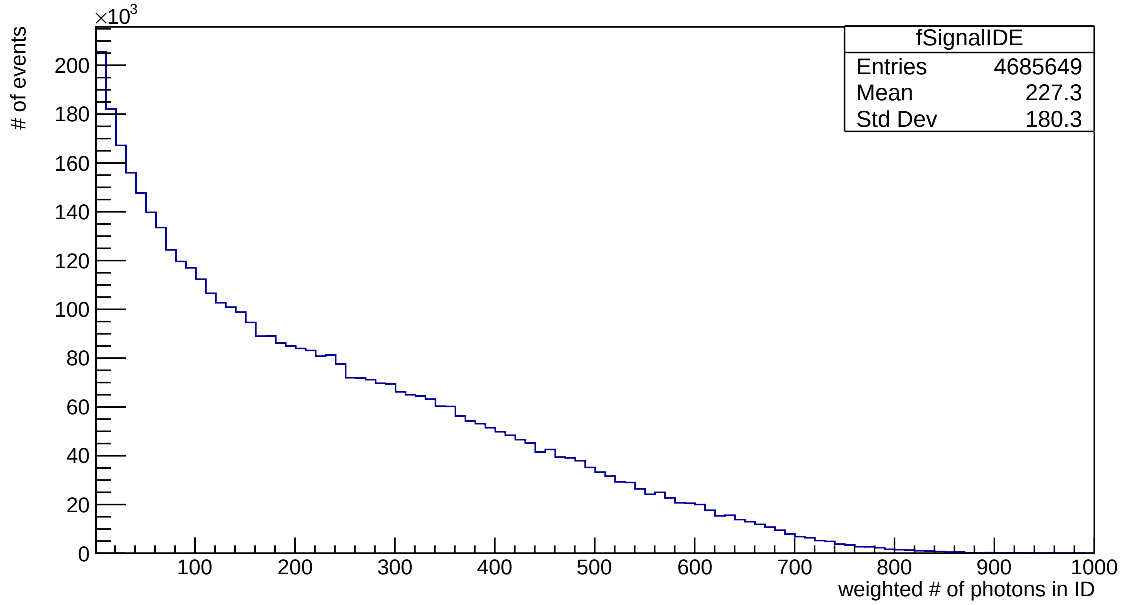

Figure 5.11(d)